2007

Temperature-dependent homogenization technique and nanoscale meshfree particle methods

Weixuan Yang
University of Iowa

TEMPERATURE-DEPENDENT HOMOGENIZATION TECHNIQUE AND NANOSCALE MESHFREE PARTICLE METHODS

by

Weixuan Yang

An Abstract

Of a thesis submitted in partial fulfillment of the
requirements for the Doctor of Philosophy degree
in Mechanical Engineering in
the Graduate College of
The University of Iowa

July 2007

Thesis Supervisor: Assistant Professor Shaoping Xiao

ABSTRACT

In this thesis, we develop a temperature-dependent homogenization technique and implement it into the meshfree particle method for nanoscale continuum simulations. As a hierarchical multiscale method, the nanoscale meshfree particle method is employed to model and simulate nanostructured materials and devices.

Recently developed multiscale methods can overcome the limitations of both length and time scales that molecular dynamics has. However, multiscale methods have difficulties in investigating temperature-dependent physical phenomena since most homogenization techniques employed in continuum models have an assumption of zero temperature. A new homogenization technique, the temperature-related Cauchy-Born (TCB) rule, is proposed with the consideration of the free energy instead of the potential energy in this thesis. This technique is verified via stress analyses of several crystalline solids. The studies of material stability demonstrate the significance of temperature effects on nanostructured material stability.

Since meshfree particle methods have advantages on simulating the problems involving extremely large deformations and moving boundaries, they become attractive options to be used in the hierarchical multiscale modeling to approximate a large number of atoms. In this thesis, a nanoscale meshfree particle method with the implementation of the developed homogenization technique, i.e. the TCB rule, is proposed. It is shown that numerical simulations in nanotechnology can be beneficial from this technique by saving a great amount of computer time. The nanoscale meshfree particle method is employed to investigate the crack propagation in a nanoplate with the development of cohesive zone model and a thermal-mechanical coupling model. In addition, the nanoscale meshfree

particle method is simplified to successfully study mechanisms of nanotube-based memory cells.

Abstract Approved: _____
Thesis Supervisor

_____
Title and Department

_____
Date

TEMPERATURE-DEPENDENT HOMOGENIZATION TECHNIQUE AND NANOSCALE MESHFREE PARTICLE METHODS

by

Weixuan Yang

A thesis submitted in partial fulfillment of the
requirements for the Doctor of Philosophy degree
in Mechanical Engineering in
the Graduate College of
The University of Iowa

July 2007

Thesis Supervisor: Assistant Professor Shaoping Xiao

Graduate College
The University of Iowa
Iowa City, Iowa

CERTIFICATE OF APPROVAL

_____

PH.D. THESIS

_____

This is to certify that the Ph.D. thesis of

Weixuan Yang

has been approved by the Examining Committee
for the thesis requirement for the Doctor of
Philosophy degree in Mechanical Engineering
at the July 2007 graduation.

Thesis Committee: _____
Shaoping Xiao, Thesis Supervisor

_____
Jia Lu

_____
Sharif Rahman

_____
Colby Swan

_____
Weimin Han

To my family

ACKNOWLEDGEMENTS

I would like to express my deep and sincere gratitude to my advisor, Professor Shaoping Xiao. His inspirational suggestions and careful guidance have been of great value for me in these four years. I also would like to thank Professor David Andersen for the help with the electromagnetics and relevant discussions.

Many special thanks go to my wife Qingyuan Wang, who shared happiness and difficult times with me. She has been a great source of strength for me all through this work.

Finally, I am forever indebted to my parents for their understanding and encouragement. I dedicate this work to all of them.

ABSTRACT

In this thesis, we develop a temperature-dependent homogenization technique and implement it into the meshfree particle method for nanoscale continuum simulations. As a hierarchical multiscale method, the nanoscale meshfree particle method is employed to model and simulate nanostructured materials and devices.

Recently developed multiscale methods can overcome the limitations of both length and time scales that molecular dynamics has. However, multiscale methods have difficulties in investigating temperature-dependent physical phenomena since most homogenization techniques employed in continuum models have an assumption of zero temperature. A new homogenization technique, the temperature-related Cauchy-Born (TCB) rule, is proposed with the consideration of the free energy instead of the potential energy in this thesis. This technique is verified via stress analyses of several crystalline solids. The studies of material stability demonstrate the significance of temperature effects on nanostructured material stability.

Since meshfree particle methods have advantages on simulating the problems involving extremely large deformations and moving boundaries, they become attractive options to be used in the hierarchical multiscale modeling to approximate a large number of atoms. In this thesis, a nanoscale meshfree particle method with the implementation of the developed homogenization technique, i.e. the TCB rule, is proposed. It is shown that numerical simulations in nanotechnology can be beneficial from this technique by saving a great amount of computer time. The nanoscale meshfree particle method is employed to investigate the crack propagation in a nanoplate with the development of cohesive zone model and a thermal-mechanical coupling model. In addition, the nanoscale meshfree

particle method is simplified to successfully study mechanisms of nanotube-based memory cells.

TABLE OF CONTENTS

LIST OF TABLES

LIST OF FIGURES

LIST OF SYMBOLS

Ω_0	Material body in the reference configuration
Ω	Material body in the current configuration
$\mathbf{X}$	Position in the reference configuration
$\mathbf{x}$	Position in the current configuration
$\mathbf{u}$	Displacement
$\mathbf{u}^h$	Approximation of displacement by Meshfree Particle Methods
$\mathbf{F}$	Deformation gradient
$\mathbf{P}$	Nominal stress
$\boldsymbol{\sigma}$	Cauchy stress
$\mathbf{b}$	Body force per unit mass
$\bar{\mathbf{t}}$	Boundary traction
ρ_0	Mass per unit reference volume
ρ	Mass per unit current volume
J	Determinant of deformation gradient
V_0	Volume in reference configuration
A_0	Area in reference configuration
ω_I	Kernel function for particle I
W	Weight function
h	Support radius of the influence domain
D_{mx}	Dilation parameter
c_0	Wave speed

E^e	Effective Young's modulus of the material
$\mathbf{f}^{int}$	Internal force
$\mathbf{f}^{ext}$	External force
ξ	Coordinates in the parent (isoparametric) configuration
N	Finite Element shape function
$\overline{\mathbf{J}}$	Determinant of the Jacobin matrix of the isoparametric mapping
t	Time
m	Mass
$\mathbf{A}$	Lattice vector in reference configuration
$\mathbf{a}$	Lattice vector in current configuration
W_C	Continuum strain energy at 0K
w_C	Continuum strain energy density at 0K
$\mathbf{C}$	First elasticity tensor or first tangential stiffness matrix
F_H	Atomic free energy
S	Atomic entropy
T	System temperature
T_0	Desired system temperature
ω_n	Vibration frequencies of molecular system
$\mathbf{D}$	Dynamical matrix
$\overline{\mathbf{D}}$	Determinant of dynamical matrix
W_H	Free energy in continuum model
w_H	Free energy density in continuum model

l_0, r_0	Equilibrium bond length
l, r	Current bond length
φ	Interatomic potential
$\boldsymbol{\eta}$	Inner displacement
θ_0	Equilibrium bond angle
θ	Current bond angle
$\boldsymbol{\tau}$	Cohesive traction
$\boldsymbol{\Delta}$	Crack opening displacement vector
β	Scaling parameter in the bridging domain
$\boldsymbol{A}^{0}$	Acoustic tensor
c	Specific heat capacity
k	Thermal conductivity
F_{eff}	Effective interlayer friction
f	Frequency
ε_0	Permittivity of free space
$\mathbf{E}$	Electric field
Q	Charge
C	Capacitance
V	Voltage on the electrode
$\otimes$	Tensor product
Δ	Difference
∇	Gradient

CHAPTER 1

INTRODUCTION

1.1 Motivation

Significant interest has been generated recently in the field of nanoscale materials and devices, in which the grain size is usually in the range of 1-100nm. Within this length scale, the properties of matter are sufficiently different from both individual atoms/molecules and bulk materials. Such studies have been recently recognized as a new area of science, which is generally termed Nanoscience. Even more popular than Nanoscience has become the term Nanotechnology, which relates to the ability to build functional devices based in the controlled assembly of nanoscale objects, for specific technological applications [1-3]. Nanotechnology has been playing an important role in materials science, space exploration and information technology. It can also offer new techniques for biotechnology and agriculture. Nanotechnology covers a wide range of industries, and therefore the potential benefits are also widespread.

Numerical simulation has become a powerful tool and has made a significant contribution to the fields of nanoscience and nanotechnology. The efficient numerical methods will stimulate the nanotechnology development, such as the nanoscale material and device design. The popularly-used molecular dynamics is expected to be one of the candidates. Although molecular systems with billions of atoms [4, 5] can be modeled using molecular dynamics (MD) with current high-performance computing techniques, limitations of MD are always found on both length and time scales. These limitations prevent us from studying certain phenomena such as material failure. With the

development of nanotechnology, multiscale methods have been of interest as a potential alternative for MD since they are feasible for simulating large nanoscale systems.

Recently developed multiscale methods still have some limitations. One issue is that most multiscale methods conduct continuum approximation in large scales through a homogenization technique such as the Cauchy-Born (CB) rule [6, 7]. It provides the constitutive relation as a link between molecular and continuum models. However, the conventional CB rule assumes that the simulated systems are at zero temperature. Consequently, temperature effects at the nanoscale cannot be investigated via the continuum approximation. On the other hand, it has been shown that most physical phenomena of nanoscale materials and devices [8], particularly material failure and damping in devices, are temperature-dependent. Therefore, a temperature-dependent homogenization technique is needed to enhance multiscale models.

Most multiscale methods employ finite element methods in continuum models. Since meshfree particle methods are more attractive for usage in a variety of situations [9-12], including problems with moving boundaries, discontinuities, and extremely large deformations, the incorporation of them with a homogenization technique will benefit the simulation through multiscale methods.

1.2 Literature Review of Multiscale Modeling

There are two types of multiscale methods: concurrent multiscale methods and hierarchical multiscale methods.

1.2.1 Concurrent Multiscale Modeling

Concurrent multiscale methods treat different length scales simultaneously by using different numerical methods. The recently developed concurrent multiscale techniques mainly focus on the coupling methods between the continuum and molecular models. Abraham and his coworkers [13, 14] developed a methodology called MAAD (Macro-Atomistic-*Ab initio*-Dynamics), which coupled a tight-binding quantum mechanical calculation, molecular dynamics, and a finite element method. Rudd and Broughton [15, 16] proposed a coarse-grained method. They superimposed the atomistic Hamiltonian on a continuum Hamiltonian so a coarse scale domain was used to represent the fine scale domain. Wagner and Liu [17] have proposed a bridging scale method in which the molecular displacements were decomposed into a molecular scale and a continuum scale. Park and his co-workers [18] developed a multiscale method in which the molecular displacements are decomposed into fine scale (molecular) and coarse scale (continuum). Belytschko and Xiao [19, 20] developed a bridging domain coupling method by overlapping the continuum model and the molecular model via the bridging domain. Their method can efficiently eliminate the nonphysical wave reflection that usually occurs at the interface of different length scales.

1.2.2 Hierarchical Multiscale Modeling

Hierarchical multiscale methods use the continuum approximation to model a large group of molecules. The continuum approximation is based on the properties of the atomic model, such as an MD model. One can use a homogenization procedure, like the Cauchy-Born rule, in the continuum model. Consequently, the intrinsic properties of the material at the atomic level can be obtained and embedded in the continuum model. The

classical Cauchy-Born rule states that the deformation is locally homogeneous, and this model is also called the quasicontinuum model. Based on an extended version of the local quasicontinuum model [21], Smith and his coworkers reported that the simulations of silicon nanoindentation were capable of handling complex crystal structures. Diestler et al. [22, 23] developed an alternative "static" finite-element coarse-graining description which is an extension to nonzero temperatures of the quasicontinuum procedure. The major drawbacks of hierarchical multiscale methods relate to the difficulties in modeling defects in molecular lattices, dislocations, crack initiation and growth, as well as limitations arising from the homogeneous deformation model used. There are several algorithms to solve these issues. Rodney and Phillips [24] built quasicontinuum simulations of dislocations lying in intersecting slip planes, and calculated the threshold stress required to break the dislocation junction. Mortensen and his coworkers [25] used a mixed local/nonlocal quasicontinuum with some modifications to study a cross-slip of screw dislocations and job mobility in copper. With the wide usage of the Cauchy-Born rule, Arroyo and Belytschko [26, 27] found that the classical Cauchy-Born rule has some difficulties for many important situations, such as in single-layer curved crystalline sheets. They developed a methodology called the exponential Cauchy-Born rule to solve this issue. Shenoy et al. [28] developed a finite-temperature quasicontinuum method. Chen et al. [29] developed a discontinuous Galerkin (DG) method, within the framework of the heterogeneous multiscale method (HMM), to solve hyperbolic and parabolic multiscale problems.

1.3 Objectives

The ultimate objective of this thesis is to develop an efficient hierarchical multiscale method for modeling nanostructured materials and simulating temperature-dependent physical phenomena at the nanoscale.

The purposes of the present work are the following: (1) to develop a new homogenization technique, the temperature-related Cauchy-Born (TCB) rule, for multiscale methods; (2) to implement the TCB rule into meshfree particle method to investigate the temperature effects on nanostructured materials; (3) to analyze temperature-dependent material stability of nanostructured materials; (4) to develop a thermal-mechanical coupling model for nanoscale continuum simulations; (5) to study electromechanical behavior of nanotube-based devices.

1.4 Outline of the Thesis

The thesis is organized as follows.

- **Chapter 2: Meshfree Particle Methods**

Meshfree particle methods are briefly introduced in this chapter. The weak forms for particle methods are derived from the governing equations. Based on the kernel approximation, the discrete equations are then given. Two different domain integration schemes and explicit time integration scheme are introduced here. In addition, the stability of meshfree particle methods using different kernel functions and integration schemes are briefly discussed.

- **Chapter 3: Temperature-dependent Homogenization Technique**

In this chapter, a new temperature-dependent homogenization technique for multiscale modeling, the temperature-related Cauchy-Born (TCB) rule, is developed.

Stress analyses of several crystalline solids verify the continuum approximation with the TCB rule by comparing the calculated Cauchy stresses with the outcomes of molecular dynamics simulations.

- **Chapter 4: Nanoscale Meshfree Particle Methods**

A nanoscale meshfree particle method with the implementation of the temperature-related Cauchy-Born rule is proposed in this chapter. Several numerical examples show that numerical simulations in nanotechnology can be beneficial from the advantages of the meshfree particle methods. This progress could not only save a great amount of computer time but also make it possible to treat extremely large deformation problems and the problems involving discontinuities, such as fractures, at nanoscale. Through this hierarchical multiscale method, the nanoscale crack propagation problem is investigated using visibility criterion and cohesive model. The observed crack propagation phenomena at finite temperatures match the ones in molecular dynamics simulations. It is shown that the temperature effects are significant on the crack propagation speed when the temperature is in a particular range.

- **Chapter 5: Temperature-dependent Material Stability**

The general concept of material stability and several different stability criteria of crystalline solids are introduced and compared in this chapter. A standard linearized stability analysis process is conducted for nanostructured materials using temperature-dependent homogenization technique. It can be seen that temperature effects on material stability of nanostructured materials are significant.

- **Chapter 6: Thermal-mechanical Coupling**

In this chapter, a thermo-mechanical model is developed via coupling the energy equation with the momentum equations in nanoscale continuum approximations. The temperature-related constitutive relation is represented by TCB rule and the system temperature profile is updated via solving discrete equations of thermal flow. The nanoscale crack propagation is reanalyzed using the thermal-mechanical coupling method.

- **Chapter 7: Nanotube-based Oscillator**

The mechanism of the nanotube-based oscillator is studied by the nanoscale meshfree particle method in this chapter. Since the rigid body motion dominates the oscillation of oscillators, the nanoscale meshfree particle model is simplified to calculate interlayer interaction between the outer tube and inner tube. A nanoelectromechanical systems (NEMS) design, containing nanotube-based oscillators is proposed as a memory cell. Numerical analyses demonstrate that the representation of the Boolean logic states is possible.

- **Chapter 8: Summary and Future Work**

The present research work is summarized. The future tasks are outlined.

1.5 Contributions

The contributions of the present work include:

1. Developing a new temperature-dependent homogenization technique for hierarchical multiscale modeling.
2. Developing a new hierarchical multiscale method in which the TCB rule was implemented into meshfree particle methods so that temperature effects on mechanics of nanostructured materials could be investigated via continuum approximations.

3. Investigating nanoscale crack propagation problems at various temperatures using the developed hierarchical multiscale method and a cohesive zone model.
4. Analyzing the material stability of nanostructured materials with the consideration of temperature effects.
5. Coupling the energy equation with the momentum equations in the nanoscale continuum approximation to analyze the thermo-mechanical behavior of the nanoscale crack propagation.
6. Studying the electromechanical properties of the nanotube-based memory cell to obtain the steady oscillatory mechanism and Boolean logic states.

CHAPTER 2

MESHFREE PARTICLE METHODS

2.1 Introduction

Finite element methods are often used for modeling continua in multiscale methods based on the quasicontinuum approach. However, meshfree particle methods are more attractive for usage in a variety of situations, including problems with moving boundaries, discontinuities, and extremely large deformations. In general, there are two types of meshfree particle methods: field approximation based methods, such as Element-Free Galerkin (EFG) methods [30], and kernel approximation based methods, such as Reproduced Kernel Particle Methods (RKPM) [31] and Smoothed Particle Hydrodynamics (SPH) [32]. There are two kernel functions used in the kernel based meshfree particle methods: the Lagrangian kernel, which is a function of the material coordinates, and the Eulerian kernel, which is a function of the spatial coordinates. In this thesis, we will employ the meshfree particle methods with a Lagrangian kernel.

2.2 Governing Equations

One of the physical principles governing the continuum is the conservation of momentum, and it can be written as the follows under a so-called total Lagrangian description in a reference configuration Ω_0:

$$\frac{\partial P_{ji}}{\partial X_j} + \rho_0 b_i = \rho_0 \ddot{u}_i \tag{2.1}$$

where ρ_0 is the initial density, $\mathbf{P}$ is the nominal stress (the transpose of the first Piola-Kirchhoff stress) [33], $\mathbf{X}$ are the material (Lagrangian) coordinates, $\mathbf{b}$ is the body force

per unit mass and **u** is the displacement and the superposed dots denote material time derivatives. Eq. (2.1) can be written as the spatial form of the momentum equations under the Eulerian description in the current configuration Ω:

$$\frac{\partial \sigma_{ji}}{\partial x_j} + \rho b_i = \rho \ddot{u}_i \tag{2.2}$$

where ρ is the current density, **σ** is the Cauchy stress tensor, and **x** are the spatial (Eulerian) coordinates. By conservation of mass,

$$\rho J = \rho_0 \tag{2.3}$$

where J is the Jacobian determinant of deformation gradient $\mathbf{F}$, which are defined by

$$J = \det(\mathbf{F}), \quad F_{ij} = \frac{\partial x_i}{\partial X_j} \tag{2.4}$$

It can be seen that the two above forms of momentum equations in Eq. (2.1) and Eq. (2.2) are identical and differ in form only because they are expressed in different descriptions [33, 34]. Since we use the Lagrangian description in this thesis, the Galerkin weak form of the momentum conservation equation is

$$\int_{\Omega_0} \delta u_i \rho_0 \ddot{u}_i d\Omega_0 = \int_{\Omega_0} \delta u_i \rho_0 b_i d\Omega_0 - \int_{\Omega_0} \delta F_{ij} P_{ji} d\Omega_0 + \int_{\Gamma_0} \delta u_i \bar{t}_i d\Gamma_0 \tag{2.5}$$

where δu_i is the test function, and $\bar{t}_i$ is the prescribed boundary traction. The discrete equations of motion can be derived from weak form, Eq. (2.5), for dynamic problems.

2.3 Particle Method Approximations and Kernel Functions

In particle methods, displacements can be approximated by

$$\mathbf{u}^h(\mathbf{X}, t) = \sum_I \omega_I(\mathbf{X}) \mathbf{u}_I(t) \tag{2.6}$$

where $\omega_I(\mathbf{X})$ are called Lagrangian kernel functions [35] because they are functions of material (Lagrangian) coordinates. If spatial (Eulerian) coordinates are used, the approximation of displacements can be written in terms of Eulerian kernel functions as the follows:

$$\mathbf{u}^h(\mathbf{x}(t),t) = \sum_I \omega_I(\mathbf{x}(t))\mathbf{u}_I(t) \tag{2.7}$$

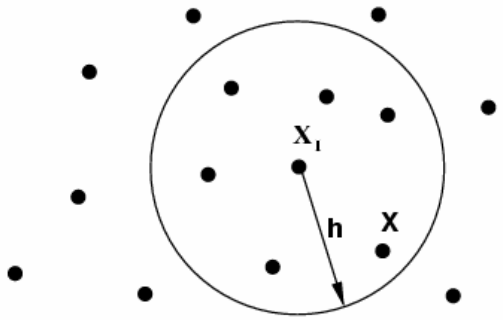

Figure 2.1: The domain of influence of particle $\mathbf{X}_I$

In this thesis, we use Lagrangian kernel functions because particle methods with Lagrangian kernel functions are more stable than the ones with Eulerian kernel functions [35]. The Lagrangian kernel functions can be obtained from the weight function,

$$\omega_I(\mathbf{X}) = \omega(\mathbf{X}-\mathbf{X}_I) = \frac{W(\mathbf{X}-\mathbf{X}_I)}{\sum_K W(\mathbf{X}-\mathbf{X}_K)} \tag{2.8}$$

which is the kernel approximation that reproduces constant functions. Here, we use a quartic spline weight function

$$W(s) = \begin{cases} 1-6s^2+8s^3-3s^4 & \text{for} \quad s \le 1 \\ 0 & \text{for} \quad s > 1 \end{cases} \tag{2.9}$$

where $s = r/h$, $r = \|\mathbf{X} - \mathbf{X}_I\|$, and h is the support radius of the influence domain as shown in Fig. 2.1. It is determined by a dilation parameter D_{mx}. We define $h = D_{mx}\Delta X$ for uniformly spaced particles in one dimension. The kernel function is of compact support, i.e., $\omega_I(\mathbf{X}) > 0$ only in the neighborhood of $\mathbf{X}$.

We can see that, from Eq. (2.8), the kernel functions, $\omega_I(\mathbf{X})$, obviously reproduce the constant functions, i.e. $\sum_I \omega_I(\mathbf{X}) = 1$, but not the linear functions. In other words, one can find that $\sum_I \frac{\partial \omega_I(\mathbf{X})}{\partial X_i} X_{jI} \neq \delta_{ij}$. Krongauz and Belytschko [36] developed a correction that enables the derivatives of constant or linear functions to be reproduced exactly. The corrected derivatives of displacements are denoted by $L_{ji}(\mathbf{X},t)$ and are approximated by:

$$L_{ji}(\mathbf{X},t) = \sum_I G_{iI}(\mathbf{X}) u_{jI}(t) \tag{2.10}$$

where $G_{iI}(\mathbf{X})$ are the corrected derivatives of Lagrangian kernel functions. Note here that $L_{ji}(\mathbf{X},t)$ is different from $\frac{\partial u_j^h(\mathbf{X},t)}{\partial X_i}$ with u_j^h defined by Eq. (2.6). The corrected derivatives are defined as linear combinations of the exact derivatives of kernel functions, so linear functions (coordinates for instance) can be reproduced by the particle method approximation:

$$\sum_I G_{iI}(\mathbf{X}) X_{jI} = \sum_I a_{ik} \frac{\partial \omega_I(\mathbf{X})}{\partial X_k} X_{jI} = \delta_{ij} \tag{2.11}$$

The above can be written in a matrix form:

$$\mathbf{A}\mathbf{a}^T = \mathbf{I} \tag{2.12}$$

where $\mathbf{I}$ is the identity matrix and for a three-dimensional approximation,

$$\mathbf{A} = \begin{bmatrix} \omega_{I,X} X_I & \omega_{I,Y} X_I & \omega_{I,Z} X_I \\ \omega_{I,X} Y_I & \omega_{I,Y} Y_I & \omega_{I,Z} Y_I \\ \omega_{I,X} Z_I & \omega_{I,Y} Z_I & \omega_{I,Z} Z_I \end{bmatrix} \tag{2.13}$$

$$\mathbf{a} = \begin{bmatrix} a_{XX} & a_{XY} & a_{XZ} \\ a_{YX} & a_{YY} & a_{YZ} \\ a_{ZX} & a_{ZY} & a_{ZZ} \end{bmatrix} \tag{2.14}$$

By solving Eq. (2.12) for the coefficient matrix $\mathbf{a}$, one can obtain the corrected derivatives of kernel functions, $G_{iI}(\mathbf{X})$. Therefore, the approximation for the derivatives of the displacement in Eq. (2.10) can be written as follows:

$$L_{ji}(\mathbf{X},t) = \sum_I \left[\sum_k a_{ik}(\mathbf{X}) \omega_{I,k}(\mathbf{X}) \right] u_{jI}(t) \tag{2.15}$$

Therefore, the gradient of deformation is expressed as:

$$F_{ij} = \frac{\partial u_i}{\partial X_j} + 1 = L_{ij} + 1 \tag{2.16}$$

2.4 Discrete Equations

Substituting the approximation of displacements of Eq. (2.6) and a similar expansion for $\delta\mathbf{u}(\mathbf{X})$ into the weak form of Eq. (2.5), the following discrete equations of motion are obtained:

$$m_I \ddot{u}_{iI} = f_{iI}^{ext} - f_{iI}^{int}, \; m_I = \rho_0 V_I^0 \tag{2.17}$$

where V_I^0 is the volume associated with the particle I, f_{iI}^{ext} and f_{iI}^{int} are the external and internal nodal forces respectively, given by

$$f_{iI}^{ext} = \int_{\Omega_0} \rho_0 \omega_I b_i d\Omega_0 + \int_{\Gamma_0^t} N_I \bar{t}_i d\Gamma_0 \tag{2.18}$$

$$f_{iI}^{int} = \int_{\Omega_0} \frac{\partial \omega_I(\mathbf{X})}{\partial X_j} P_{ji} d\Omega_0 \tag{2.19}$$

Stationary principles can be applied for conservative, static problems. The equilibrium solutions can be found by searching a set of displacements from which the minimum potential can be obtained, i.e.

$$\begin{aligned} 0 = \delta W(\mathbf{u}) &= \delta W^{int}(\mathbf{u}) - \delta W^{ext}(\mathbf{u}) \\ &= \int_{\Omega_0} \delta F_{ij} P_{ji} d\Omega_0 - \int_{\Omega_0} \delta u_i \rho_0 b_i d\Omega_0 - \int_{\Gamma_0} \delta u_i \bar{t}_i d\Gamma_0 \end{aligned} \tag{2.20}$$

Note here that Eq. (2.20) is identical to Eq. (2.5) if the accelerations are set zero in Eq. (2.5) for static problems. We can obtain the residual as:

$$0 = r_{iI} = \frac{\partial W}{\partial u_{iI}} = \frac{\partial W^{int}}{\partial u_{iI}} - \frac{\partial W^{ext}}{\partial u_{iI}} = f_{iI}^{int} - f_{iI}^{ext} \tag{2.21}$$

where internal and external nodal forces are defined as Eq. (2.18) and Eq. (2.19).

The increments of the internal and external forces can be related to the increments of nodal displacements by stiffness matrices via the Newton method:

$$\Delta \mathbf{f}^{int} = \mathbf{K}^{int} \Delta \mathbf{u} \quad \text{or} \quad \Delta \mathbf{f}_I^{int} = \sum_J \mathbf{K}_{IJ}^{int} \Delta \mathbf{u}_J \tag{2.22}$$

$$\Delta \mathbf{f}^{ext} = \mathbf{K}^{ext} \Delta \mathbf{u} \quad \text{or} \quad \Delta \mathbf{f}_I^{ext} = \sum_J \mathbf{K}_{IJ}^{ext} \Delta \mathbf{u}_J \tag{2.23}$$

where $\mathbf{K}^{int}$ and $\mathbf{K}^{ext}$ are tangent stiffness matrices given by

$$\mathbf{K}_{IJ}^{int} = \frac{\partial \mathbf{f}_I^{int}}{\partial \mathbf{u}_J} = \frac{\partial^2 W^{int}}{\partial \mathbf{u}_I \partial \mathbf{u}_J}, \ \mathbf{K}_{IJ}^{ext} = \frac{\partial \mathbf{f}_I^{ext}}{\partial \mathbf{u}_J} = \frac{\partial^2 W^{ext}}{\partial \mathbf{u}_I \partial \mathbf{u}_J} \tag{2.24}$$

Therefore, Newton equations can be obtained by linearization of Eq. (2.21) as:

$$\left(\mathbf{K}^{int} - \mathbf{K}^{ext}\right) \Delta \mathbf{u} = -\mathbf{r} \tag{2.25}$$

2.5 Numerical Domain Integration Schemes

2.5.1 Nodal Integration

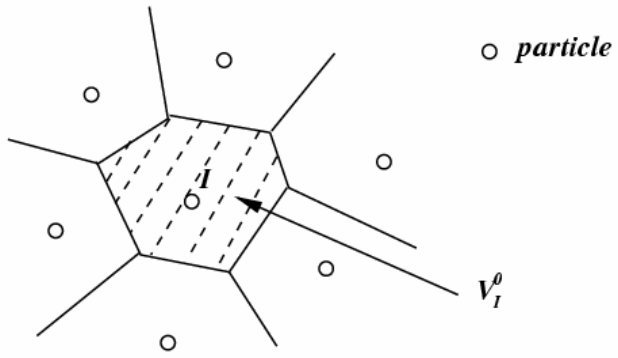

Figure 2.2: Volume associated with particle I for nodal integration scheme

To obtain the discrete momentum equations from the weak form, the integrals of the right hand sides of Eq. (2.18) and Eq. (2.19) need to be evaluated by numerical quadrature. In EFG method, background elements or voxels are used [30]. However, the integration by using full quadrature points is computationally intensive. Beissel and Belytscho [37] have proposed the nodal integration scheme for the EFG method, where any integral is evaluated by summing the function at the nodes, i.e.

$$\int_{\Omega_0} G(\mathbf{X})\, d\Omega_0 = \sum_I G(\mathbf{X}_I) V_I^0 \tag{2.26}$$

where $V_I^0 = m_0 / \rho_0$ is the volume associated with node I. Fig. 2.2 shows that the volume can be calculated through the triangulation and Voronoi diagram. The internal nodal force, Eq. (2.19), are then computed by

$$f_{iI}^{int} = \sum_{J \in N} V_J^0 \frac{\partial \omega_I(\mathbf{X}_J)}{\partial X_j} P_{ji}(\mathbf{X}_J) \tag{2.27}$$

This approach was found to be unstable by Beissel and Belytscho [37]. It will result in one of the instabilities due to rank deficiency for some problems [20, 35].

2.5.2 Stress Point Integration

One approach to stabilizing nodal integration is to use additional quadrature points called stress points or slave points/particles [38]. In this approach, slave particles are added to the original set of particles (master particles). The nomenclature "slave" nodes originates in finite element methods, where slave nodes are nodes whose motion is completely determined by the motion of master nodes through kinematics relations. In other words, the kinematic variables of slave particles, such as displacements and velocities, are evaluated from the neighboring master particles by the approximation, Eq. (2.6).

The most stable situation is the hexagonal arrangement of master particles in which the stress points are placed in the center of "virtual" triangles. If master particles are arranged irregularly for an object with arbitrary geometry, triangulation is usually used to construct a triangular (or tetrahedral in 3D) mesh as shown in Fig. 2.3(a). The stress points are then placed at the center of triangles (or tetrahedrons in 3D). Next, the Voronoi cells are constructed for both master particles and stress points, as shown in Fig. 2.3(b). The volumes of these cells are used as V_J^{0M} and V_J^{0S} for the stress point integration. However, the algorithms for triangulation and Voronoi diagram are complicated, especially for three-dimensional problems, and are not applicable, consequently, for multiple dimensional problems with an arbitrary geometry.

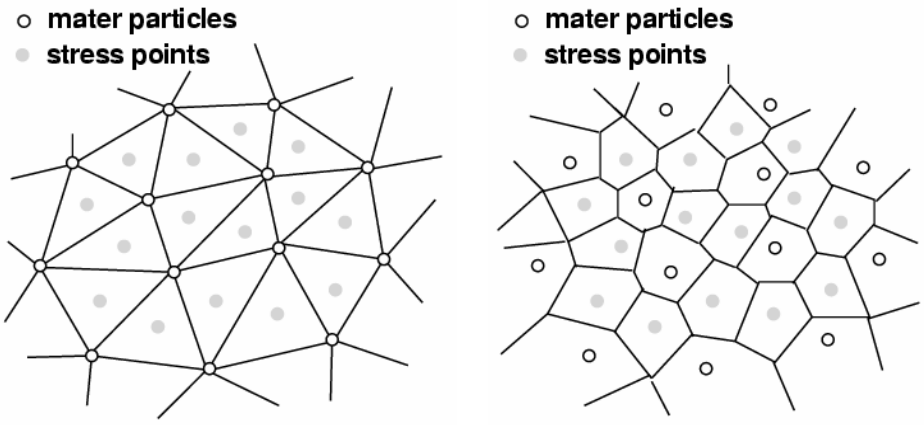

(a) Triangulation (b) Voronoi diagram

Figure 2.3: Stress point placement and volume calculation

The slave particles are used only for the integration of the Galerkin weak form; the discrete momentum equations are not enforced at the slave particles, since the displacements of the slave particles are not arbitrary. The displacements and velocities at the slave particles (stress points), according to Eq. (2.6), are

$$u_I^S = \sum_J \omega_J \left(\mathbf{X}_I^S\right) u_J^M \qquad v_I^S = \sum_J \omega_J \left(\mathbf{X}_I^S\right) v_J^M \tag{2.28}$$

where $\mathbf{X}_I^S$ is the material coordinate of a slave particle. The internal nodal forces are given by

$$f_{iI}^{int} = \sum_{J \in N_M} V_J^{0M} \frac{\partial \omega_I(\mathbf{X}_J^M)}{\partial X_j} P_{ji}(\mathbf{X}_J^M) + \sum_{J \in N_S} V_J^{0S} \frac{\partial \omega_I(\mathbf{X}_J^S)}{\partial X_j} P_{ji}(\mathbf{X}_J^S) \tag{2.29}$$

where N_M, N_S are the sets of master and slave particles, respectively, which contribute to the master particle at $\mathbf{X}_I^M$. The volumes V_J^{0M} and V_J^{0S} are the volumes of the Voronoi cells associated with the master and slave particle, respectively. It follows that

$$\sum_{J}^{N_M} V_J^{0M} + \sum_{J}^{N_S} V_J^{0S} = V_J^0 \tag{2.30}$$

In the above, V_0 is the initial total volume and N_M, N_S are the number of master particles and stress points in the model, respectively. Note that the volume for the master particle I, V_I^{0M}, differs from the volume associated with the mass, V_I^0, as in Eq. (2.17). The second term on the RHS of Eq. (2.29) is the contribution of the slave particle stresses to the master particle forces. The discrete equations of motion, Eq. (2.17), are solved only at the master particles.

2.5.3 Insertion of Stress Points

We introduce a simple technique of finite element mapping to insert stress points and to calculate volumes associated with master particles and stress points.

With current powerful finite element mesh generation software it is easy to construct triangular or tetrahedral meshes in the reference configuration for any given problem. The nodes can be taken as master particles in meshfree particle methods. In finite element methods, the reference configuration can be mapped from the parent configuration [33] via $\mathbf{X} = \mathbf{X}(\boldsymbol{\xi})$ where $\boldsymbol{\xi}$ represents coordinates in the parent (isoparametric) configuration. If stress point I is at the center of an equilateral triangle ABC in the parent configuration as shown in Fig. 2.4, the coordinate of this stress point in the reference configuration can be obtained via the finite element approximation, which is

$$\mathbf{X}^S(\boldsymbol{\xi}_I) = \sum_J N_J(\boldsymbol{\xi}_I)\mathbf{X}_J^M, \quad J = A, B, C \tag{2.31}$$

where $N(\xi)$ are finite element interpolation functions evaluated in the parent configuration. In other words, stress points are also inserted at the centers of triangular meshes in the reference configuration.

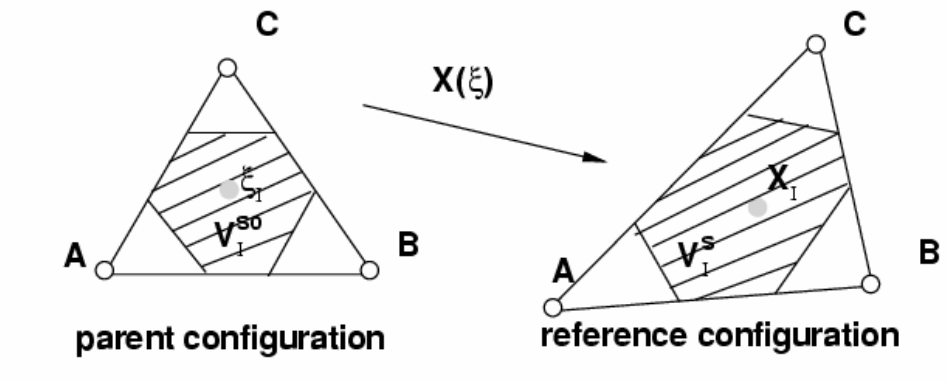

Figure 2.4: The finite element mapping technique

In the parent configuration, it is easy to calculate volume V_I^{S0} of the Voronoi cell, which is associated with stress point I. Through the isoparametric mapping technique, the volume associated with this stress point in the reference configuration is calculated by:

$$V_I^S = \bar{J} V_I^{S0} \tag{2.32}$$

where $\bar{J}$ is the determinant of the Jacobin matrix of the isoparametric mapping, and

$$\mathbf{J}(\xi_I) = \left.\frac{\partial \mathbf{X}(\xi)}{\partial \xi}\right|_{\xi_I} = \left.\left(\sum_J \frac{\partial N_J(\xi)}{\partial \xi}\mathbf{X}_J^M\right)\right|_{\xi_I} \tag{2.33}$$

A similar procedure can be performed to calculate volumes associated with master particles in the reference configuration.

2.6 Explicit Time Integration

We have seen that the momentum equation can be discretized as follows for a Lagrangian mesh

$$\mathbf{M}\ddot{\mathbf{u}} = \mathbf{f}^{ext} - \mathbf{f}^{int} = \mathbf{f} \tag{2.34}$$

The above equations are ordinary differential equations in time.

To solve Eq. (2.34), we employ explicit time integration. The most widely used explicit method is the central difference method with a diagonal or lumped mass matrix.

We start at time $t = 0$ using the time step of Δt, so that at time step n, $t = n\Delta t$. The value of a function at $n\Delta t$ is denoted by a superscript n, i.e., $\mathbf{u}^n \equiv \mathbf{u}(n\Delta t)$. In the central difference method, the velocities are approximated by

$$\dot{\mathbf{u}}^n = \mathbf{v}^{n+1/2} = \frac{\mathbf{u}^{n+1/2} - \mathbf{u}^{n-1/2}}{\Delta t} = \frac{\mathbf{u}(t + \Delta t/2) - \mathbf{u}(t - \Delta t/2)}{\Delta t} \tag{2.35}$$

where the second equality is included to clarify the notation. Half-time-step values are used for computing the velocities. The accelerations and velocities are given by

$$\ddot{\mathbf{u}}^n = \mathbf{a}^n = \frac{\mathbf{v}^{n+1/2} - \mathbf{v}^{n-1/2}}{\Delta t} \quad \text{or} \quad \mathbf{v}^{n+1/2} = \Delta t \mathbf{M}^{-1}\mathbf{f}^n + \mathbf{v}^{n-1/2} \tag{2.36}$$

where the equation on the right is obtained by combing the equation on the left with Eq. (2.34). The value of the derivative at the center of a time interval is obtained from the difference of the function values at the ends of the interval, hence the name central difference formulas.

Updating for the displacement by Eq. (2.36) does not require any solution of algebraic equations. Thus, in a sense, explicit integration is simpler than static linear stress analysis. The first time step is somewhat different form the others because only a

half-step is taken. This enables the integration to correctly account for the initial conditions on the stresses and velocities.

Most of the computation time is in computing the nodal forces, particular the internal nodal forces. The nodal forces are computed particle by particle. The computation of the internal nodal forces involves the application of the equations that are left in strong form, the strain equation and the constitutive equation. This is followed by the evaluation of the internal nodal forces from the stress by a relationship emanating from the weak form of the momentum equation.

The disadvantage of explicit integration is that the time step must be below a critical value or the solution "blows up" due to a numerical instability. The critical time step is given by

$$\Delta t_c = \frac{l_0}{c_0} \tag{2.37}$$

where l_0 is the initial distance between two particles and c_0 is the wave speed given by $c_0^2 = E^e / \rho_0$, and E^e is the effective Young's modulus of the material.

2.7 Stability of Meshfree Particle Methods

There are two sources of instability exist in meshfree particle methods: (1) rank deficiency of the discrete equations, and (2) distortion of the material instability. The latter one leads to the so-called tensile instability. Belytschko and Xiao gave a linearized stability analysis of the discrete equations for the meshfree particle methods [35]; this is often called a von Neumann stability analysis. In their studies, an infinite slab under a uniform state of stress was considered. The solution, i.e. the displacement, was perturbed by harmonics of various wavelengths as

$$\tilde{\mathbf{u}} = \mathbf{g}e^{i\omega t + i\kappa \mathbf{n}^0 \cdot \mathbf{x}} \tag{2.38}$$

where $\tilde{\mathbf{u}}$ is the plane wave perturbation, $\mathbf{g}$ is the polarization of the wave, ω is the frequency, κ is the wave number and $\mathbf{n}^0$ is the normal direction of the wave front [90]. The response is considered stable if the perturbation decays or remains constant in amplitude or unstable if it grows when time goes infinite.

When using the nodal integration scheme, instability occurs in meshfree particle methods due to rank deficiency of the discretization of the divergence. This instability makes the equilibrium equations singular regardless of the value of the stress. Such instability occurs when the nodal integration scheme is employed. Stress points are inserted to eliminate this instability. However, tensile instability occurs in meshfree particle methods as long as Eulerian kernels are employed even when the stress point integration scheme is utilized. Xiao and Belytschko [39] performed material stability analysis of meshfree particle methods. They pointed out that Eulerian kernels severely distorted the material instability while Lagrangian kernels can exactly reproduce material instability. Rabczuk et al. [40] concluded that a meshfree particle method with Lagrangian kernels and stress point integration is a stable numerical method.

2.8 Summary and Conclusions

Meshfree particle methods have been briefly introduced. Based on the governing equations, the weak forms for particle methods are derived and two different domain integration schemes and explicit time integration scheme are highlighted. In addition, the brief discussion about the stability of meshfree particle methods concluded that a meshfree particle method with Lagrangian kernels and stress point integration is a stable numerical method.

CHAPTER 3

TEMPERATURE-DEPENDENT HOMOGENIZATION TECHNIQUE

3.1 Cauchy-Born (CB) Rule

Generally, in a nanoscale continuum model, the potential energy depends on the elongations and angle changes of the atomic bonds underlying the discretized continuum domain via the conventional CB rule [41, 42]. The CB rule states that the deformation is locally homogeneous. Therefore, the atomic-level lattice follows the deformation given by the macroscopically imposed deformation gradient. For example, an undeformed lattice vector **A** in the reference configuration can be mapped into a deformed lattice vector **a** in the current configuration via

$$\mathbf{a} = \mathbf{F}\mathbf{A}\ ,\ \mathbf{F} = \frac{\partial \mathbf{x}}{\partial \mathbf{X}} \tag{3.1}$$

where **F** is the gradient of deformation, **x** are Eulerian coordinates and **X** are Lagrangian coordinates. Consequently, the total potential energy, also called the strain energy of the continuum model, in the reference configuration Ω_0 is defined by

$$W_C = \int_{\Omega_0} w_C\left(\mathbf{F}\right) d\Omega_0 \tag{3.2}$$

where w_C is the strain energy per unit volume, i.e. strain energy density. Based on nonlinear continuum mechanics [33], the nominal stress, **P**, is obtained from the first derivative of the strain energy density to the transpose of the gradient of deformation

$$\mathbf{P} = \frac{\partial w_C\left(\mathbf{F}\right)}{\partial \mathbf{F}^{\mathrm{T}}} \tag{3.3}$$

The above equation usually serves as a constitutive relation implemented into continuum models in either hierarchical or concurrent multiscale modeling of crystalline

solids. With respect to the deformation gradients, the first elasticity tensor or first tangential stiffness matrix [33] can be obtained from the second derivatives of the strain energy density as

$$\mathbf{C} = \frac{\partial^2 w_C(\mathbf{F})}{\partial \mathbf{F}^{\mathrm{T}} \partial \mathbf{F}^{\mathrm{T}}} \tag{3.4}$$

If long distance interatomic interactions, such as nonbonded interaction, are considered, the van der Waals energy must be included in the molecular mechanics potential. Further research is needed to derive the continuum strain energy from the atomic-level potential and to modify the CB rule. Since the effects of long distance interatomic interactions on nanoscale mechanical behaviors of crystalline solids are not as significant as those of short distance interatomic interactions, we only consider short distance interatomic interactions in this thesis.

The conventional CB rule has some difficulties for many important situations, such as in single-layer curved crystalline sheets. Arroyo and Belytschko [26, 27] developed an extension of the CB rule – the exponential CB rule. The objective of this extension is to account for the fact that the deformation gradient maps the tangent space of the undeformed surface to the tangent space of the deformed surface.

3.2 Temperature-related Cauchy-Born (TCB) Rule

It has been shown that physical phenomena at the nanoscale, especially nanostructured material failure, are temperature-related. Therefore, it is important to consider temperature effects in the continuum model when performing multiscale modeling and simulation. Temperature effects can be introduced by employing potentials that incorporate the entropy due to lattice vibration, for example, in a local Einstein

description [28, 43]. This is conceptually similar to the coarse graining of vibrations in first-principles thermodynamics [44]. In the proposed TCB rule, we consider the Helmholtz free energy, i.e. the effective energy in [22, 28, 45, 46], rather than the potential energy at the nanoscale. Helmholtz free energy is the amount of thermodynamic energy which can be converted into work at constant temperature and volume [47]. It can be written as

$$F_H = W_C(\mathbf{F}) - TS \tag{3.5}$$

where F_H is the atomic-level free energy of a crystalline solid, $W_C(\mathbf{F})$ is the potential energy of the atoms in their equilibrium positions, T is the system temperature and S is the system entropy.

To obtain reasonable accuracy for the Helmholtz free energy calculation in the nanoscale continuum model, the motion of an atom in a solid is assumed to be harmonic [48]. The entropy of the system of N atoms can be expressed as

$$S = -\kappa_B \sum_{n=1}^{3N} \ln\left[2\sinh\left(\frac{\hbar\omega_n}{2\kappa_B T}\right)\right] \tag{3.6}$$

where $\kappa_B = 1.38\times10^{-23}\,\mathrm{J/K}$ is the Boltzmann constant , $\hbar = h/2\pi$, $h = 6.63\times10^{-34}\,\mathrm{J\cdot s}$ is Planck's constant, ω_n are the vibration frequencies of the system and are determined from the eigenvalues of the dynamical matrix, $\mathbf{D}$, which is calculated as

$$D_{I\alpha J\beta} = \frac{1}{\sqrt{m_I m_J}}\left(\frac{\partial^2 W_C}{\partial x_{I\alpha}\partial x_{J\beta}}\right) \tag{3.7}$$

where $x_{I\alpha}$ is the vibrational coordinate in direction α for atom I, and m_I is the mass of atom I.

This quasiharmonic approximation is quite accurate and gives results that are in good agreements with the Monte Carlo simulations [49]. However, the diagonalization of the $3N \times 3N$ matrix is computationally expensive. In order to avoid this difficulty, the local harmonic approximation [50] has been introduced to neglect coupled vibration of different atoms. Consequently, the atomic-level free energy is expressed as:

$$F_H = W_C(\mathbf{F}) + \kappa_B T \sum_{I=1}^{N} \sum_{k=1}^{3} \ln\left[2\sinh\left(\frac{\hbar \omega_{Ik}}{2\kappa_B T} \right) \right] \tag{3.8}$$

Foiles [49] and Najafabadi et al. [51] evaluated the accuracy of local harmonic approximation and concluded that, even though the local harmonic approximation somewhat underestimates the temperature dependence, it still provides a reasonable compromise between accuracy and computational demands. However, they also pointed out that the accuracy of this approximation is sensitive to the anharmonicities in interatomic potentials.

LeSar et al. further introduced the high-temperature classical limit [50],

$$\sinh\left(\frac{\hbar \omega_{Ik}}{2\kappa_B T} \right) \approx \frac{\hbar \omega_{Ik}}{2\kappa_B T} \tag{3.9}$$

such that the Helmholtz free energy in Eq. (3.8) becomes

$$F_H = W_C(\mathbf{F}) + n\kappa_B T \sum_{I=1}^{N} \ln\left(\frac{\hbar \bar{D}_I^{\frac{1}{2n}}}{\kappa_B T} \right) \tag{3.10}$$

where

$$D_I = \frac{1}{m_I}\left(\frac{\partial^2 W_C}{\partial x_{I\alpha} \partial x_{I\beta}} \right) \tag{3.11}$$

is the local dynamical matrix and

$$\bar{D}_I = \left(\prod_k^n \omega_{Ik} \right)^2 \tag{3.12}$$

is the determinant of the local dynamical matrix, where n is the number of degrees of freedom per atom.

In continuum approach to a crystalline solid with the TCB rule, we assume that atoms not only have locally homogeneous deformation as in the conventional CB rule but also have the same vibration mode locally [52] at a given temperature. Therefore, all the local atoms have the same dynamical matrix that is a function of the deformation gradient.

In summary, the proposed TCB rule assumes:

1) atoms have locally homogeneous deformation;

2) the vibration of atoms is harmonic;

3) atoms have the same local vibration modes;

4) coupled vibration of different atoms is negligible.

In the continuum model of a crystalline solid that contains N atoms at a temperature field of $T(\mathbf{X})$, the total free energy, W_H, of the crystalline solid with the continuum model can be expressed as follows,

$$\begin{aligned} W_H(\mathbf{F},T) &= \int_\Omega w_C(\mathbf{F}) d\Omega + n\kappa_B \int_\Omega \rho_n T \ln\left[\frac{\hbar\left(\bar{D}(\mathbf{F})\right)^{\frac{1}{2n}}}{\kappa_B T} \right] d\Omega \\ &= \sum_i^{N_q} w_C\left(\mathbf{F}_i^q\right) A_i + n\kappa_B \sum_i^{N_q} n_i^q T_i^q \ln\left[\frac{\hbar\left(\bar{D}\left(\mathbf{F}_i^q\right)\right)^{\frac{1}{2n}}}{\kappa_B T_i^q} \right] \end{aligned} \tag{3.13}$$

where ρ_n is the number of atoms per unit volume; N_q is the number of quadrature points in the continuum model; and A_i is the volume associated with one quadrature point, X_i^q,

which represents n_i^q atoms. The first term on the RHS of the above equation is the continuum level strain energy when temperature equals to zero. In the continuum model, the deformation gradient and the temperature are evaluated at each quadrature point. With the TCB technique, all the bonds and atoms in A_i are assumed to be at the same deformation and temperature. Consequently, the strain energy density and the dynamical matrix can be calculated using the unit cell model for each quadrature point.

As a difference from other research [22, 28, 45, 46, 53], we modify Eq. (3.3) to calculate the continuum-level nominal stress for continuum approach to finite-temperature nano systems as follows,

$$\mathbf{P}\left(\mathbf{F},T\right)=\frac{\partial w_H\left(\mathbf{F},T\right)}{\partial \mathbf{F}^{\mathrm{T}}} \tag{3.14}$$

where w_H is the free energy density. It can be written as

$$w_H\left(\mathbf{F},T\right)=\frac{1}{V_0}W_H\left(\mathbf{F},T\right) \tag{3.15}$$

and is a function of the deformation gradient and the temperature, where V_0 is the system volume. In a periodic nanostructure, we always calculate the free energy density in a unit cell. In this case, W_H and V_0 are the total free energy and volume of the unit cell respectively. Eq. (3.14) can serve as a temperature-related constitutive relation that is implemented in most hierarchical and concurrent multiscale methods to investigate temperature-related physical behavior of nanostructured materials.

3.3 Verification of the TCB Rule

To verify the proposed TCB rule, we perform stress analyses of various crystalline solids at any given deformation gradient and temperature using the continuum

approximation with the TCB rule. Then, we compare the continuum-level Cauchy stresses with the atomic-level ones (Appendix D) from molecular simulations. It should be noted here that the simulated objects are assumed to be canonical ensembles subject to any given deformation and temperature. Both Monte Carlo method and molecular dynamics are feasible to result in the same stress state of canonical ensembles at thermal equilibrium. In this thesis, we employ molecular dynamics (Appendix A) with the periodic boundary conditions and the Berendsen thermostat [54] (Appendix B).

3.3.1 One-dimensional Molecule Chain

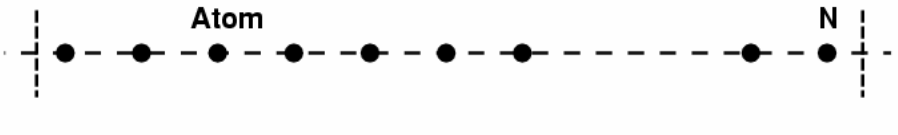

Figure 3.1: One-dimensional molecule chain

We first consider a one-dimensional molecule chain, which contains 100 atoms, each of which has a mass of $m_0 = 1.993\times10^{-26}\,\mathrm{kg}$. The following Lennard-Jones 6-12 potential function is employed to describe the interatomic interaction between nearest neighbored atoms

$$\varphi(l) = 4\varepsilon\left[\frac{1}{4}\left(\frac{l_0}{l}\right)^{12} - \frac{1}{2}\left(\frac{l_0}{l}\right)^{6}\right] \tag{3.16}$$

where $l_0 = 1\mathrm{nm}$ is the undeformed bond length, and $\varepsilon = 8.25\times10^{-18}\,\mathrm{J}$ is the depth of the energy well. Fig. 3.1 gave the geometry of the one-dimensional molecule chain. In this model we have N atoms or molecules in total. When this molecular chain is under a

deformation gradient of F , which is a scalar in one dimension, the length of the deformed bond is $l = Fl_0$ since the deformation is assumed to be homogeneous.

The unit cell of this molecule chain contains one atom and two half-bonds. The free energy density for this unit cell under temperature T can be calculated as

$$\begin{aligned} w_H &= \frac{1}{l_0}\left\{\varphi(l) + \kappa_B T \ln\left[\frac{\hbar\sqrt{\bar{D}}}{\kappa_B T}\right]\right\} \\ &= \frac{1}{l_0}\left\{\varphi(l) + \kappa_B T\left[\ln\left(\frac{\hbar}{\kappa_B T}\right) + \frac{1}{2}\ln(\varphi'') - \frac{1}{2}\ln(m_0)\right]\right\} \end{aligned} \tag{3.17}$$

where $\bar{D}$ is the determinant of the dynamical matrix which can be written as

$$\bar{D} = \frac{1}{m_0}\frac{\partial^2\varphi}{\partial x^2} = \frac{1}{m_0}\frac{\partial^2\varphi}{\partial l^2} = \frac{\varphi''}{m_0} \tag{3.18}$$

The nominal stress, derived from the free energy density can be calculated as

$$\begin{aligned} \sigma^C = P &= \frac{\partial w_H}{\partial F} = \frac{\partial w_H}{\partial l}\frac{\partial l}{\partial F} \\ &= \frac{1}{l_0}\left\{\varphi'(l) + \frac{\partial}{\partial l}\left[\frac{1}{2}\kappa_B T \ln(\varphi'')\right]\right\} l_0 \\ &= \varphi'(l) + \frac{1}{2}\kappa_B T\frac{\varphi'''(l)}{\varphi''(l)} \end{aligned} \tag{3.19}$$

Fig. 3.2 shows the comparison of atomic-level and continuum-level Cauchy stresses with temperatures when a given deformation gradient is applied on the molecule chain. Molecular dynamics elucidates that the lower stress is obtained at a higher temperature due to the thermal expansion. However, since the continuum approximation with the conventional CB rule does not include temperature effects, its derived Cauchy stresses are independent of the temperature and become a constant in Fig. 3.2. When the TCB rule is employed, the Cauchy stresses are temperature-related and are in accord with molecular dynamics results very well.

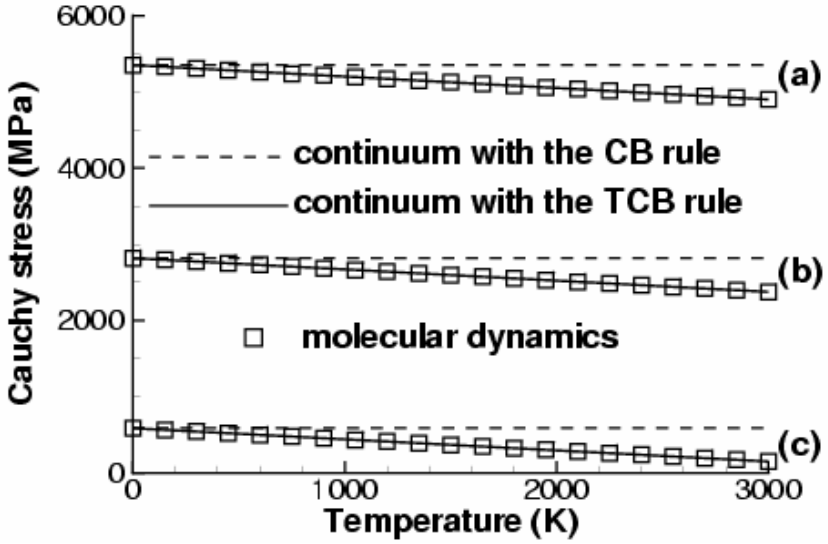

(a) $F = 1.001$; (b) $F = 1.005$; (c) $F = 1.01$

Figure 3.2: Comparison of Cauchy stress with temperature in molecule chain

3.3.2 Two-dimensional Hexagonal-triangular Lattice

We then study a plate of two-dimensional Lennard-Jones crystal with a hexagonal-triangular lattice as shown in Fig. 3.3. This molecular structure was used by Gao [59] to study the local limiting speed in dynamic fractures. The nanoplate contains 1116 atoms, and its length and width are 30nm, respectively. The interatomic Lennard-Jones 6-12 potential and its parameters are the same as in Eq. (3.16). When the nanoplate undergoes a deformation gradient, $\mathbf{F} = \begin{bmatrix} F_{11} & F_{12} \\ F_{21} & F_{22} \end{bmatrix}$, all the unit cells are assumed to be deformed identically, and all the atoms have the same harmonic vibration mode via the TCB rule. Therefore, the strain energy density at the temperature of 0K can be calculated

from the potential of the unit cell, as well as the dynamical matrix of the atom located in the center of the unit cell. From Fig. 3.3, we can see that there are 2 atoms in the unit cell, including one whole atom in the center and 4 quarter-atoms shared with adjacent unit cells on the boundary. And there are 6 bonds, including 4 whole bonds and 4 half-bonds which are also shared with neighboring unit cell on the boundary. For each atom, there are 6 bonds connected to it but also shared with other adjacent atoms. So, there are 3 independent bonds for each atom in average which are shown in Fig. 3.4. The area for a unit cell is $A_0 = \sqrt{3} l_0^2$, so if we only consider the pair-potentials, the strain energy density calculated from unit cell is

$$w_C = \frac{2}{\sqrt{3} l_0^2} \left[\varphi(l_1) + \varphi(l_2) + \varphi(l_3) \right] \tag{3.20}$$

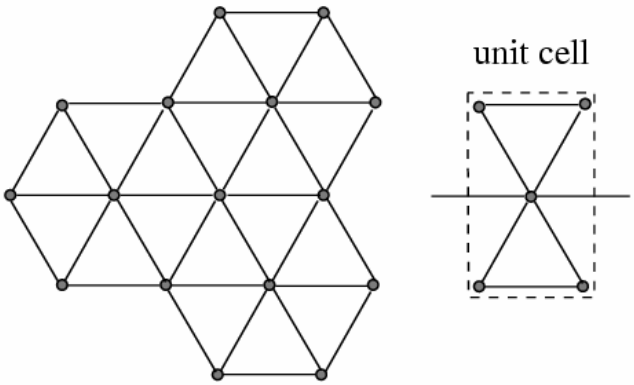

Figure 3.3: A two-dimensional crystal with a hexagonal-triangular lattice

The local dynamical matrix for the atom located in the center of the unit cell in Eq. (3.11), can also be computed from the second derivative of strain energy density with respect to the material coordinates. They are:

$$D_{ij} = \sum_{k=1}^{3} \left[\varphi''(l_k) \frac{r_{ki} r_{kj}}{l_k^2} - \varphi'(l_k) \frac{r_{ki} r_{kj}}{l_k^3} + \frac{\varphi'(l_k)}{l_k} \delta_{ij} \right] \tag{3.21}$$

where $l_k = \sqrt{r_{k1}^2 + r_{k2}^2}$ $(k = 1,2,3)$ and

$$r_{11} = F_{11} l_0 ,\ r_{12} = F_{12} l_0$$

$$r_{21} = \left(\frac{1}{2} F_{11} - \frac{\sqrt{3}}{2} F_{12} \right) l_0 ,\ r_{22} = \left(\frac{1}{2} F_{21} - \frac{\sqrt{3}}{2} F_{22} \right) l_0 , \tag{3.22}$$

$$r_{31} = \left(\frac{1}{2} F_{11} + \frac{\sqrt{3}}{2} F_{12} \right) l_0 ,\ r_{32} = \left(\frac{1}{2} F_{21} + \frac{\sqrt{3}}{2} F_{22} \right) l_0$$

Here we omit the mass and volume parts in the dynamical matrix, since scalar parameters in logarithm function do not affect the result in the derivatives. We will keep this explicit notation unless we mention.

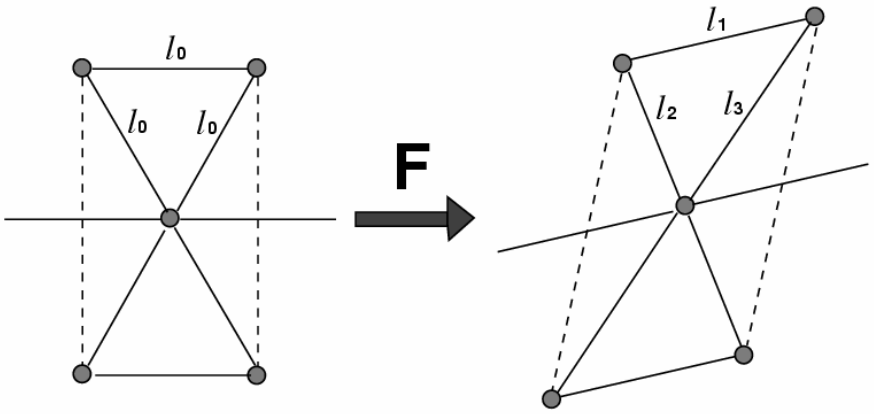

Figure 3.4: Deformation of a unit cell of the hexagonal-triangular lattice

The free energy density can be computed as

$$w_H = w_C + \frac{4}{\sqrt{3}l_0^2}\kappa_B T \ln\left(\frac{\hbar \bar{D}^{1/4}}{\kappa_B T}\right) \tag{3.23}$$

Then, the continuum-level nominal stress, from Eq. (3.14), is

$$\mathbf{P} = \frac{\partial w_C}{\partial \mathbf{F}^{\mathrm{T}}} + \frac{\kappa_B T}{\sqrt{3}\bar{D}l_0^2}\frac{\partial \bar{D}}{\partial \mathbf{F}^{\mathrm{T}}} \tag{3.24}$$

The first term on RHS is the nominal stress from traditional CB rule. Using Eq. (3.20), it can be written further as

$$\frac{\partial w_C}{\partial \mathbf{F}^{\mathrm{T}}} = \frac{2}{\sqrt{3}l_0^2}\sum_k^3 \left[\varphi'(l_k)\frac{\partial l_k}{\partial \mathbf{F}^{\mathrm{T}}}\right] \tag{3.25}$$

We only keep the normal vibration modes and omit the off-diagonal components in dynamical matrix since they are pretty small compare to the diagonal parts. So, in a two-dimensional lattice

$$\bar{D} = D_{11}D_{22} \tag{3.26}$$

and

$$\frac{\partial \bar{D}}{\partial \mathbf{F}^{\mathrm{T}}} = \frac{\partial D_{11}}{\partial \mathbf{F}^{\mathrm{T}}}D_{22} + D_{11}\frac{\partial D_{22}}{\partial \mathbf{F}^{\mathrm{T}}} \tag{3.27}$$

The first derivative of the diagonal components with respect to the deformation gradient, from Eq. (3.21), is

$$\begin{aligned}\frac{\partial D_{ii}}{\partial \mathbf{F}^{\mathrm{T}}} = \sum_k \Bigg[& \varphi'''(l_k)\left(\frac{r_{ki}}{l_k}\right)^2 \frac{\partial l_k}{\partial \mathbf{F}^{\mathrm{T}}} + 2\varphi''(l_k)\frac{r_{ki}}{l_k^2}\frac{\partial r_{ki}}{\partial \mathbf{F}^{\mathrm{T}}} - 3\varphi''(l_k)\frac{r_{ki}^2}{l_k^3}\frac{\partial l_k}{\partial \mathbf{F}^{\mathrm{T}}} \\ & + \varphi''(l_k)\frac{1}{l_k}\frac{\partial l_k}{\partial \mathbf{F}^{\mathrm{T}}} + 3\varphi'(l_k)\frac{r_{ki}^2}{l_k^4}\frac{\partial l_k}{\partial \mathbf{F}^{\mathrm{T}}} - \varphi'(l_k)\frac{1}{l_k^2}\frac{\partial l_k}{\partial \mathbf{F}^{\mathrm{T}}} - 2\varphi'(l_k)\frac{r_{ki}}{l_k^3}\frac{\partial r_{ki}}{\partial \mathbf{F}^{\mathrm{T}}}\Bigg]\end{aligned} \tag{3.28}$$

The atomic-level and continuum-level Cauchy stresses are computed via Eq. (D.1) and Eq. (D.5) (Appendix D) for any given deformation gradient and temperature. Fig. 3.4

shows the comparison of each component of Cauchy stresses at various temperatures when two different deformation gradients are given. We also calculate Cauchy stresses using the continuum model with the conventional CB rule to demonstrate the advantages of the TCB rule. The continuum approximation with the conventional CB rule gives constant stresses at different temperatures since temperature effects are not considered in the CB rule. If temperature effects are considered, the continuum-level normal stresses, calculated based on the TCB rule, decrease with the increasing temperature due to thermal expansion. The results agree with the molecular dynamics solutions. Shear stresses calculated from continuum approximations with either the conventional CB or the TCB rule are supported by molecular dynamics simulation because temperature has no effects on shear stresses.

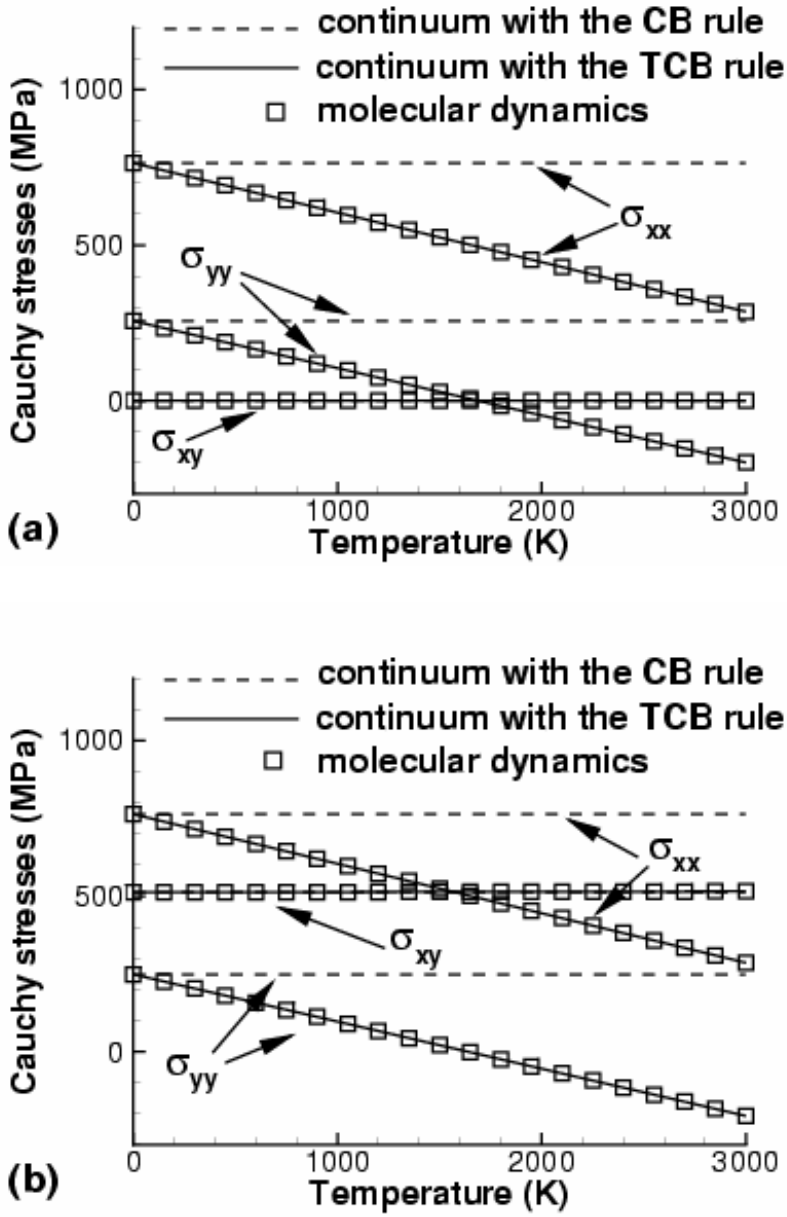

(a) $\mathbf{F} = \begin{bmatrix} 1.001 & 0.0 \\ 0.0 & 1.0 \end{bmatrix}$; (b) $\mathbf{F} = \begin{bmatrix} 1.001 & 0.002 \\ 0.0 & 1.0 \end{bmatrix}$

Figure 3.5: Cauchy stress components with temperature in the hexagonal-triangular lattice

3.3.3 Graphene Sheet

As a more practical example, we consider temperature effects on stress analysis of the graphene sheet. Fig. 3.6 shows the honeycomb multi-lattice of a graphene sheet with its unit cell in the dashed box. There are three inequivalent bonds, $\mathbf{A}_{0i}$ $(i=1,2,3)$ in the reference configuration, i.e. the undeformed configuration. It should be noted that the graphene sheet as a Bravais multi-lattice, has two basic nuclei: a black dot and a white dot shown in Fig. 3.6. Consequently, when the graphene sheet is subject to a homogeneous deformation, one cannot use only one basic nucleus and two simple Bravais lattice vectors to define the entire lattice. Therefore, a shift vector, $\boldsymbol{\eta}$, known as the inner displacement [55], must be introduced as shown in Fig. 3.6 to define the relative displacement of the basic nuclei. The inner displacement represents an internal model of deformation in the unit cell instead of the homogeneous deformation sustained by the entire graphene sheet. Then, the deformed lattice vectors $\mathbf{l}_i$ is written as

$$\mathbf{l}_i = \mathbf{l}_{0i} + \boldsymbol{\eta} \tag{3.29}$$

Since inner displacements are in the internal equilibrium, we neglect the temperature effects on inner displacements. Similarly to [55], the inner displacement is calculated by minimizing the strain energy density with respect to $\boldsymbol{\eta}$ for a given deformation of the lattice, i.e.

$$\boldsymbol{\eta}(\mathbf{F}) = \arg\left(\min_{\boldsymbol{\eta}} w_C(\mathbf{F},\boldsymbol{\eta})\right) \Rightarrow \left.\frac{\partial w_C(\mathbf{F},\boldsymbol{\eta})}{\partial \boldsymbol{\eta}}\right|_{\mathbf{F}} = 0 \tag{3.30}$$

When a graphene sheet is subject to a homogeneous deformation and a particular temperature, the positions of the atoms in the current configuration, i.e. the deformed

configuration, are expressed in terms of the deformation gradient $\mathbf{F}$ and the inner displacement $\boldsymbol{\eta}$. Therefore, the total free energy of the graphene sheet is computed as

$$W_H\left(\mathbf{F},T,\boldsymbol{\eta}\right)=A_0 w_C\left(\mathbf{F},\boldsymbol{\eta}\right)+nN\kappa_B T\ln\left[\frac{\hbar\left(\bar{D}\left(\mathbf{F},\boldsymbol{\eta}\right)\right)^{\frac{1}{2n}}}{\kappa_B T}\right] \tag{3.31}$$

where A_0 is the area of the simulated graphene sheet, and N is the total carbon atoms.

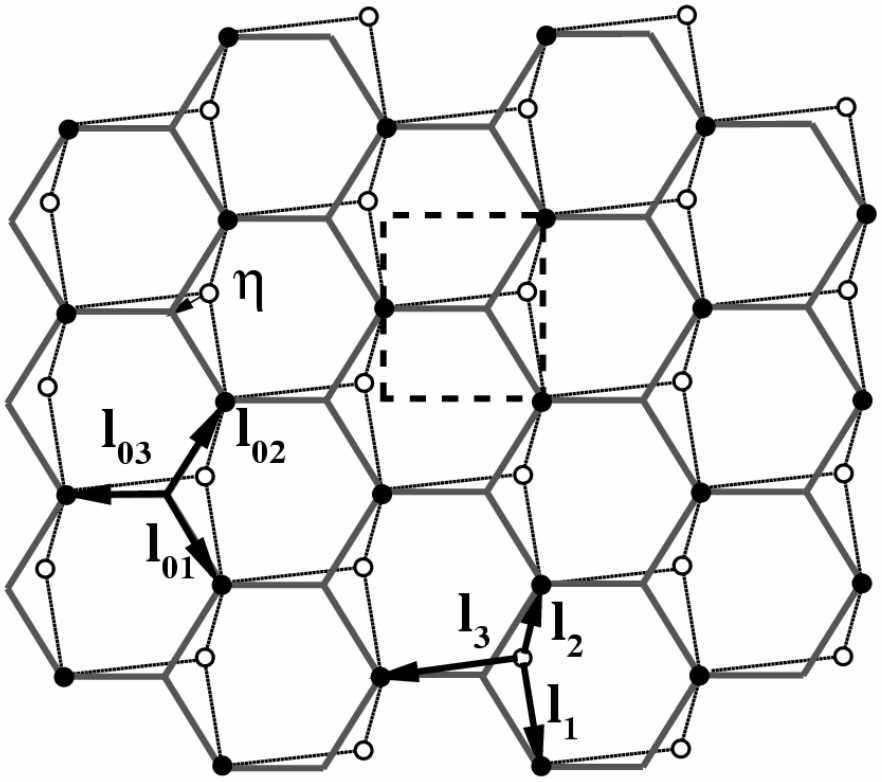

Figure 3.6: A graphene sheet and its unit cell

The inner displacement can be eliminated at the constitutive level using Eq. (3.30). After this inner relaxation, the total free energy can be written as a function of $\mathbf{F}$ and T only

$$\hat{W}_H\left(\mathbf{F},T\right)=W_H\left(\mathbf{F},T,\hat{\boldsymbol{\eta}}\left(\mathbf{F}\right)\right) \tag{3.32}$$

Note that, while a closed form expression for the potential W_H is available, the evaluation of $\hat{W}_H\left(\mathbf{F},T\right)$ requires the solution of a bivariate minimization problem, which can be solved numerically by Newton's method or Conjugate Gradient method (Appendix C). The nominal stress, which the first derivative of the free energy density, can be benefit from the inner relaxation,

$$\mathbf{P}\left(\mathbf{F},T\right)=\frac{\partial\hat{w}_H}{\partial\mathbf{F}^{\mathrm{T}}}=\left.\frac{\partial w_H}{\partial\mathbf{F}^{\mathrm{T}}}\right|_{\boldsymbol{\eta}=\hat{\boldsymbol{\eta}}} \tag{3.33}$$

where $w_H=\dfrac{W_H}{A_0}$ is the density of free energy, and therefore this derivative can be computed in closed-form from the function W_H.

Since the effects from the angle-bending potential are significant in the graphene sheet, we need to consider both band-stretching potential and angle-bending potential. We use a modified Morse potential function [56] as the follows to describe the interatomic interaction,

$$\begin{aligned}
&\varphi\left(l,\theta\right)=\varphi_s\left(l\right)+\varphi_a\left(\theta\right)\\
&\varphi_s=D_e\left\{\left[1-e^{-\beta\left(l-l_0\right)}\right]^2-1\right\}\\
&\varphi_a=\frac{1}{2}k_\theta\left(\theta-\theta_0\right)^2\left[1+k_s\left(\theta-\theta_0\right)^4\right]
\end{aligned} \tag{3.34}$$

where φ_s is the bond energy due to bond stretching or compressing, φ_a is the bond energy due to bond angle-bending, l is the current bond length, and θ is the angle of two adjacent bonds representing a standard deformation measure in molecular mechanics.

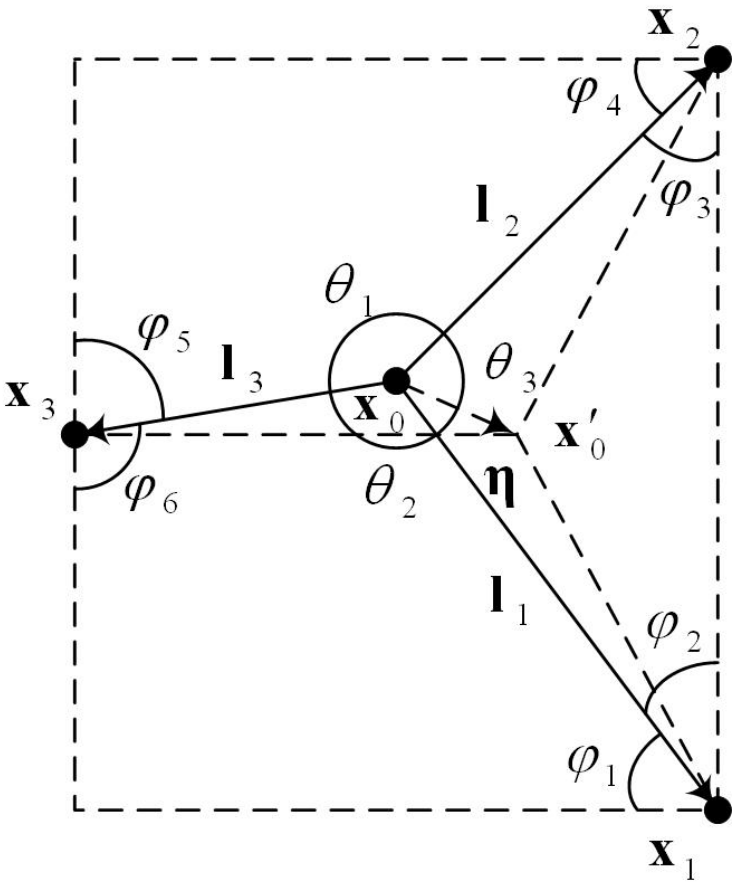

Figure 3.7: Unit cell of grapheme sheet

From the zoom in of the unit cell, which is Fig. 3.7, we can see that there are 2 atoms in the unit cell, including one whole atom in the center, 1 half-atom on the right boundary and 2 quarter-atoms on the left boundary shared with adjacent unit cells. And there are 3 whole bonds in the unit cell, which means for each atom, there are 1.5 bonds in average. Also, there are 9 angles in the unit cell, which are θ_1 to θ_3 and φ_1 to φ_6. But they are not all independent. From the geometry, we can obtain

$$\begin{aligned} \theta_1 &= \varphi_3 + \varphi_6 \\ \theta_2 &= \varphi_2 + \varphi_5 \\ \theta_3 &= \varphi_1 + \varphi_4 \end{aligned} \tag{3.35}$$

That means for each atom, only three of the angles, θ_1 to θ_3 are independent.

$\mathbf{x}_0$ to $\mathbf{x}_3$ are the realistic positions of the atoms while $\mathbf{x}_0'$ is the position for the central atom if there is no inner displacement (internal shift) vector $\boldsymbol{\eta}$. Follow the geometry, we can obtain

$$\mathbf{x}_0 = \mathbf{x}_0' - \boldsymbol{\eta} \tag{3.36}$$

and

$$\mathbf{l}_1 = \mathbf{x}_1 - \mathbf{x}_0 = \begin{Bmatrix} r_{11} \\ r_{12} \end{Bmatrix} l_0 + \boldsymbol{\eta} = \begin{Bmatrix} \frac{1}{2}F_{11} - \frac{\sqrt{3}}{2}F_{12} \\ \frac{1}{2}F_{21} - \frac{\sqrt{3}}{2}F_{22} \end{Bmatrix} l_0 + \boldsymbol{\eta} \tag{3.37}$$

$$\mathbf{l}_2 = \mathbf{x}_2 - \mathbf{x}_0 = \begin{Bmatrix} r_{21} \\ r_{22} \end{Bmatrix} l_0 + \boldsymbol{\eta} = \begin{Bmatrix} \frac{1}{2}F_{11} + \frac{\sqrt{3}}{2}F_{12} \\ \frac{1}{2}F_{21} + \frac{\sqrt{3}}{2}F_{22} \end{Bmatrix} l_0 + \boldsymbol{\eta} \tag{3.38}$$

$$\mathbf{l}_3 = \mathbf{x}_3 - \mathbf{x}_0 = \begin{Bmatrix} r_{31} \\ r_{32} \end{Bmatrix} l_0 + \boldsymbol{\eta} = \begin{Bmatrix} -F_{11} \\ -F_{21} \end{Bmatrix} l_0 + \boldsymbol{\eta} \tag{3.39}$$

For the angles, we can obtain

$$\theta_1 = \arccos\left(\frac{\mathbf{l}_2 \square \mathbf{l}_3}{l_2 l_3} \right) \tag{3.40}$$

$$\theta_2 = \arccos\left(\frac{\mathbf{l}_3 \square \mathbf{l}_1}{l_3 l_1} \right) \tag{3.41}$$

$$\theta_3 = \arccos\left(\frac{\mathbf{l}_1 \square \mathbf{l}_2}{l_1 l_2} \right) \tag{3.42}$$

where l_1, l_2, l_3 are the length of $\mathbf{l}_1$, $\mathbf{l}_2$ and $\mathbf{l}_3$, $(\square)$ denotes the inner product of two vectors, for example, in a two-dimensional problem

$$\mathbf{l}_m \square \mathbf{l}_n = l_m^1 l_n^1 + l_m^2 l_n^2 \tag{3.43}$$

The area for a unit cell is $A_0 = \frac{3\sqrt{3}}{2} l_0^2$. So, the nominal stresses can be written as

$$\mathbf{P} = \frac{\partial w_C}{\partial \mathbf{F}^{\mathrm{T}}} + \frac{\kappa_B T}{3\sqrt{3}\bar{D} l_0^2} \frac{\partial \bar{D}}{\partial \mathbf{F}^{\mathrm{T}}} \tag{3.44}$$

where w_C and $\mathbf{D}$ are the function of the potentials from both bond stretching and angle bending. They can be written as

$$w_C = \frac{1}{A_0} \left\{ \frac{1}{2} \sum_k^3 \left[\varphi_s \left(l_k \right) \right] + \sum_k^3 \left[\varphi_a \left(\theta_k \right) \right] \right\} \tag{3.45}$$

$$D_{ij} = D_{ij}^s + D_{ij}^a = \frac{\partial^2}{\partial x_0^i \partial x_0^j} \left\{ \frac{1}{2} \sum_k^3 \left[\varphi_s \left(l_k \right) \right] \right\} + \frac{\partial^2}{\partial x_0^i \partial x_0^j} \left\{ \sum_k^3 \left[\varphi_a \left(\theta_k \right) \right] \right\} \tag{3.46}$$

where x_0^i and x_0^j are the i and j component of vector $\mathbf{x}_0$.

The calculations of the first term on the RHS of Eq. (3.45) and Eq. (3.46) are similar to what we showed in previous section. Here we only derive the formula for the second term. The nominal stress from strain energy at $0K$ can be obtained by

$$\mathbf{P}_s = \frac{1}{A_0} \frac{\partial}{\partial \mathbf{F}^{\mathrm{T}}} \sum_k^3 \left[\varphi_a \left(\theta_k \right) \right] = \frac{1}{A_0} \sum_k^3 \left[\varphi' \left(\theta_k \right) \frac{\partial \theta_k}{\partial \mathbf{F}^{\mathrm{T}}} \right] \tag{3.47}$$

where

$$\frac{\partial \theta_k}{\partial \mathbf{F}^{\mathrm{T}}} = -\frac{1}{\sqrt{1 - \cos^2 \theta_k}} \frac{\partial \cos \theta_k}{\partial \mathbf{F}^{\mathrm{T}}} \tag{3.48}$$

and

$$\begin{aligned} \frac{\partial \cos \theta_k}{\partial \mathbf{F}^{\mathrm{T}}} = & \frac{1}{l_m l_n} \left(r_{m1} \frac{\partial r_{n1}}{\partial \mathbf{F}^{\mathrm{T}}} + r_{n1} \frac{\partial r_{m1}}{\partial \mathbf{F}^{\mathrm{T}}} + r_{m2} \frac{\partial r_{n2}}{\partial \mathbf{F}^{\mathrm{T}}} + r_{n2} \frac{\partial r_{m2}}{\partial \mathbf{F}^{\mathrm{T}}} \right) \\ & - \frac{\mathbf{l}_m \square \mathbf{l}_n}{l_m^2 l_n^2} \left(l_m \frac{\partial l_n}{\partial \mathbf{F}^{\mathrm{T}}} + l_n \frac{\partial l_m}{\partial \mathbf{F}^{\mathrm{T}}} \right) \end{aligned} \tag{3.49}$$

Here *m* and *n* are the indices of the bonds belong to angle θ_k. For the nominal stress from temperature part, the elimination of the off-diagonal components is also conducted in the dynamical matrix to simplify the expression.

$$D_{ii}^{a}=\sum_{k}^{3}\left[\frac{\partial^{2}\varphi^{a}}{\partial\theta_{k}^{2}}\left(\frac{\partial\theta_{k}}{\partial x_{0}^{i}}\right)^{2}+\frac{\partial\varphi^{a}}{\partial\theta_{k}}\frac{\partial^{2}\theta_{k}}{\partial\left(x_{0}^{i}\right)^{2}}\right] \tag{3.50}$$

where

$$\frac{\partial\theta_{k}}{\partial x_{0}^{i}}=-\frac{1}{\sqrt{1-\cos^{2}\theta_{k}}}\frac{\partial\cos\theta_{k}}{\partial x_{0}^{i}} \tag{3.51}$$

and

$$\frac{\partial^{2}\theta_{k}}{\partial\left(x_{0}^{i}\right)^{2}}=-\left(1-\cos^{2}\theta_{k}\right)^{-\frac{1}{2}}\frac{\partial^{2}\cos\theta_{k}}{\partial\left(x_{0}^{i}\right)^{2}}-\left(1-\cos^{2}\theta_{k}\right)^{-\frac{3}{2}}\cos\theta_{k}\left(\frac{\partial\cos\theta_{k}}{\partial x_{0}^{i}}\right)^{2} \tag{3.52}$$

The derivatives of $\cos\theta_k$ with respect to x_0^i are

$$\frac{\partial\cos\theta_{k}}{\partial x_{0}^{i}}=\frac{1}{l_{m}l_{n}}\left(r_{mi}+r_{ni}\right)-\frac{\mathbf{l}_{m}\square\mathbf{l}_{n}}{l_{m}^{2}l_{n}^{2}}\left(\frac{l_{m}}{l_{n}}r_{ni}+\frac{l_{n}}{l_{m}}r_{mi}\right) \tag{3.53}$$

and

$$\begin{aligned}\frac{\partial^{2}\cos\theta_{k}}{\partial\left(x_{0}^{i}\right)^{2}}=&\frac{2}{l_{m}l_{n}}-\frac{2\left(r_{mi}+r_{ni}\right)}{l_{m}^{3}l_{n}^{3}}\left(l_{m}^{2}r_{ni}+l_{n}^{2}r_{mi}\right)\\&+\frac{\mathbf{l}_{m}\square\mathbf{l}_{n}}{l_{m}^{2}l_{n}^{2}}\left(\frac{3l_{n}r_{mi}^{2}}{l_{m}^{3}}+\frac{3l_{m}r_{ni}^{2}}{l_{n}^{3}}+\frac{2r_{mi}r_{ni}}{l_{m}l_{n}}-\frac{l_{m}}{l_{n}}-\frac{l_{n}}{l_{m}}\right)\end{aligned} \tag{3.54}$$

And the derivative of the dynamical matrix with respect to the deformation gradient can be calculated through

$$\frac{\partial D_{ii}^{a}}{\partial \mathbf{F}^{\mathrm{T}}}=\sum_{k}^{3}\left[\frac{\partial}{\partial \mathbf{F}^{\mathrm{T}}}\left(\frac{\partial^{2}\varphi_{a}}{\partial\theta_{k}^{2}}\right)\left(\frac{\partial\theta_{k}}{\partial x_{0}^{i}}\right)^{2}+2\frac{\partial^{2}\varphi_{a}}{\partial\theta_{k}^{2}}\frac{\partial\theta_{k}}{\partial x_{0}^{i}}\frac{\partial}{\partial \mathbf{F}^{\mathrm{T}}}\left(\frac{\partial\theta_{k}}{\partial x_{0}^{i}}\right)\right.$$
$$\left.+\frac{\partial}{\partial \mathbf{F}^{\mathrm{T}}}\left(\frac{\partial\varphi_{a}}{\partial\theta_{k}}\right)\frac{\partial^{2}\theta_{k}}{\partial\left(x_{0}^{i}\right)^{2}}+\frac{\partial\varphi_{a}}{\partial\theta_{k}}\frac{\partial}{\partial \mathbf{F}^{\mathrm{T}}}\left(\frac{\partial^{2}\theta_{k}}{\partial\left(x_{0}^{i}\right)^{2}}\right)\right] \tag{3.55}$$

where

$$\frac{\partial}{\partial \mathbf{F}^{\mathrm{T}}}\left(\frac{\partial\varphi_{a}}{\partial\theta_{k}}\right)=\varphi_{a}''\left(l_{k}\right)\frac{\partial\theta_{k}}{\partial \mathbf{F}^{\mathrm{T}}} \tag{3.56}$$

$$\frac{\partial}{\partial \mathbf{F}^{\mathrm{T}}}\left(\frac{\partial^{2}\varphi_{a}}{\partial\theta_{k}^{2}}\right)=\varphi_{a}'''\left(l_{k}\right)\frac{\partial\theta_{k}}{\partial \mathbf{F}^{\mathrm{T}}} \tag{3.57}$$

$$\frac{\partial}{\partial \mathbf{F}^{\mathrm{T}}}\left(\frac{\partial\theta_{k}}{\partial x_{0}^{i}}\right)=-\left(1-\cos^{2}\theta_{k}\right)^{-\frac{1}{2}}\frac{\partial}{\partial \mathbf{F}^{\mathrm{T}}}\left(\frac{\partial\cos\theta_{k}}{\partial x_{0}^{i}}\right)$$
$$-\left(1-\cos^{2}\theta_{k}\right)^{-\frac{3}{2}}\cos\theta_{k}\frac{\partial\cos\theta_{k}}{\partial x_{0}^{i}}\frac{\partial\cos\theta_{k}}{\partial \mathbf{F}^{\mathrm{T}}} \tag{3.58}$$

and

$$\frac{\partial}{\partial \mathbf{F}^{\mathrm{T}}}\left(\frac{\partial^{2}\theta_{k}}{\partial\left(x_{0}^{i}\right)^{2}}\right)=-\left(1-\cos^{2}\theta_{k}\right)^{-\frac{1}{2}}\frac{\partial}{\partial \mathbf{F}^{\mathrm{T}}}\left(\frac{\partial^{2}\cos\theta_{k}}{\partial\left(x_{0}^{i}\right)^{2}}\right)$$
$$-\left(1-\cos^{2}\theta_{k}\right)^{-\frac{3}{2}}\cos\theta_{k}\frac{\partial^{2}\cos\theta_{k}}{\partial\left(x_{0}^{i}\right)^{2}}\frac{\partial\cos\theta_{k}}{\partial \mathbf{F}^{\mathrm{T}}}$$
$$-2\left(1-\cos^{2}\theta_{k}\right)^{-\frac{3}{2}}\cos\theta_{k}\frac{\partial\cos\theta_{k}}{\partial x_{0}^{i}}\frac{\partial}{\partial \mathbf{F}^{\mathrm{T}}}\left(\frac{\partial\cos\theta_{k}}{\partial x_{0}^{i}}\right) \tag{3.59}$$
$$-\left[\left(1-\cos^{2}\theta_{k}\right)^{-\frac{3}{2}}+3\left(1-\cos^{2}\theta_{k}\right)^{-\frac{5}{2}}\cos^{2}\theta_{k}\right]\left(\frac{\partial\cos\theta_{k}}{\partial x_{0}^{i}}\right)^{2}\frac{\partial\cos\theta_{k}}{\partial \mathbf{F}^{\mathrm{T}}}$$

The derivatives of $\cos\theta_{k}$ with respect to x_{0}^{i} and $\mathbf{F}^{\mathrm{T}}$ are

$$\begin{aligned}\frac{\partial}{\partial \mathbf{F}^{\mathrm{T}}}\left(\frac{\partial \cos\theta_k}{\partial x_0^i}\right) &= \frac{1}{l_m l_n}\left(\frac{\partial r_{mi}}{\partial \mathbf{F}^{\mathrm{T}}}+\frac{\partial r_{ni}}{\partial \mathbf{F}^{\mathrm{T}}}\right)-\frac{1}{l_m^2 l_n^2}\left[\left(r_{mi}+r_{ni}\right)\left(l_m\frac{\partial l_n}{\partial \mathbf{F}^{\mathrm{T}}}+l_n\frac{\partial l_m}{\partial \mathbf{F}^{\mathrm{T}}}\right)\right.\\ &\left.+\left(\frac{l_n r_{mi}}{l_m}+\frac{l_m r_{ni}}{l_n}\right)\left(r_{m1}\frac{\partial r_{n1}}{\partial \mathbf{F}^{\mathrm{T}}}+r_{n1}\frac{\partial r_{m1}}{\partial \mathbf{F}^{\mathrm{T}}}+r_{m2}\frac{\partial r_{n2}}{\partial \mathbf{F}^{\mathrm{T}}}+r_{n2}\frac{\partial r_{m2}}{\partial \mathbf{F}^{\mathrm{T}}}\right)\right]\\ &+\frac{\mathbf{l}_m\square\mathbf{l}_n}{l_m^2 l_n^2}\left(3\frac{l_n r_{mi}}{l_m^2}\frac{\partial l_m}{\partial \mathbf{F}^{\mathrm{T}}}+3\frac{l_m r_{ni}}{l_n^2}\frac{\partial l_n}{\partial \mathbf{F}^{\mathrm{T}}}+\frac{r_{ni}}{l_n}\frac{\partial l_m}{\partial \mathbf{F}^{\mathrm{T}}}+\frac{r_{mi}}{l_m}\frac{\partial l_n}{\partial \mathbf{F}^{\mathrm{T}}}\right.\\ &\left.-\frac{l_n}{l_m}\frac{\partial r_{mi}}{\partial \mathbf{F}^{\mathrm{T}}}-\frac{l_m}{l_n}\frac{\partial r_{ni}}{\partial \mathbf{F}^{\mathrm{T}}}\right)\end{aligned} \tag{3.60}$$

and

$$\begin{aligned}\frac{\partial}{\partial \mathbf{F}^{\mathrm{T}}}\left(\frac{\partial^2 \cos\theta_k}{\partial\left(x_0^i\right)^2}\right) &= -\frac{2}{l_m^2 l_n^2}\left(l_m\frac{\partial l_n}{\partial \mathbf{F}^{\mathrm{T}}}+l_n\frac{\partial l_m}{\partial \mathbf{F}^{\mathrm{T}}}\right)\\ &-\frac{2\left(r_{mi}+r_{ni}\right)}{l_m^3 l_n^3}\left(l_m^2\frac{\partial r_{ni}}{\partial \mathbf{F}^{\mathrm{T}}}+l_n^2\frac{\partial r_{mi}}{\partial \mathbf{F}^{\mathrm{T}}}+2l_m r_{ni}\frac{\partial l_m}{\partial \mathbf{F}^{\mathrm{T}}}+2l_n r_{mi}\frac{\partial l_n}{\partial \mathbf{F}^{\mathrm{T}}}\right)\\ &-2\left(l_m^2 r_{ni}+l_n^2 r_{mi}\right)\frac{\partial}{\partial \mathbf{F}^{\mathrm{T}}}\left(\frac{r_{mi}+r_{ni}}{l_m^3 l_n^3}\right)+\left(\frac{3l_n r_{mi}^2}{l_m^3}+\frac{3l_m r_{ni}^2}{l_n^3}+\frac{2r_{mi}r_{ni}}{l_m l_n}\right.\\ &\left.-\frac{l_m}{l_n}-\frac{l_n}{l_m}\right)\frac{\partial}{\partial \mathbf{F}^{\mathrm{T}}}\left(\frac{\mathbf{l}_m\square\mathbf{l}_n}{l_m^2 l_n^2}\right)+\frac{\mathbf{l}_m\square\mathbf{l}_n}{l_m^2 l_n^2}\left[3\frac{\partial}{\partial \mathbf{F}^{\mathrm{T}}}\left(\frac{l_n r_{mi}^2}{l_m^3}\right)+3\frac{\partial}{\partial \mathbf{F}^{\mathrm{T}}}\left(\frac{l_m r_{ni}^2}{l_n^3}\right)\right.\\ &\left.+2\frac{\partial}{\partial \mathbf{F}^{\mathrm{T}}}\left(\frac{r_{mi}r_{ni}}{l_m l_n}\right)-\frac{\partial}{\partial \mathbf{F}^{\mathrm{T}}}\left(\frac{l_m}{l_n}\right)-\frac{\partial}{\partial \mathbf{F}^{\mathrm{T}}}\left(\frac{l_n}{l_m}\right)\right]\end{aligned} \tag{3.61}$$

where

$$\frac{\partial}{\partial \mathbf{F}^{\mathrm{T}}}\left(\frac{r_{mi}+r_{ni}}{l_m^3 l_n^3}\right)=\frac{1}{l_m^3 l_n^3}\left(\frac{\partial r_{mi}}{\partial \mathbf{F}^{\mathrm{T}}}+\frac{\partial r_{ni}}{\partial \mathbf{F}^{\mathrm{T}}}\right)-\frac{3\left(r_{mi}+r_{ni}\right)}{l_m^4 l_n^4}\left(l_m\frac{\partial l_n}{\partial \mathbf{F}^{\mathrm{T}}}+l_n\frac{\partial l_m}{\partial \mathbf{F}^{\mathrm{T}}}\right) \tag{3.62}$$

$$\begin{aligned}\frac{\partial}{\partial \mathbf{F}^{\mathrm{T}}}\left(\frac{\mathbf{l}_m\square\mathbf{l}_n}{l_m^2 l_n^2}\right) &= \frac{1}{l_m^2 l_n^2}\left(r_{m1}\frac{\partial r_{n1}}{\partial \mathbf{F}^{\mathrm{T}}}+r_{n1}\frac{\partial r_{m1}}{\partial \mathbf{F}^{\mathrm{T}}}+r_{m2}\frac{\partial r_{n2}}{\partial \mathbf{F}^{\mathrm{T}}}+r_{n2}\frac{\partial r_{m2}}{\partial \mathbf{F}^{\mathrm{T}}}\right)\\ &-\frac{2\mathbf{l}_m\square\mathbf{l}_n}{l_m^3 l_n^3}\left(l_m\frac{\partial l_n}{\partial \mathbf{F}^{\mathrm{T}}}+l_n\frac{\partial l_m}{\partial \mathbf{F}^{\mathrm{T}}}\right)\end{aligned} \tag{3.63}$$

$$\frac{\partial}{\partial \mathbf{F}^{\mathrm{T}}}\left(\frac{l_n r_{mi}^2}{l_m^3}\right)=\frac{r_{mi}^2}{l_m^3}\frac{\partial l_n}{\partial \mathbf{F}^{\mathrm{T}}}+\frac{2l_n r_{mi}}{l_m^3}\frac{\partial r_{mi}}{\partial \mathbf{F}^{\mathrm{T}}}-\frac{3l_n r_{mi}^2}{l_m^4}\frac{\partial l_m}{\partial \mathbf{F}^{\mathrm{T}}} \tag{3.64}$$

$$\frac{\partial}{\partial \mathbf{F}^{\mathrm{T}}}\left(\frac{r_{mi}r_{ni}}{l_m l_n}\right)=\frac{1}{l_m l_n}\left(r_{mi}\frac{\partial r_{ni}}{\partial \mathbf{F}^{\mathrm{T}}}+r_{ni}\frac{\partial r_{mi}}{\partial \mathbf{F}^{\mathrm{T}}}\right)-\frac{r_{mi}r_{ni}}{l_m^2 l_n^2}\left(l_m\frac{\partial l_n}{\partial \mathbf{F}^{\mathrm{T}}}+l_n\frac{\partial l_m}{\partial \mathbf{F}^{\mathrm{T}}}\right) \tag{3.65}$$

and

$$\frac{\partial}{\partial \mathbf{F}^{\mathrm{T}}}\left(\frac{l_m}{l_n}\right)=\frac{1}{l_n}\frac{\partial l_m}{\partial \mathbf{F}^{\mathrm{T}}}-\frac{l_m}{l_n^2}\frac{\partial l_n}{\partial \mathbf{F}^{\mathrm{T}}} \tag{3.66}$$

In the numerical example, a graphene sheet of 800 atoms is considered to be subject to a deformation gradient of $\mathbf{F}=\begin{bmatrix}1.02 & -0.01\\ 0.0 & 1.00\end{bmatrix}$. In our calculation, the parameters are:

$$l_0=1.42\times10^{-10}\,\mathrm{m},\ \theta_0=2.094\mathrm{rad},$$

$$D_e=6.03105\times10^{-19}\,\mathrm{Nm},\ \beta=2.625\times10^{10}/\mathrm{m},$$

$$k_\theta=1.13\times10^{-18}\,\mathrm{Nm/rad^2},\ k_s=0.754/\mathrm{rad^4}$$

The calculated normal Cauchy stresses from molecular dynamics and the continuum approximation with either the conventional CB rule or the TCB rule are compared in Fig. 3.8. We can also conclude that the continuum-level Cauchy stresses based on the continuum approximation with the TCB rule are in good agreement with those from molecular dynamics at various temperatures.

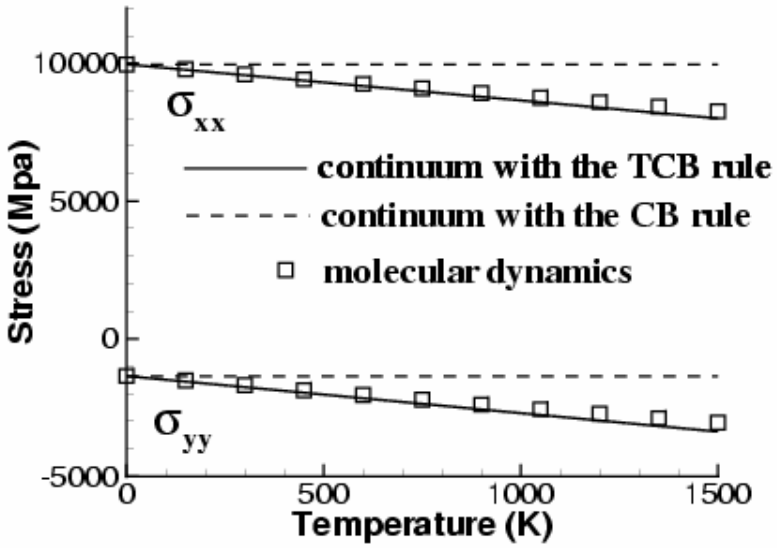

Figure 3.8: Normal Cauchy stresses of a graphene sheet subject to a deformation gradient

3.3.4 Three-dimensional Simple Cubic Lattice

From Fig 3.8, we can know that in the unit cell of a three-dimensional simple cubic lattice, there is only one atom and 6 half-bonds. So, for each atom, there are 3 independent bonds. Those three bonds are

$$\mathbf{l}_1 = \begin{Bmatrix} r_{11} \\ r_{12} \\ r_{13} \end{Bmatrix} l_0 = \begin{Bmatrix} F_{11} \\ F_{21} \\ F_{31} \end{Bmatrix} l_0 \tag{3.67}$$

$$\mathbf{l}_2 = \begin{Bmatrix} r_{21} \\ r_{22} \\ r_{23} \end{Bmatrix} l_0 = \begin{Bmatrix} F_{12} \\ F_{22} \\ F_{32} \end{Bmatrix} l_0 \tag{3.68}$$

$$\mathbf{l}_3 = \begin{Bmatrix} r_{31} \\ r_{32} \\ r_{33} \end{Bmatrix} l_0 = \begin{Bmatrix} F_{13} \\ F_{23} \\ F_{33} \end{Bmatrix} l_0 \tag{3.69}$$

And the volume of the unit cell is $V_0 = l_0^3$. In this case we do not consider the effects from angle-bending potential.

A three-dimensional simple cubic lattice with each dimension of 5nm is studied in this example. Fig. 3.8 shows the basic geometry of this cubic lattice and its unit cell. We still employ the Lennard-Jones 6-12 potential and the parameters are the same as in Eq. (3.16).

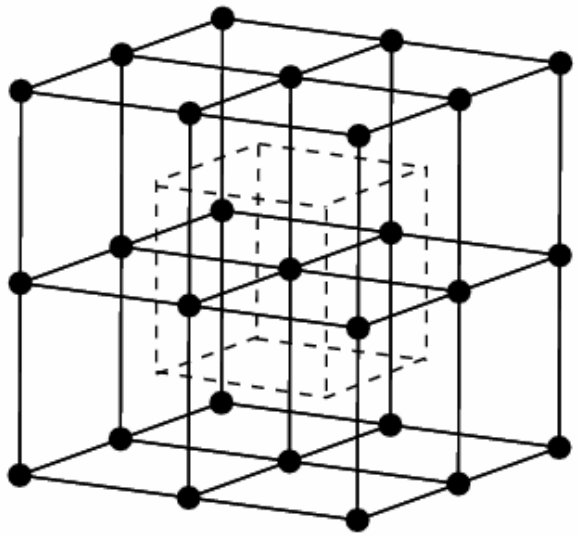

Figure 3.9: Geometry of a cubic lattice and the unit cell

Not to lose generality, we investigate the Cauchy stress evolution as the simulated lattice at various temperatures from 0K to 1500K and subject to the following deformation gradient,

$$\mathbf{F} = \begin{bmatrix} 1.01 & 0.05 & 0.03 \\ 0.0 & 1.02 & 0.04 \\ 0.0 & 0.0 & 1.03 \end{bmatrix} \tag{3.70}$$

Since there are no temperature effects on shear stresses, we only compare the normal Cauchy stresses from molecular dynamics simulation and those from the continuum approximation with either the CB rule or the TCB rule as shown in Tab. 3.1. With the consideration of temperature effects, the results from the continuum approximation with the TCB technique match the molecular dynamics solutions better than those from the continuum approximation with the CB rule.

Temperature (K)		**0**	**300**	**600**	**900**	**1200**	**1500**
σ_{xx} (Mpa)	CB	5128.15	5128.15	5128.15	5128.15	5128.15	5128.15
	TCB	5128.15	5092.47	5056.80	5021.12	4985.44	4949.77
	MD	5128.15	5083.55	5055.32	5043.26	5023.87	4998.69
σ_{yy} (Mpa)	CB	9734.92	9734.92	9734.92	9734.92	9734.92	9734.92
	TCB	9734.92	9695.06	9655.21	9615.35	9575.49	9535.63
	MD	9734.92	9703.53	9668.00	9632.53	9597.25	9569.72
σ_{zz} (Mpa)	CB	13035.51	13035.51	13035.51	13035.51	13035.51	13035.51
	TCB	13035.51	12991.61	12947.70	12903.80	12859.89	12815.99
	MD	13035.51	13007.78	12978.02	12936.49	12900.09	12860.72

Table 3.1: Normal Cauchy stress components at various temperatures for a three-dimensional simple cubic lattice subject to the deformation gradient in Eq. (3.70)

3.4 Summary and Conclusions

The temperature-related Cauchy-Born rule is developed as a new temperature-dependent homogenization technique for multiscale modeling. With the consideration of

the free energy instead of the potential energy, the TCB rule assumes that atoms have locally harmonic motion in addition to homogeneous assumption. When employing the TCB rule in the nanoscale continuum approximation, the nominal stress can be explicitly computed as the first derivative of the Helmholtz free energy density to the transpose of the deformation gradient. Since the Helmholtz free energy is temperature-dependent, multiscale methods consisting of the TCB rule embedded continuum model can be used to elucidate temperature-related physical phenomena at the nanoscale. Stress analyses of canonical ensembles verify the continuum approximation with the TCB rule by comparing the calculated Cauchy stresses with the outcomes of molecular dynamics simulations.

CHAPTER 4

NANOSCALE MESHFREE PARTICLE METHODS

4.1 Implementation of the Homogenization Technique

4.1.1 Implementation of the CB Rule

With a homogenization technique, such as the CB rule, it is possible to impose the continuum mechanics methods to perform simulations at the nanoscale because the intrinsic properties of material can be sought at the atomic level and embedded in the continuum. Such methods are also called the hierarchical multiscale methods, or quasicontinuum method. Finite element methods are always used in multiscale methods with the implementation of the CB rule. Since the meshfree particle methods are advantageous to treat large deformation problems as well as fracture problems, they will have potential to be used in nanoscale numerical modeling and simulation. The CB rule states the deformation is locally homogeneous, so it is assumed there is a constant gradient of deformation in each volume that is associated with a master particle or a stress point.

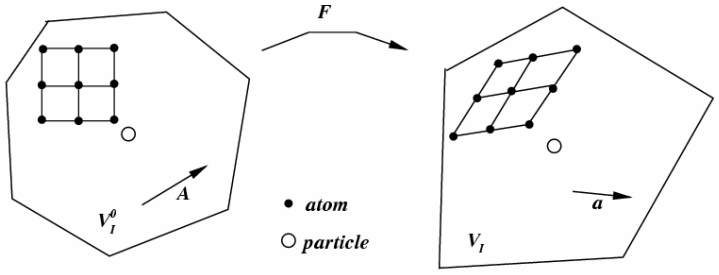

Figure 4.1: Quasicontinuum method

As the illustration in Fig. 4.1, an undeformed lattice vector **A** in the reference configuration is mapped into **a** in the current configuration by the gradient of deformation **F** via $\mathbf{a} = \mathbf{F}\mathbf{A}$. In the continuum model, the potential energy depends on the elongations and angle changes of the atomic bonds that underlie the volume of the master particles or stress points. Then, the nominal stresses, **P**, are computed as follows (should F be transposed?)

$$\mathbf{P}\left(\mathbf{X}_I^M\right) = \frac{\partial w_C\left(\mathbf{F}\left(\mathbf{X}_I^M\right)\right)}{\partial \mathbf{F}^{\mathrm{T}}\left(\mathbf{X}_I^M\right)}, \quad \mathbf{P}\left(\mathbf{X}_I^S\right) = \frac{\partial w_C\left(\mathbf{F}\left(\mathbf{X}_I^S\right)\right)}{\partial \mathbf{F}^{\mathrm{T}}\left(\mathbf{X}_I^S\right)} \tag{4.1}$$

where w_C is the potential energy density, and

$$\mathbf{F}\left(\mathbf{X}_I^M\right) = \sum_J \frac{\partial \omega_J\left(\mathbf{X}_I^M\right)}{\partial \mathbf{X}} \mathbf{u}_J^M, \quad \mathbf{F}\left(\mathbf{X}_I^S\right) = \sum_J \frac{\partial \omega_J\left(\mathbf{X}_I^S\right)}{\partial \mathbf{X}} \mathbf{u}_J^M \tag{4.2}$$

are the deformation gradients at the master particle or stress point I. Eq. (4.1) serves as the constitutive equation for the meshfree particle methods based on atomistic potentials via the CB rule.

4.1.2 Implementation of the TCB Rule

When using meshfree particle methods for nanoscale simulation, the TCB rule results in a constitutive relationship due to molecular properties. As an instance, we consider a Voronoi cell CI associated with a particle PI. PI can be any master particle or stress points in the simulated domain. During the implementation of the TCB rule in meshfree particle methods, the following assumption and procedures are conducted:

- The lattice in cell CI is assumed to be subject to a deformation gradient as that of particle PI. Therefore, the strain energy density at zero temperature can be calculated via a unit cell.

- All the atoms in cell CI are assumed to have the identical harmonic vibration mode. Then, a dynamical matrix can be calculated via the unit cell for all the atoms in this cell.
- The molecular domain in cell CI is assumed to be at a constant temperature as that of particle PI. The free energy density is thereafter computed via Eq. (3.13), and both master particles and stress points are quadrature points in meshfree particle methods.
- Once free energy density is calculated, stresses of particles can be obtained through Eq. (3.14). Numerical integration will be performed to compute nodal forces using Eq. (2.18) and Eq. (2.19), and discrete equations, Eq. (2.17), will be thereafter solved.
- Consequently, the nominal stresses, $\mathbf{P}$, at master particles or stress points are computed as the follows

$$\mathbf{P}\left(\mathbf{X}_I^M, T\right) = \frac{\partial w_H\left(\mathbf{F}\left(\mathbf{X}_I^M\right), T\right)}{\partial \mathbf{F}^{\mathrm{T}}\left(\mathbf{X}_I^M\right)}, \quad \mathbf{P}\left(\mathbf{X}_I^S, T\right) = \frac{\partial w_H\left(\mathbf{F}\left(\mathbf{X}_I^S\right), T\right)}{\partial \mathbf{F}^{\mathrm{T}}\left(\mathbf{X}_I^S\right)} \tag{4.3}$$

4.2 Modeling of Fracture at Nanoscale

Meshfree particle methods have advantages in dealing with large deformation problems, and problems with moving discontinuities such as fracture mechanics. Such advantages will benefit the developed hierarchical multiscale method in which a meshfree particle method is employed as well as the TCB rule. In this thesis, we introduce visibility criterion and cohesive zone model in meshfree particle methods to model cracks at the nanoscale.

4.2.1 Visibility Criterion in Meshfree Particle Methods

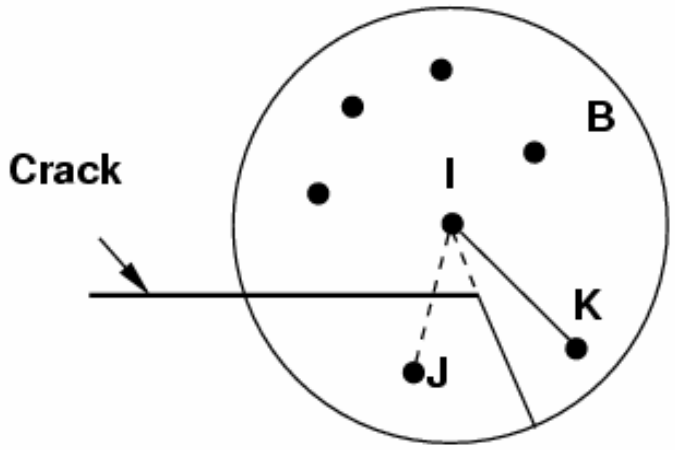

Figure 4.2: Visibility criterion in meshfree particle methods

A crack is modeled in meshfree particle method by defining a line segment internal to the domain as shown in Fig. 4.2. The domains of influence for particles near the crack are truncated whenever they intersect the crack surface so that a particle on one side of the crack will not affect particles on the opposite side of the crack. This technique was called the visibility criterion by Krysl and Belytschko [6]. The domain of influence can be considered as the line of sight and the crack can be considered as an opaque boundary. Whenever the line of sight meets the opaque boundary, the domain of influence is cut. In Fig. 4.2, if we search the neighbor particles for the particle I, the particle K is included but not the particle J, since the latter is not visible for the particle I due to the block of the crack. Other techniques, the diffraction method and the

transparency method [57], can provide continuous and smooth approximations near nonconvex boundaries. For simplification, we use the visibility criterion in this thesis.

4.2.2 Cohesive Zone Model

The crack propagation criterion used in our study is similar to the cohesive zone model [58]. As shown in Fig. 4.3, two crack tips should be monitored in the cohesive zone model: one is called physical tip which is a "real" crack tip in physics, and the other is mathematical tip which means it is a fictitious tip ahead of the physical one. The physical meanings of those two tips at the nanoscale are described as follows. It is known that crack propagation involves bond breakage so that the physical tip moves to the location where bonds are broken. Such a tip can be viewed as a "real" crack tip at the macroscale. On the other hand, the mathematical tip moves to the location where bonds become unstable. An unstable bond means that the interatomic bond force decreases while the bond length increases. Between the mathematical tip and the physical tip, there is a so-called cohesive zone, where the cohesive traction is applied on the two facets of the cohesive zone. It should be noted here that the mathematical tip is used to determine the domain of influence in meshfree particle methods via the visibility criterion.

The cohesive traction, $\boldsymbol{\tau}$, are taken as external forces in meshfree particle simulation and they are derived as

$$\boldsymbol{\tau} = \frac{\partial \hat{w}_H \left(\boldsymbol{\Delta}, T \right)}{\partial \boldsymbol{\Delta}} \tag{4.4}$$

where $\boldsymbol{\Delta}$ is the crack opening displacement vector. $\hat{w}_H \left(\boldsymbol{\Delta}, T \right)$ is the free energy per unit length along the cohesive zone and can be calculated via the TCB rule.

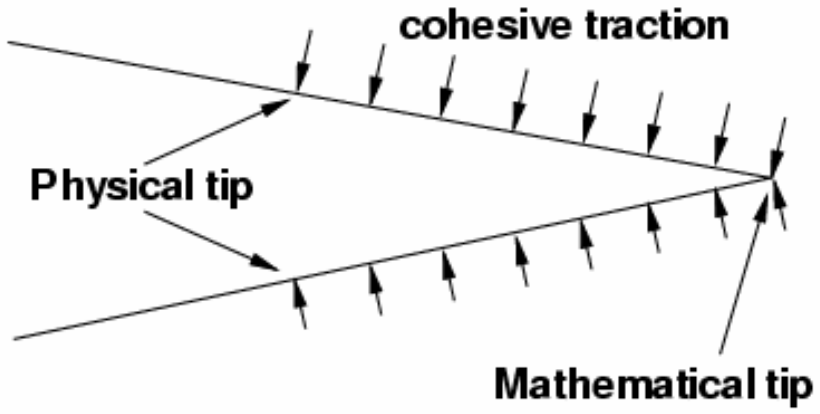

Figure 4.3: Cohesive zone model for crack propagation

In meshfree particle methods, the cohesive tractions can be projected into consistent nodal forces [58] without introducing additional degree of freedom. In order to represent the surface geometry and calculate the cohesive traction, a parameterization must be implemented. As shown in Fig. 4.4, we define a local coordinate system in the reference configuration as well as the finite element points along the cohesive zone. The crack opening displacement vector $\mathbf{\Delta}$ may be written as

$$\begin{aligned}\mathbf{\Delta}(\xi) &= \mathbf{u}^{+}(\xi) - \mathbf{u}^{-}(\xi) \\ &= \sum_{P\in N^{+}} \omega_p(\xi)\mathbf{u}_p - \sum_{P\in N^{-}} \omega_p(\xi)\mathbf{u}_p\end{aligned} \tag{4.5}$$

where ξ are local coordinates; $\mathbf{u}^{+}$ and $\mathbf{u}^{-}$ are displacements of upper and lower facets of the cohesive zone, respectively; ω_p is the meshfree shape function associated with particle p involved in the truncated neighborhood of the FE point, $\mathbf{u}_p$ is the displacement of particle p. In a variational setting, the contribution to the virtual work from cohesive traction is

$$\delta W = \int_{\Gamma_0} \boldsymbol{\tau} \cdot \delta \boldsymbol{\Delta} \tag{4.6}$$

where Γ_0 is the cohesive zone in the reference configuration; and $\delta\boldsymbol{\Delta}$ is the variation in the surface opening displacement. On the other hand, in terms of the variation in the particle displacements, $\mathbf{u}_p$, the work increment due to the crack opening can be written as

$$\delta W = \sum \mathbf{f}_p \cdot \delta \mathbf{u}_p \tag{4.7}$$

where $\mathbf{f}_p$ is the particle force projected from the cohesive traction $\boldsymbol{\tau}$. Therefore, the nodal force due to the cohesive traction is computed as

$$f_{pi} = \int_{\Gamma_0} \sum_j \frac{\partial \Delta_j}{\partial u_{pi}} \tau_j d\Gamma \tag{4.8}$$

where

$$\frac{\partial \Delta_j}{\partial u_{pi}} = \begin{cases} \omega_p \delta_{ij} & \text{for} \quad p \in N^+ \\ -\omega_p \delta_{ij} & \quad\quad p \in N^- \end{cases} \tag{4.9}$$

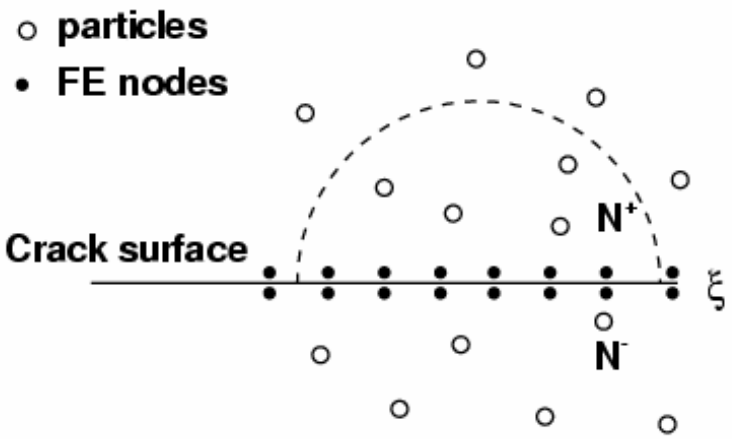

Figure 4.4: Projection of cohesive traction

4.3 Applications

4.3.1 One-dimensional Molecule Chain

4.3.1.1 Continuum Model of Molecule Chain

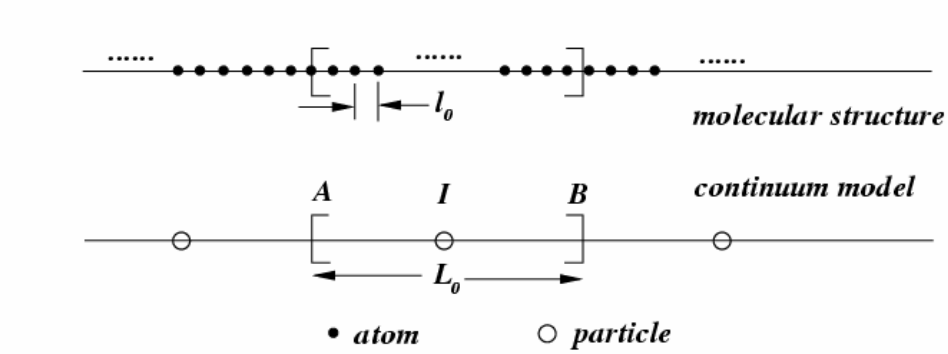

Figure 4.5: A continuum model for a molecular chain with the meshfree particle methods

A line of atoms as well as its continuum model in the reference (initial) configuration is considered here as shown in Fig. 4.5. The equilibrium bond length between neighboring atoms is l_0, and the length of the region AB associated with the particle I is L_0. We assume that only the nearest two atoms are attractive and repulsive with each other. Therefore, the molecular potential can be written as follows without considerations of external forces:

$$W = \sum_{i=2}^{N} \varphi\left(x_i - x_{i-1}\right) = \sum_{i=1}^{N-1} \varphi\left(l_i\right) \tag{4.10}$$

where N is the total number of atoms; $l_i = x_{i+1} - x_i$ is the current bond length. If we use F_I to denote the deformation gradient at particle I, all the deformed bonds in region AB

will have the same length, $l = F_I l_0$, according to the assumption of the CB rule. One can write the potential density of the volume associated with particle I based on the atomic level potential as

$$w_C\left(F_I\right) = \frac{W_C\left(F_I\right)}{L_0} = \frac{\frac{L_0}{l_0}\varphi(l)}{L_0} = \frac{\varphi(l)}{l_0} = \frac{\varphi\left(F_I l_0\right)}{l_0} \tag{4.11}$$

Then, the nominal stress can be calculated as

$$P\left(X_I\right) = \frac{\partial w_C\left(F_I\right)}{\partial F_I} = \frac{1}{l_0}\frac{\partial \varphi\left(F_I l_0\right)}{\partial F_I} \tag{4.12}$$

As an instance, we use the Lennard-Jones (LJ) 6-12 potential to approach the interaction between the nearest atoms. The LJ 6-12 potential function is written as

$$\varphi = 4\varepsilon\left[\left(\frac{\sigma}{l}\right)^{12} - \left(\frac{\sigma}{l}\right)^{6}\right] \tag{4.13}$$

where ε and σ are constants chosen to fit material properties and l is the distance between two atoms. ε is the depth of the potential energy well. σ is the value of l where the potential becomes zero and $\sigma = 2^{-1/6} l_0$. The potential energy density at particle I can be written as follows from Eq. (4.11):

$$w_C\left(F_I\right) = \frac{\varphi\left(F_I l_0\right)}{l_0} = \frac{4\varepsilon}{l_0}\left[\left(\frac{\sigma}{l_0}\right)^{12} F_I^{-12} - \left(\frac{\sigma}{l_0}\right)^{6} F_I^{-6}\right] \tag{4.14}$$

Therefore, the nominal stress at particle I can be obtained as

$$P\left(X_I\right) = \frac{\partial w_C}{\partial F_I} = \frac{4\varepsilon}{l_0}\left[\frac{6\sigma^6}{l_0^6 F_I^7} - \frac{12\sigma^{12}}{l_0^{12} F_I^{13}}\right] \tag{4.15}$$

Wave propagation along a one-dimensional molecule chain is studied by using molecular dynamics and the meshfree particle methods with quasicontinuum

implementation separately. The molecule chain contains 2001 atoms. 101 particles are used in the meshfree particle simulation. The L-J (6-12) potential function is used to approach the interaction between the nearest atoms. The constants are chosen as: $\sigma = 3.4\times10^{-10}\,\mathrm{m}$ and $\varepsilon = 1.65\times10^{-21}\,\mathrm{J}$. The mass of each atom is set to be $3.8\times10^{-10}\,\mathrm{kg}$. In the meshfree particle methods, the nominal stress can be obtained from Eq. (4.15). Fig. 4.6 shows the comparison of the calculated wave configurations at $t = 0.02\mathrm{ns}$, from the molecular dynamics simulation and the meshfree particle methods, when an initial cosine shaped wave is given. We can see that they are in accord.

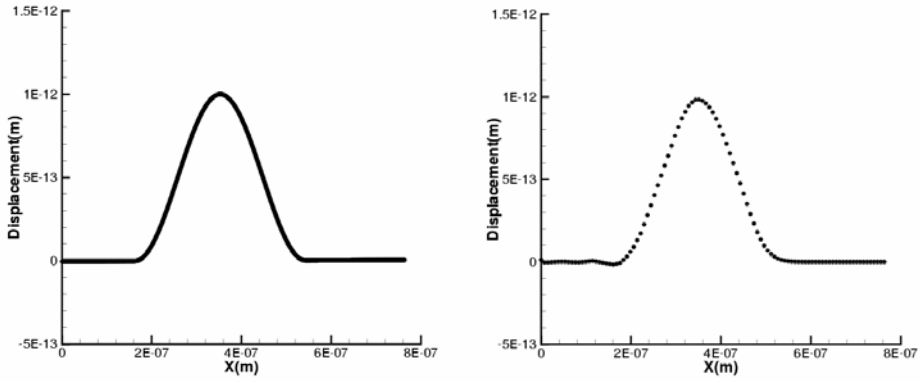

(a) molecular dynamics (b) meshfree particle method

Figure 4.6: Wave propagation in a molecule chain

4.3.1.2 Overlapping of Continuum and Discrete Model of Molecule Chain

With the development of multiscale modeling at the nanoscale, Xiao and Belytschko [20] proposed a bridging domain coupling method. In this thesis, this technique is used to develop a concurrent multiscale model in which the meshfree

particle method is coupled with molecular dynamics. In expressing the total Hamiltonian of the system, a scaling parameter β in the bridging domain, Ω_0^{int}, which is the overlapping domain between the molecular domain, Ω_0^M, and the continuum domain, Ω_0^C, as shown in Fig. 4.7, is employed. The Hamiltonian, H, for the complete domain is taken to be a linear combination of the molecular and continuum Hamiltonians, as shown in

$$\begin{aligned} H = \beta H^M + (1-\beta) H^C = \sum_I \beta(\mathbf{X}_I) \frac{1}{2} m_I \dot{\mathbf{d}}_I \cdot \dot{\mathbf{d}}_I + \sum_I \beta(\mathbf{X}_I) W_M(\mathbf{X}_I) \\ + \sum_I (1-\beta(\mathbf{X}_I)) \frac{1}{2} M_I \dot{\mathbf{u}}_I \cdot \dot{\mathbf{u}}_I + \int_{\Omega_0} (1-\beta(\mathbf{X})) w_C(\mathbf{F}(\mathbf{X})) d\Omega \end{aligned} \tag{4.16}$$

where m_I and M_I are mass for atoms and master particles, respectively. W_M is the potential function in the molecular model. H^M and H^C are molecular and continuum Hamiltonians, respectively. **d** is atomic displacement and **u** is the continuum displacement.

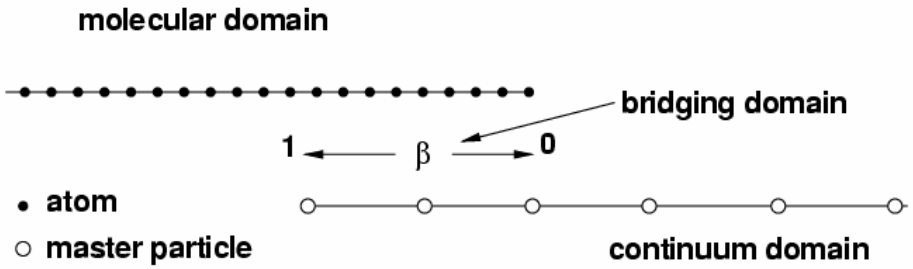

Figure 4.7: A bridging coupling model for a molecular chain

The constraints in the bridging domain are

$$\mathbf{g}_I = \{g_{iI}\} = \{u_i(\mathbf{X}_I) - d_{iI}\} = \left\{\sum_J \omega_J(\mathbf{X}_I) u_{iJ} - d_{iI}\right\} = 0 \tag{4.17}$$

i.e. the atomic displacements, $\mathbf{d}$, are required to conform to the continuum displacements, $\mathbf{u}$, at the positions of the atoms. The continuum displacement field can be obtained from the meshfree particle approximation as Eq. (2.6). The constraints are applied to all components of the displacements. With the Lagrange multiplier method, the total Hamiltonian is written as

$$H_L = H + \boldsymbol{\lambda}^T \mathbf{g} = H + \sum_I \boldsymbol{\lambda}_I^T \mathbf{g}_I \tag{4.18}$$

where $\boldsymbol{\lambda}_I = \{\lambda_{iI}\}$ is a vector of Lagrange multipliers. Note that the Lagrange multipliers are assigned to the discrete positions of atoms in the bridging domain.

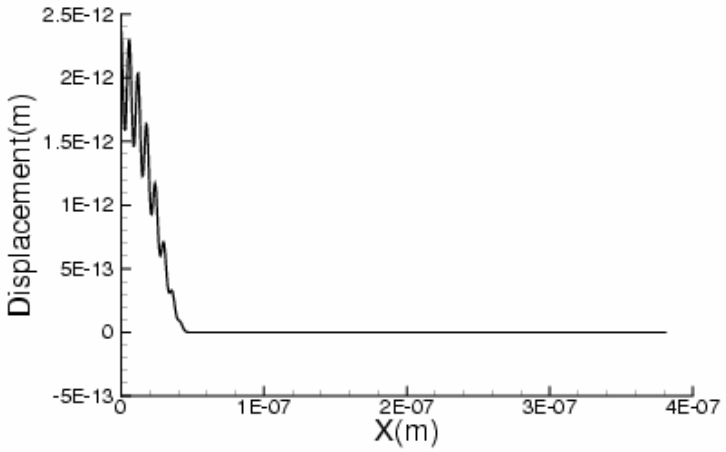

Figure 4.8: The initial wave in a molecule chain

The discrete equations can be derived from Eq. (4.18) via classical Hamiltonian mechanics. In equations of motion there exists constraint forces applied on the atoms/particles in the bridging domain besides external and internal forces. Xiao and

Belytschko [20] developed an explicit time integration algorithm. At first, so-called trial velocities are obtained by solving equations of motion independently in the continuum and molecular domains without the consideration of constraints. Then, constraints are applied to calculate the Lagrange multipliers. Finally, the constraint forces are considered to correct the velocities of atoms/particles in the bridging domain.

In the bridging domain coupling modeling of this molecule chain, there are 1001 atoms in molecular domain and 100 master particles in continuum domain. The initial wave is the combination of high frequency and low frequency waves as shown in Fig. 4.8 in the molecular domain.

A handshake technique [14] was developed for coupling a finite element method and molecular dynamics. In that method, the element size was graded down to the lattice spacing in the handshake region. This technique will result in a non-physical phenomenon as shown in Fig. 4.9(a) at the interface between the continuum domain and the molecular domain if the artificial viscosity is not applied. We can see that high frequency waves are reflected while the low frequency wave passes the continuum domain. Such a phenomenon is also called spurious wave reflection. However, with the bridging domain coupling technique, the spurious wave reflection can be eliminated as shown in Fig. 4.9(b).

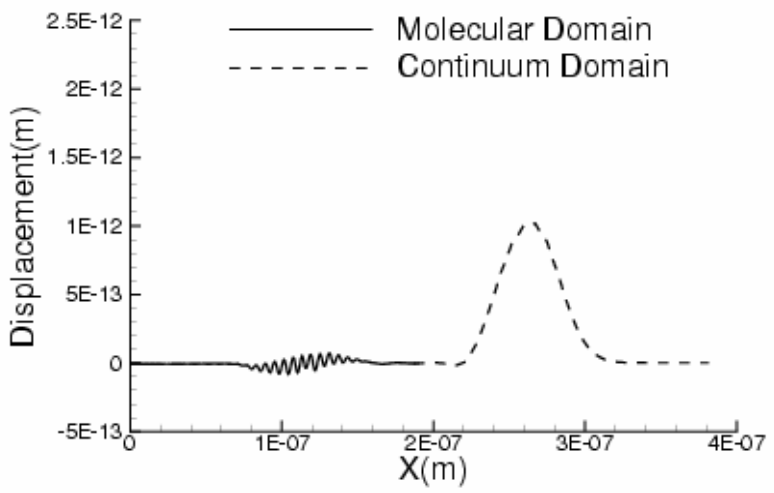

(a) handshake method

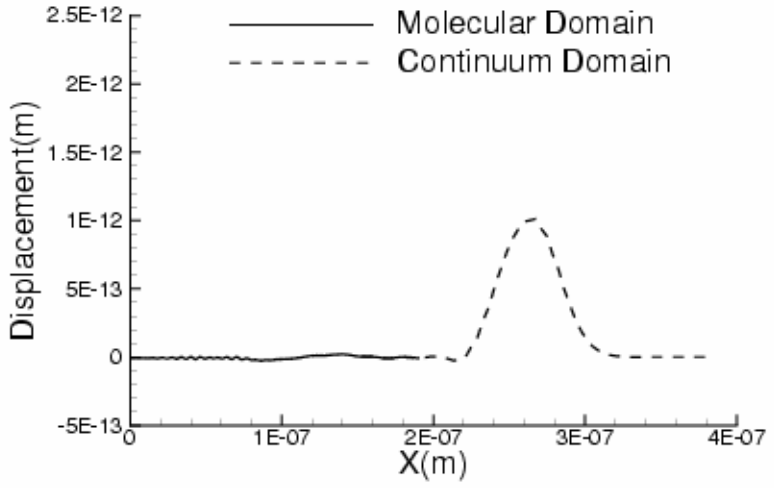

(b) bridging domain coupling method

Figure 4.9: Concurrent multiscale simulation of a molecule chain

4.3.2 Two-dimensional Nanobeam

We consider a 2-D molecular structure with hexagonal-triangular lattices as shown in Fig. 4.10. A pair potential function of $\varphi(l)$ is used here to describe the nearest-neighbor interatomic interaction. l denotes the bond length and $l = l_0$ when the bond is not stretched i.e. when the bond is at the equilibrium state. Fig. 4.10 also shows that a rectangle cell is set as a unit cell to calculate the continuum properties of the molecular structure.

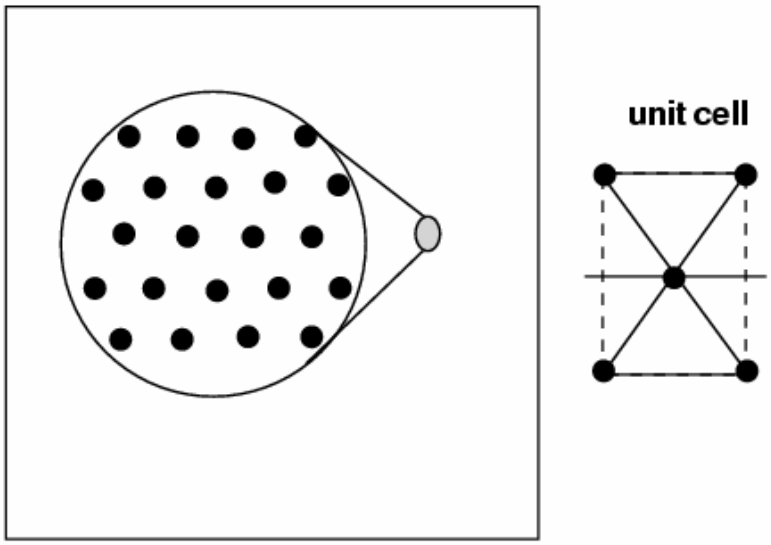

Figure 4.10: A continuum material with hexagonal-triangular molecular structure

We assume that the volume associated with a particle contains a large number of such unit cells. If a unit cell is under the deformation with the deformation gradient $\mathbf{F}$, then there are three types of deformed bonds as shown in Fig. 3.4. Therefore, the strain energy per undeformed unit area (strain energy density) in such a unit cell is

$$w_C = \frac{2}{\sqrt{3}l_0}\left[\varphi(l_1)+\varphi(l_2)+\varphi(l_3)\right] \tag{4.19}$$

where l_1, l_2, l_3 can be described by deformation gradient **F** based on the geometric relations, one can find that

$$\begin{aligned} l_1 &= l_0\sqrt{F_{11}^2+F_{21}^2} \\ l_2 &= l_0\sqrt{(\frac{1}{2}F_{11}-\frac{\sqrt{3}}{2}F_{12})^2+(\frac{1}{2}F_{21}-\frac{\sqrt{3}}{2}F_{22})^2} \\ l_3 &= l_0\sqrt{(\frac{1}{2}F_{11}+\frac{\sqrt{3}}{2}F_{12})^2+(\frac{1}{2}F_{21}+\frac{\sqrt{3}}{2}F_{22})^2} \end{aligned} \tag{4.20}$$

The nominal stress **P** is the first derivative of strain energy density with respect to the transpose of the deformation gradient, and one can have

$$\begin{aligned} \mathbf{P} &= \frac{2}{\sqrt{3}l_0}\left[\frac{\partial\varphi(l_1)}{\partial\mathbf{F}^{\mathrm{T}}}+\frac{\partial\varphi(l_2)}{\partial\mathbf{F}^{\mathrm{T}}}+\frac{\partial\varphi(l_3)}{\partial\mathbf{F}^{\mathrm{T}}}\right] \\ &= \frac{2}{\sqrt{3}l_0}\left[\frac{\partial\varphi(l_1)}{\partial l_1}\frac{\partial l_1}{\partial\mathbf{F}^{\mathrm{T}}}+\frac{\partial\varphi(l_2)}{\partial l_2}\frac{\partial l_2}{\partial\mathbf{F}^{\mathrm{T}}}+\frac{\partial\varphi(l_3)}{\partial l_3}\frac{\partial l_3}{\partial\mathbf{F}^{\mathrm{T}}}\right] \end{aligned} \tag{4.21}$$

and the components of the stress are

$$P_{11} = \frac{2}{\sqrt{3}l_0}\left[\frac{\partial\varphi(l_1)}{\partial l_1}\frac{F_{11}}{l_1}+\frac{\partial\varphi(l_2)}{\partial l_2}\frac{1}{2l_2}\left(\frac{1}{2}F_{11}-\frac{\sqrt{3}}{2}F_{12}\right)+\frac{\partial\varphi(l_3)}{\partial l_3}\frac{1}{2l_3}\left(\frac{1}{2}F_{11}+\frac{\sqrt{3}}{2}F_{12}\right)\right]$$

$$P_{12} = \frac{2}{\sqrt{3}l_0}\left[\frac{\partial\varphi(l_1)}{\partial l_1}\frac{F_{21}}{l_1}+\frac{\partial\varphi(l_2)}{\partial l_2}\frac{1}{2l_2}\left(\frac{1}{2}F_{21}-\frac{\sqrt{3}}{2}F_{22}\right)+\frac{1}{2l_3}\frac{\partial\varphi(l_3)}{\partial l_3}\left(\frac{1}{2}F_{21}+\frac{\sqrt{3}}{2}F_{22}\right)\right]$$

$$P_{21} = \frac{2}{\sqrt{3}l_0}\left[-\frac{\partial\varphi(l_2)}{\partial l_2}\frac{\sqrt{3}}{2l_2}\left(\frac{1}{2}F_{11}-\frac{\sqrt{3}}{2}F_{12}\right)+\frac{\sqrt{3}}{2l_3}\frac{\partial\varphi(l_3)}{\partial l_3}\left(\frac{1}{2}F_{11}+\frac{\sqrt{3}}{2}F_{12}\right)\right]$$

$$P_{22} = \frac{2}{\sqrt{3}l_0}\left[-\frac{\partial\varphi(l_2)}{\partial l_2}\frac{\sqrt{3}}{2l_2}\left(\frac{1}{2}F_{21}-\frac{\sqrt{3}}{2}F_{22}\right)+\frac{\sqrt{3}}{2l_3}\frac{\partial\varphi(l_3)}{\partial l_3}\left(\frac{1}{2}F_{21}+\frac{\sqrt{3}}{2}F_{22}\right)\right]$$

Correspondingly, the first tangential stiffness matrix can be written as

$$\mathbf{C} = \frac{\partial \mathbf{P}}{\partial \mathbf{F}^{\mathrm{T}}} = \frac{\partial^2 w_C}{\partial \mathbf{F}^{\mathrm{T}} \partial \mathbf{F}^{\mathrm{T}}} \tag{4.22}$$

4.3.2.1 Bending of a Nanobeam

In this example, we consider the bending of a nano cantilever beam. The beam contains 5140 atoms as shown in Fig. 4.12 where $L = 270\text{nm}$ and $H = 15.6\text{nm}$. One end of the beam is fixed. A quadratic potential function is used to approximate the interaction between nearest atoms,

$$\varphi(l) = \frac{1}{2} k \left(l - l_0\right)^2 \tag{4.23}$$

where $k = 10000\text{N/m}$ and $l_0 = 1\text{nm}$.

We use the meshfree particle method to simulate the bending of this nanobeam, which is under the load of a prescribed displacement as shown in Fig. 4.11. There are 250 particles used in the simulation. In the meshfree particle method, the nominal stress and tangential stiffness matrix can be calculated when substituting Eq. (4.23) into Eq. (4.21) and Eq. (4.22). During the simulation, the prescribed displacement will be increased by $\Delta d = 3.6\text{nm}$ per calculation step. After 50 steps, the nanobeam will be bent as the final configuration with the shear stress distribution shown in Fig. 4.12(a).

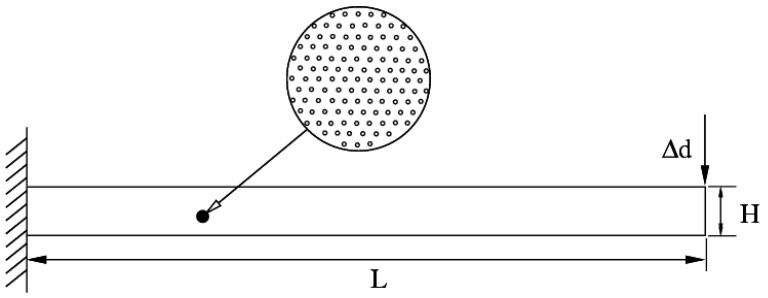

Figure 4.11: A nano cantilever beam

We also show the molecular mechanics calculation result for comparison. One can see that the outcome in Fig. 4.12(b) supports the meshfree particle method result. When different numbers of particles are used in the meshfree particle method simulations, Fig. 4.13 shows the evolution of the calculated nanobeam potential compared with the molecular mechanics result. We can see that the meshfree particle method with 250 particles gives a consistent response with the molecular mechanics calculation. If 1000 or more particles are used in the simulations, the evolution of the nanobeam potential is almost identical to the one from the molecular mechanics calculation.

We study the convergence by using the L_2 error in displacement for the nanoscale meshfree particle method. The error in displacement is defined as

$$Error = \frac{\left\| \mathbf{u}^{MM} - \mathbf{u}^{PM} \right\|_2}{\left\| \mathbf{u}^{MM} \right\|_2} \tag{4.24}$$

where $\mathbf{u}^{MM}$ and $\mathbf{u}^{PM}$ are the atomic displacements from the molecular mechanics calculation and the meshfree particle method, respectively. Note, here, that one can calculate the atomic displacements from the particle displacements in the meshfree particle method based on the meshfree particle approximation. The convergence rate is 1.28 here which is shown in Fig. 4.14.

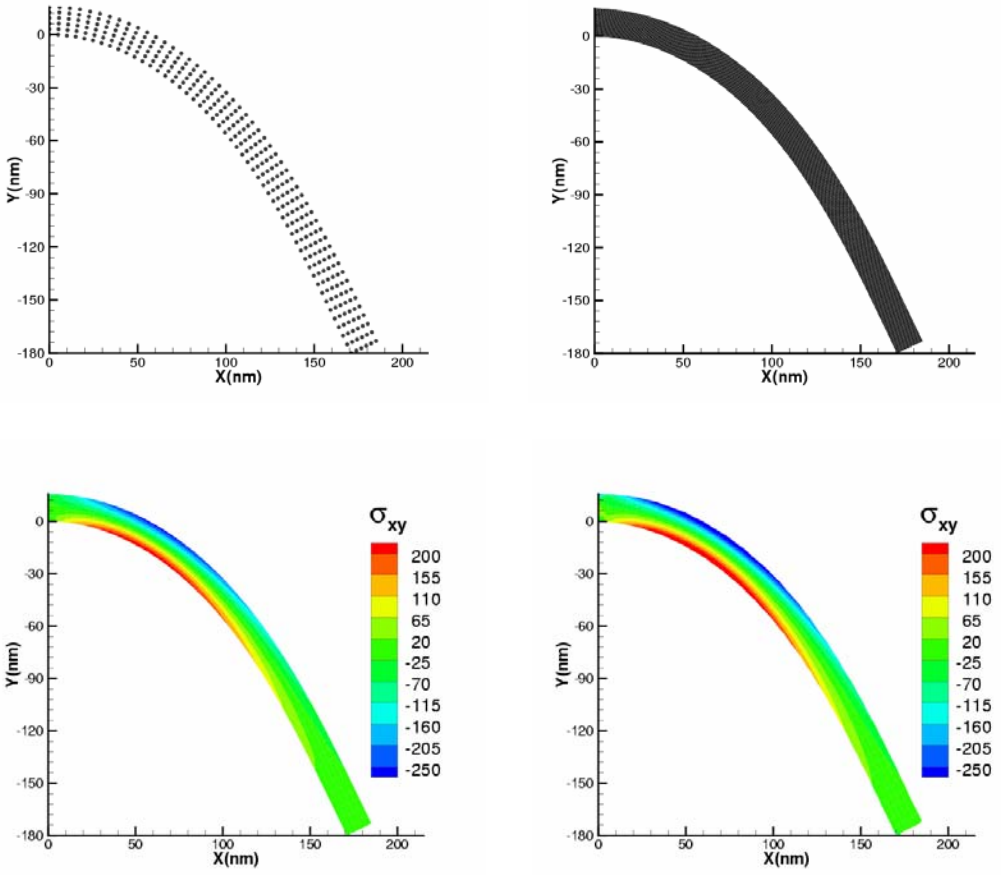

(a) meshfree particle method (b) molecular mechanics

Figure 4.12: Deformed configurations and stress distribution of the nanobeam

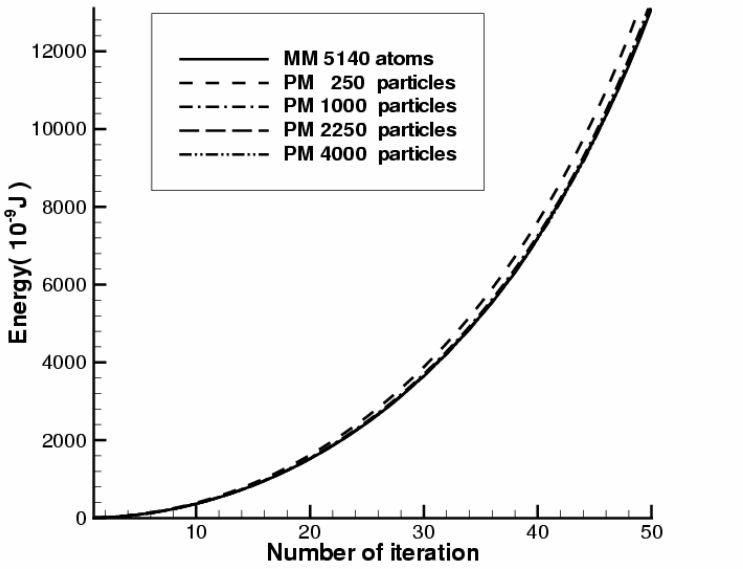

Figure 4.13: Evolutions of the nanobeam potential

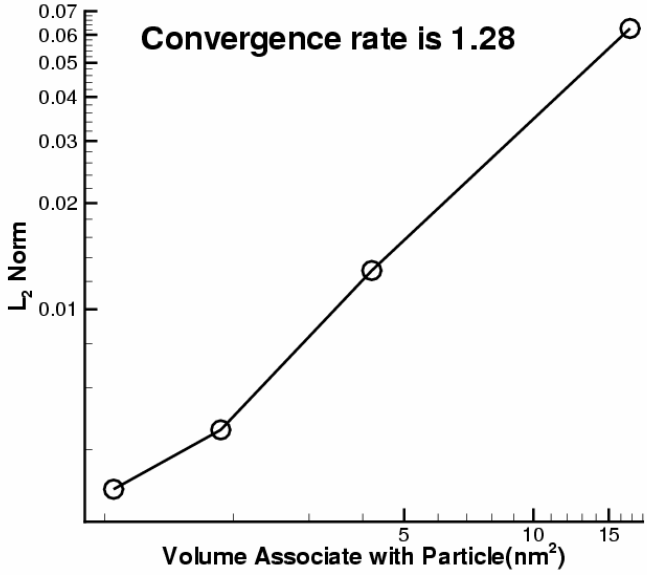

Figure 4.14: Convergence of the nanoscale meshfree particle method

4.3.2.2 Vibration of a Nanobeam

The vibration of a nano cantilever beam is studied in this example. The nanobeam is similar to what we study in the previous examples, but with $L = 200\text{nm}$ and $H = 34.6\text{nm}$. There are 8221 atoms in this nanobeam. One end of the beam is fixed. We use the LJ (6-12) potential function to approximate the interaction between nearest atoms. The constants are chosen as follows: $\sigma = 1.833\text{nm}$ and $\varepsilon = 8.25\times10^{-9}\text{J}$. The mass of each atom is $5.0\times10^{-17}\text{kg}$. In this example, the nanobeam is bent first with the loading of a prescribed displacement at the upper right corner. This step can be achieved similarly with the technique we used in the previous example. Then, if the nanobeam is released, it will vibrate up and down. Different numbers of particles are used in the simulations. The calculated oscillatory amplitude and frequency of the middle point on the right boundary are compared with the molecular dynamics simulation results as shown in Tab. 4.1, as well as computer time, when two vibration circles are finished. We can see that molecular dynamics simulations are obviously computationally intensive and the continuum mechanics (meshfree particle methods here) can save a great amount of computing time. Furthermore, the meshfree particle methods can give very accurate values of the oscillatory amplitudes compared with molecular dynamics, but not the frequencies although they are still compared well. We think that this result is due to the vibration of atoms around their equilibrium positions. Such molecular-level phenomena results in one of the macroscopic properties, temperature.

	Amplitude (nm)	Frequency (1/ns)	CPU time (s)
Molecular dynamics (8221 atoms)	3.90	2.067	425.25
Meshfree particle method (2000 Particles)	3.91	2.159	52.46
Meshfree particle method (320 Particles)	3.93	2.272	11.53
Meshfree particle method (80 Particles)	3.94	2.324	2.31

Table 4.1: Amplitudes and frequencies of nanobeam vibration

4.3.3 A Nanoplate with a Central Crack

4.3.3.1 Stress Distribution

Meshfree particle methods have advantages to treat fracture problems. In this example, we use the meshfree particle method to study the stress concentration of a nanoplate containing an initial central crack. The crack is initialized by taking a number of bonds out in the molecular model. The meshfree particle model with 400 particles is shown in Fig. 4.15. The dimensions are: $L = 270\text{nm}$ and $H = 280\text{nm}$, and the crack length is 135nm. This nanoplate contains 86915 atoms with the triangular molecular structure. The LJ (6-12) potential function is used in this example as the previous one. We use the visibility criterion [30] in the meshfree particle model to construct the kernel functions for the particles near the crack or around the crack tip.

We plan to observe the stress concentration around the crack tip. The constitutive relationship can be achieved through the CB rule as before. For the purpose of

comparison, we also perform molecular mechanics calculations to obtain the contour of stress distribution. At the atomic level, the Cauchy stress can be calculated as Eq. (D.1).

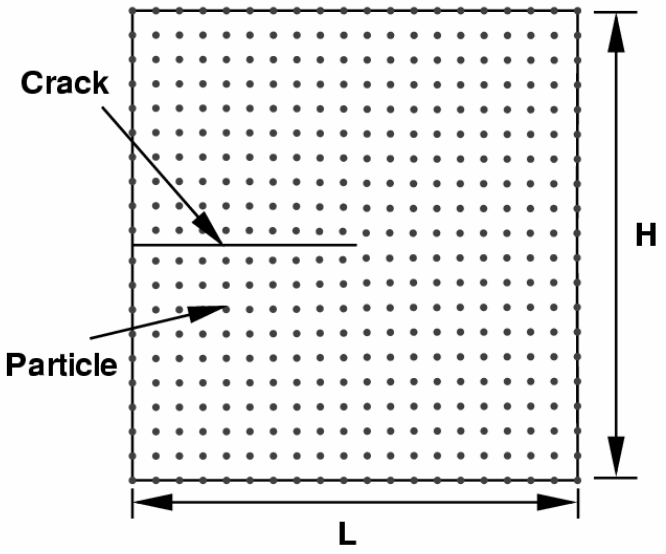

Figure 4.15: A nanoplate with a central crack modeled by the meshfree particle method

Fig. 4.16 shows the comparison of the stress (σ_{yy}) contour from the molecular mechanics calculation and the meshfree particle simulation. In the molecular mechanics calculation, the whole domain is divided into a number of subdomains, for each of which the Cauchy stress can be computed via Eq. (D.1). We can see that the result of meshfree particle method is in accord with that of the molecular mechanics calculation.

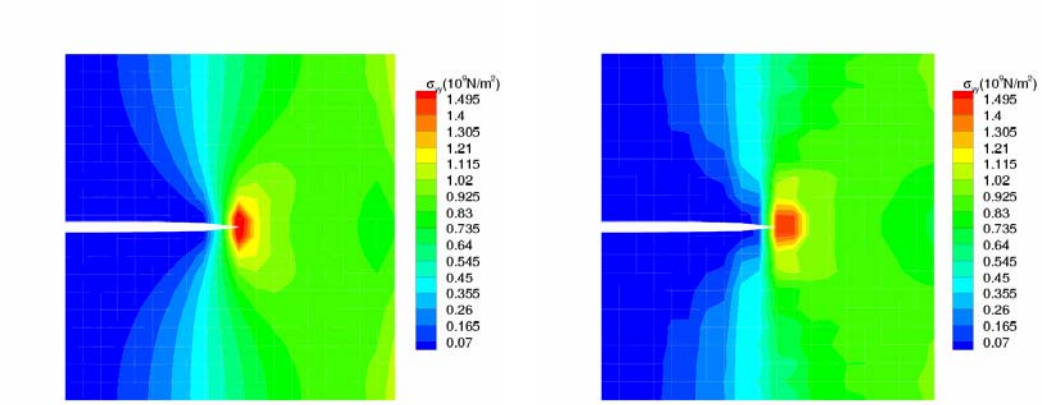

(a) molecular mechanics (b) meshfree particle method

Figure 4.16: Stress concentration in a nanoplate with a central crack

4.3.3.2 Crack Propagation in a Nanoplate for Different Temperature

One of the benefits from the nanoscale meshfree particle method is that it is possible to investigate crack propagation mechanism at the nanoscale using continuum mechanics. With the implementation of the TCB rule, the temperature effects can be investigated. In this example, crack propagation in a nanoplate with the hexagonal-triangular lattice, shown in Fig. 4.17, is studied. We first consider the nanoplate consisting of 256961 atoms with the following dimensions: the length of 800nm and the width of 280nm. Each atom has the mass of 1.0×10^{-22} kg. An edge crack is initiated in the middle of the plate by taking out a number of bonds, and the initial crack length is 20nm. For simplification, the crack is restricted to propagate along the weak interface by assuming that only weakened bonds can be broken. We employ a quadratic potential

function to describe interatomic interactions between nearest neighbouring atoms, except weakened bonds. The quadratic potential function is

$$\varphi(l) = \frac{1}{2} k (l - l_0)^2 \tag{4.25}$$

where the length of undeformed bond is $l_0 = 1.0\text{nm}$, and the spring constant is $k = 594.0\text{N/m}$. A L-J (6-12) potential with a cutoff distance of 2.0nm, as described in Eq. (3.16), is used for weakened bonds. It should be noted here that the tangential stiffness of the weakened bond is equal to the spring constant, k, so that the parameters of the Lennard-Jones potential are: $\varepsilon = 8.25 \times 10^{-18}\text{J}$.

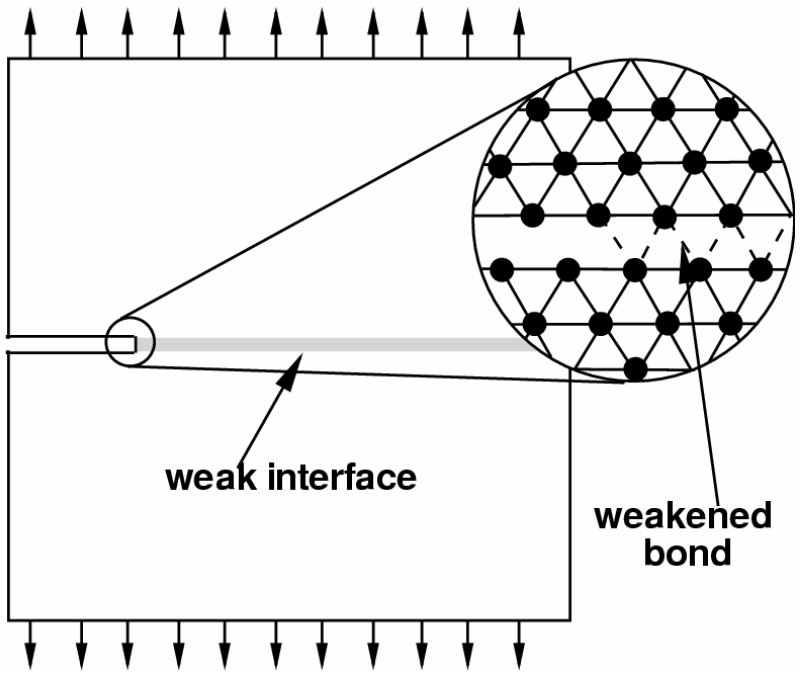

Figure 4.17: A nanoplate with the hexagonal-triangular lattice containing an initial crack

In the meshfree particle model, there are 13600 particles. In this example, the nodal integration scheme is used so that particles are quadrature points. Based on the assumption of the TCB rule, the free energy per length along the cohesive zone is

$$F_H = \varphi(l) + \kappa_B T \ln\left(\frac{\hbar\sqrt{\varphi''(l)}}{\kappa_B T}\right) \tag{4.26}$$

The cohesive traction, $\boldsymbol{\tau}$, is calculated as

$$\tau = \varphi'(l) + \frac{\kappa_B T}{2}\frac{\varphi'''(l)}{\varphi''(l)} \tag{4.27}$$

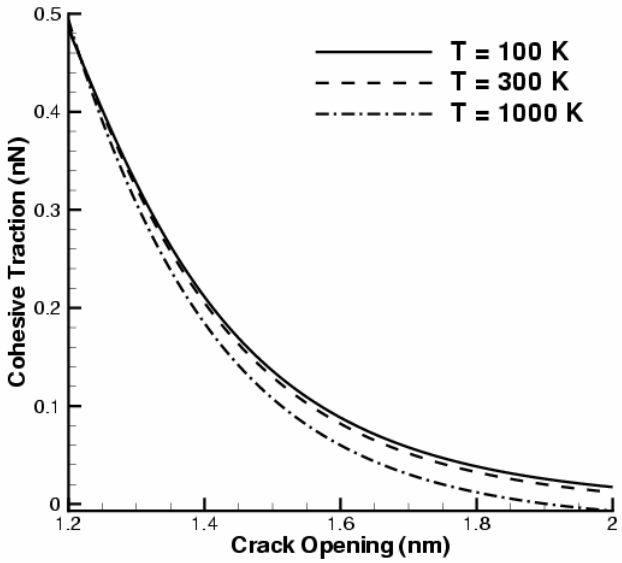

Figure 4.18: The relation of cohesive traction and crack opening along the weak interface

Fig. 4.18 shows the relation of the cohesive traction and the crack opening along the weak interface. We can see that the traction-opening slope gets lower, i.e. the crack can propagate easier, at a higher temperature. On the other hand, the triangular lattice

with the harmonic bonded potential function exhibits a special characteristic in which the Young's modulus is higher at a higher temperature. The moduli are 20GPa, 25GPa, and 36GPa at temperatures of 100K, 300K, and 1000K, respectively. The similar Young's moduli are obtained when performing molecular dynamics simulations at those three temperatures. Consequently, the Rayleigh speed is higher at a higher temperature.

In this example, we investigate temperature effects on the speed of crack propagation. The nanoplate is loaded in mode I via prescribed displacements with the train rate of 1×10^{-8} per fs. Three various temperatures, 100K, 300K and 1000K, are considered. The evolutions of crack speeds are illustrated in Fig. 4.19.

It can be seen that cracks start to propagate around 0.3ns and crack speeds become constants within 0.1ns. The terminal constant crack speeds are 600m/s, 1100m/s and 1350m/s at 100K, 300K and 1000K, respectively. Obviously, high temperature results in high crack propagation speed. It should be noted that all the calculated crack speeds are lower than the Rayleigh wave speed, ~1450m/s. We also consider higher temperatures, such as 2000K. The crack speed does not increase significantly and is still lower than the Rayleigh wave speed. In this example, our simulations demonstrate that the temperature has significant effects on the crack propagation speed when it is lower than 1000K. Otherwise, the temperature effects are not significant. As a comparison, we also perform molecular dynamics simulations, and the Berendsen thermostat is used to maintain the nanoplate at a given temperature. Fig. 4.19 also shows that the same phenomenon can be observed when performing molecular dynamics simulations.

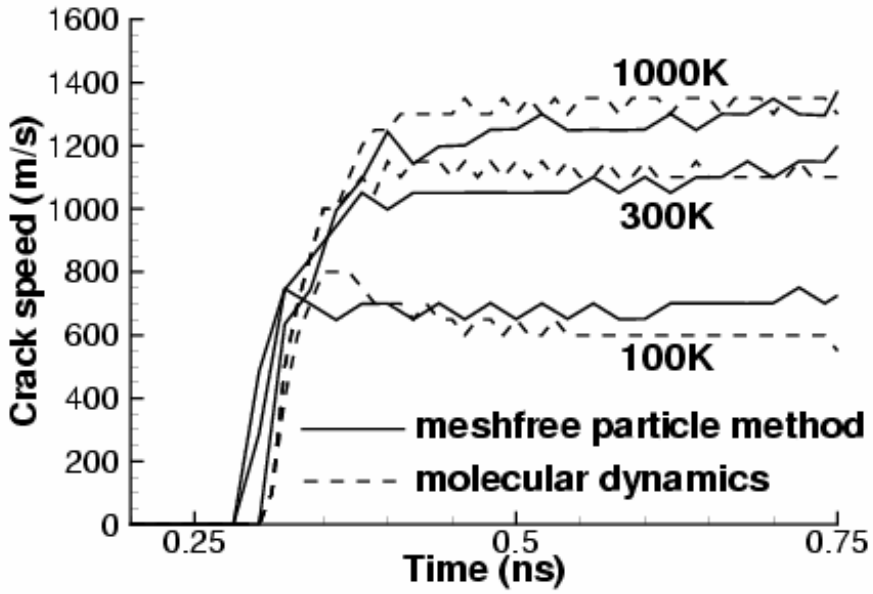

Figure 4.19: Comparison of crack propagation speed at different temperatures

4.3.3.3 Crack Propagation in a Nanoplate with a Temperature Field

Although a globally constant temperature was assumed in the above simulations, the continuum approximations with the TCB rule can deal with the object in a temperature field. Since it is assumed that atoms have the same harmonic vibration mode locally in the TCB rule, the free energy can be evaluated at the discretized particles with a locally constant temperature in the continuum approximations. Here, we investigate crack propagation in a large nanoplate with the length of 1600nm and the width of 280nm. The nanoplate is subject to a linear temperature field from 100K to 1000K along its longitudinal direction. Consequently, the crack will propagate from a low temperature region to a high temperature region and the crack speed will be increased as illustrated in Fig. 4.20.

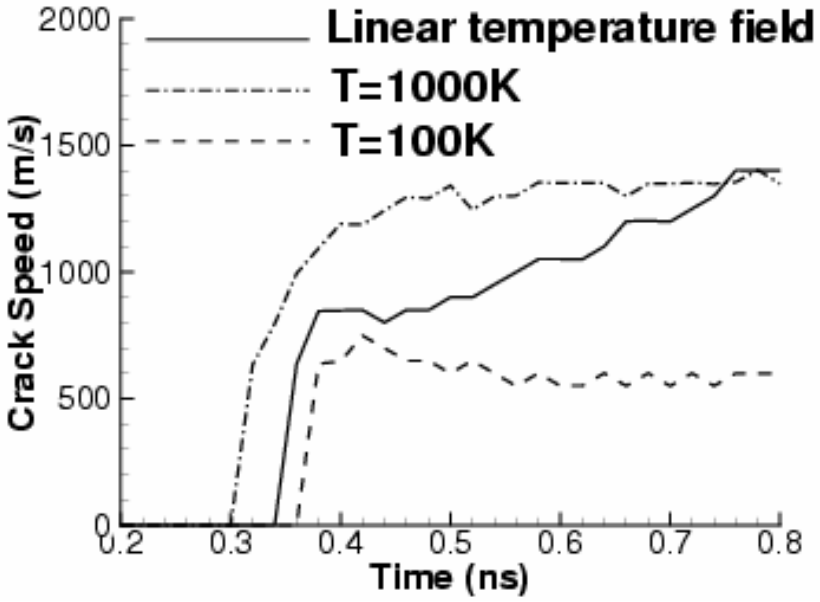

Figure 4.20: Crack propagation speed in linear temperature field

4.3.4 Nanoindentation

Nanoindentation is similar to conventional hardness testing performed on the nanoscale. The force required to press a diamond indenter into a material is measured as a function of indentation depth. Force-depth curves obtained during indenting indicate material properties, such as elastic modulus and hardness. In this example, a nanoscale indenter with the radius of 100nm is pressed into a crystalline with the simple cubic lattice. Lennard-Jones potential, as described in Eq. (3.16) with $l_0 = 1\text{nm}$ and $\varepsilon = 8.25\times10^{-18}\text{J}$, is employed for describing interaction between nearest atoms in the lattice. The mass of each atom is $1.0\times10^{-22}\text{kg}$. The crystalline has the dimensions of $500\text{nm}\times500\text{nm}\times250\text{nm}$ and contains 65 millions atoms. Therefore, the simulation of

nanoindentation is especially appealing for nanoscale continuum approximation since the experimental systems remain larger than the biggest model that can be handled by molecular dynamics. Within the nanoscale meshfree particle model, 8125 particles are used to simulation this nanoindentation problem. The indenter is assumed to be rigid in this example and the deformed configuration of the nanoscale crystalline material is shown in Fig. 4.21.

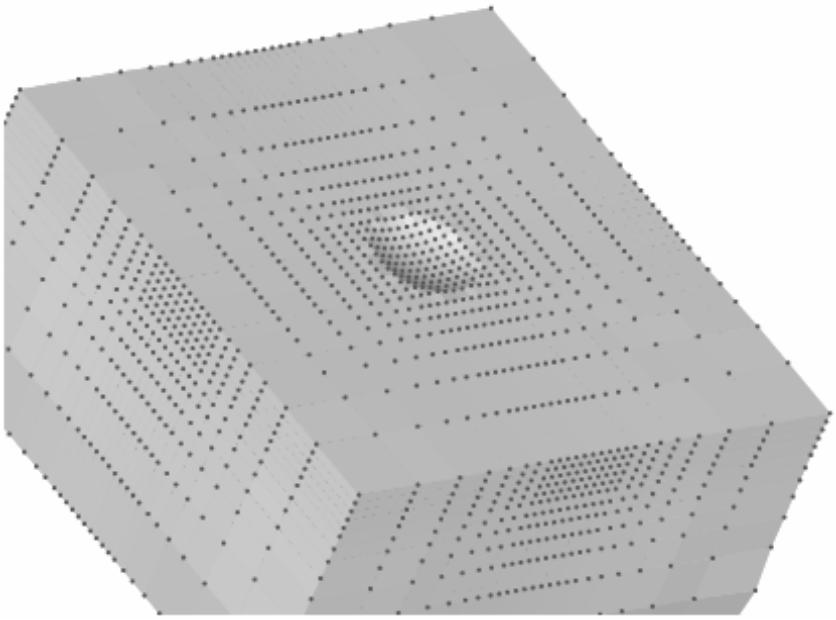

Figure 4.21: Simulation of nanoindentation using meshfree particle methods

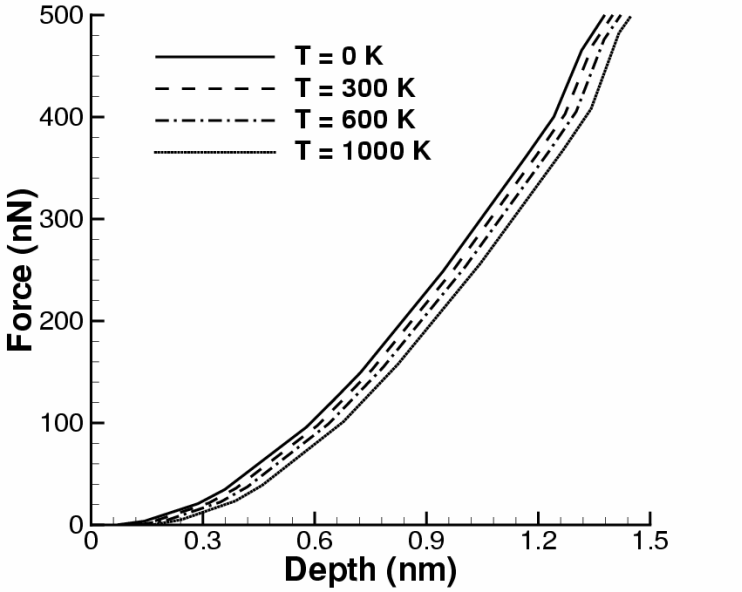

Figure 4.22: Force-depth relations at various temperatures

Fig. 4.22 illustrates the force-depth relations at various temperatures. It can be seen that higher temperature results in lower force loaded on the indenter to reach the same depth. Here we assume that no dislocation occurs so that there are no kinks appearing on the force-depth curves as demonstrated in molecular or multiscale simulations [21]. Once the material instability criterion is setup, we will be able to investigate nucleation of dislocations.

In addition, we investigate the temperature effects on the force loaded on indenters for different materials. We choose different energy depths, ε, in Lennard-Jones potential function so that the corresponding material stiffness are different. To reach the depth of 1nm, the force applied on the indenter decreases when temperature increases. Fig. 4.23 shows that the change of force is larger if the material stiffness is smaller. We conclude that temperature effects are more significant on material with smaller stiffness.

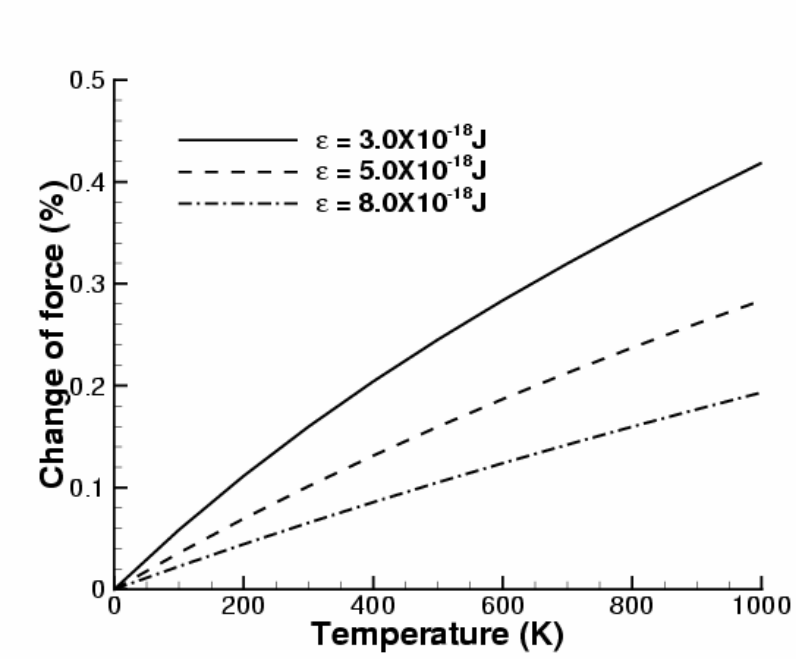

Figure 4.23: Temperature effects on the force loaded on indenters for different materials when the depth is 1nm

4.4 Summary and Conclusions

A nanoscale meshfree particle method with the implementation of the temperature-related Cauchy-Born rule has been proposed. The intrinsic properties of the material associated with each particle could be sought from the atomic level via the TCB rule. Several numerical examples showed that numerical simulations in nanotechnology can be beneficial from the advantages of the meshfree particle methods. This progress could not only save a great amount of computer time but also make it possible to treat extremely large deformation problems and the problems involving discontinuities at nanoscale. Through this hierarchical multiscale method, the nanoscale crack propagation

problem is investigated using visibility criterion and cohesive model. The observed crack propagation phenomena at finite temperatures match the ones in molecular dynamics simulations. It is shown that the temperature effects are significant on the crack propagation speed when the temperature is in a particular range.

CHAPTER 5

TEMPERATUR-DEPENDENT MATERIAL STABILITY

5.1 Introduction

5.1.1 Material Stability

In solid mechanics, both the physical model and numerical discretization affect the reflection of the material properties. But only the material model used in the computational calculation describes the intrinsic properties of the material. The phenomena such as shear bands and fracture are the important symptoms of material stability and are of interest for the researchers in the field of computational mechanics or materials science. The stability of the material model is an important issue because the material model and numerical methods that are intended for failure simulation need to reproduce the onset of material instabilities with reasonable fidelity.

Material instabilities occur in nonassociative plasticity and softening materials where stress decreases with increasing strain. In the early work of Hadamard [60], he examined the question of what happens when the tangent modulus is negative, and identified the conditions for a vanishing propagation speed of an acceleration wave as a material instability. Hill [61] considered an infinite body of the material in a homogeneous state of stress and deformation. He then applied a small perturbation to the body and obtained an expression for its response. If the perturbation grows, the material is considered unstable; otherwise it is stable.

Ogden [62] showed that material instability in equilibrium problems is associated with loss of ellipticity of the incremental equations of equilibrium. Loss of ellipticity will always occur when the tangent modulus loses positive definiteness. But it is also possible

to lose ellipticity condition when the tangent modulus is positive definite. In the dynamic equations, tangent moduli that violate ellipticity conditions lead to loss of hyperbolicity, so that three real positive wave speeds no longer occur in every direction. This is also indicative of a material instability.

Xiao and Belytschko [35] have given material stability analysis of meshfree particle methods in a two-dimensional problem. They pointed out that Eulerian kernels in meshfree particle methods severely distorted the material instability while Lagrangian kernels can exactly reproduce material instability.

The literatures on material stability analysis had given us an extensive view of the material model, but their limitation is that the former researchers didn't consider the temperature effects on the material stability, which is very important issue in material modeling especially for nanostructured materials. In this chapter, we will investigate stability of nanostructured material at finite temperatures. Some examples will illustrate that the temperature effects on nanostructured material stability are significant.

5.1.2 Stability of Crystalline Solids

Most nanostructured materials show their crystal properties. Therefore, the stability of crystalline solids is a very important issue for the novel engineering applications. An ordered crystalline solid consists of a periodic arrangement of atoms that has translational symmetry of the crystal at a distance comparable to the atomic separation. This structure can mathematically be described as a lattice, and the particular arrangement of atoms within the lattice gives rise to various point and space group symmetries that can have a profound effect on the microscopic and macroscopic properties of the material [63, 64, 65]. Under the assumptions of Cauchy-Born rule, the

deformations of the lattice can be expressed in terms of macroscopic deformation gradient **F** of the lattice vectors. If the microstructure is not centrosymmetric, which means the multilattice contains several sublattices that could deform independently, inner displacement (internal shift) vectors should also be considered in the deformation description. The interaction between atoms in a multilattice can be described by the atomic interaction potentials. These include relatively simple pair-potentials and long range interactions.

The stability theory of crystalline solids using multilattice kinematics has been discussed in Elliott's paper [66, 67]. The three different stability criteria are briefly outlined below.

1. Homogenized Continuum (HC) stability

The HC-stability criterion indicates stability with respect to all internally equilibrated "uniform" perturbations at the continuum scale. A "homogenized continuum" energy density is defined as a function only of the deformation gradient by eliminating the inner displacements $\boldsymbol{\eta}$ using strain energy minimization Eq. (3.32).

$$\hat{w}(\mathbf{F}) \equiv w(\mathbf{F}, \boldsymbol{\eta}) \tag{5.1}$$

The crystal's equilibrium configuration $\overset{0}{\mathbf{F}}$ is considered HC-stable if the resulting elastic moduli are positive definite with respect to all deformation gradient, i.e., $\tilde{w}$ is a local minimum at the equilibrium configuration.

$$\delta\mathbf{F}^{\mathrm{T}} : \left.\frac{\partial^2 \hat{w}}{\partial \mathbf{F}^{\mathrm{T}} \partial \mathbf{F}^{\mathrm{T}}}\right|_{\overset{0}{\mathbf{F}}} : \delta\mathbf{F}^{\mathrm{T}} > 0, \quad \forall \delta\mathbf{F}^{\mathrm{T}} \neq 0 \tag{5.2}$$

It is as same as

$$\mathbf{n}^0 \otimes \mathbf{h} : \mathbf{C} : \mathbf{n}^0 \otimes \mathbf{h} > 0 \quad \forall \mathbf{n}^0 \neq 0, \mathbf{h} \neq 0 \tag{5.3}$$

where **C** is the first elasticity tensor, $\mathbf{n}^0$ and **h** are two arbitrary non-zero vectors. HC-stability criterion is identical to strong ellipticity condition and hyperbolicity condition for the time-dependent PDE.

2. Cauchy-Born (CB) Stability

CB-stability provides an intermediate criterion by considering perturbations at both the atomistic and continuum scales. It indicates stability with respect to all "quasi-uniform" perturbations and contains HC-stability as a special case. Here, both the uniform deformation gradient **F** and the inner displacements **η** are allowed to vary independently. The crystal is considered CB-stable if $w(\mathbf{F},\boldsymbol{\eta})$ is a local minimum, or

$$\left[\delta\mathbf{F}^{\mathrm{T}},\delta\boldsymbol{\eta}\right]\begin{bmatrix}\dfrac{\partial^2 w}{\partial\mathbf{F}^{\mathrm{T}}\partial\mathbf{F}^{\mathrm{T}}} & \dfrac{\partial^2 w}{\partial\mathbf{F}^{\mathrm{T}}\partial\boldsymbol{\eta}}\\ \dfrac{\partial^2 w}{\partial\mathbf{F}^{\mathrm{T}}\partial\boldsymbol{\eta}} & \dfrac{\partial^2 w}{\partial\boldsymbol{\eta}\partial\boldsymbol{\eta}}\end{bmatrix}_{\mathbf{F},\boldsymbol{\eta}}^{0,0}\begin{bmatrix}\delta\mathbf{F}^{\mathrm{T}}\\ \delta\boldsymbol{\eta}\end{bmatrix}>0\quad\forall\,\delta\mathbf{F}^{\mathrm{T}}\neq 0,\delta\boldsymbol{\eta}\neq 0 \tag{5.4}$$

The CB-stability criterion bridges the length scales between the phonon- and HC-stability criteria by accounting for the atomic scale inner displacements and a superset of the continuum scale uniform perturbations. But the CB-stability is identical to HC-stability for simple lattices, since there is no inner displacement.

3. Phonon Stability

The phonon-stability is defined in terms of the normal modes of vibration (phonons) for the crystal. It considers the largest set of perturbations and indicates stability with respect to bounded perturbations of all wavelengths at the atomic scale. The phonon-stability is not complete, "uniform" perturbations and the more general "quasi-uniform" perturbations are addressed by CB-stability. In the phonon-stability, all atoms in the crystal are given their three translational degrees of freedom and the linearized

equations of motion are considered. It requires that the natural frequency for each phonon be a real quantity, or equivalently, that the eigenvalues of the crystal's stiffness matrix with respect to all atomic degrees of freedom be positive definite.

From the local harmonic model, the principal frequencies of atom I can be calculated by diagonalizing the local dynamical matrix whose determinant is expressed as

$$\bar{D}_I = \left(\prod_k^n \omega_{Ik} \right)^2 \tag{5.5}$$

The phonon-stability implies that the eigenvalues of the dynamical matrix are real. So, the dynamical matrix must be positive definite to make the lattice phonon-stable since it is always symmetric.

Each of the three stability criteria considered interrogates a different set of perturbations and no single set encompasses the other two; however, some overlap exists. The phonon-stability considers bounded perturbations of all wavelengths and no macroscopic deformation of the crystal exits, since $\delta \mathbf{F}^{\mathrm{T}} = 0$. The CB-stability considers all quasi-uniform perturbations in the continuum level that have nonzero $\delta \mathbf{F}^{\mathrm{T}}$ and independent $\delta \boldsymbol{\eta}$ perturbations. The CB-stability could be reduced to the HC-stability based on the inner relaxation. Physically this may be reasonable, since one can imagine that the characteristic time scale for the internal variable's dynamic evolution to be much shorter that the rate of evolution for the uniform deformation gradient $\mathbf{F}$. Actually, the CB- and HC-stability are identical in case of simple lattices, where there is no inner displacement involved. We will use HC-stability criterion to analyze nanostructured materials at finite temperature, since this stability criterion is based on homogenized continuum energy density and could be used as a material failure indicator in a

continuum level. Also, it has been shown that for hard-device loading (which imposes displacement conditions on the entire boundary of the body), classical continuum mechanics indicates that HC-stability condition is necessary and sufficient for stability [66], and this criterion reflects the stability property merely from material itself.

5.2 Temperature-dependent Material Stability Analysis

In this chapter, we perform a von Neumann stability analysis [61, 68, 69] of nanostructured materials via a homogenization technique. As a difference from HC-stability mentioned in the above, we employ the temperature-related CB rule because we believe temperature effects on nanoscale material instability are significant. We first derive the linearized equations. Perturbations in the displacement are assumed as follows,

$$\bar{\mathbf{u}} = \mathbf{u} + \tilde{\mathbf{u}} \tag{5.6}$$

where the superposed ~ denotes a perturbation. The perturbed solutions are governed by the following equation:

$$\rho_0 \ddot{\tilde{\mathbf{u}}} = \nabla_{\mathbf{X}} \cdot \tilde{\mathbf{P}} \tag{5.7}$$

where ρ_0 is the initial density, $\tilde{\mathbf{P}}$ is the perturbation of the nominal stress and $\nabla_{\mathbf{X}}$ is the gradient with respect to the material (reference) coordinates. From the TCB rule, Eq. (3.14), the perturbation of the nominal stress is

$$\tilde{\mathbf{P}} = \frac{\partial^2 w_H(\mathbf{F},T)}{\partial \mathbf{F}^{\mathrm{T}} \partial \mathbf{F}^{\mathrm{T}}} \cdot \tilde{\mathbf{F}}^{\mathrm{T}} = \mathbf{C}(\mathbf{F},T) \cdot \tilde{\mathbf{F}}^{\mathrm{T}} \tag{5.8}$$

where $\mathbf{C}(\mathbf{F},T)$ is the temperature-related first elasticity tensor, or first tangential stiffness [33]. Writing Eq. (5.8) in indicial form, the perturbed stress is given by

$$\tilde{P}_{ij} = C_{ijkl}\tilde{F}_{lk} = A_{ijkl}\tilde{F}_{lk} \tag{5.9}$$

The governing equation in terms of the perturbed displacements can be obtained by substituting Eq. (5.9) into Eq. (5.7)

$$\rho_0 \frac{\partial^2 \tilde{u}_i}{\partial t^2}(\mathbf{X},t) = \frac{\partial}{\partial X_j}\left[C_{ijkl}(\mathbf{X},t)\tilde{F}_{lk}(\mathbf{X},t)\right] = \frac{\partial}{\partial X_j}\left(C_{ijkl}\frac{\partial \tilde{u}_l}{\partial X_k}\right) \tag{5.10}$$

Assuming that the perturbation of displacements is in the form of a plane wave

$$\tilde{\mathbf{u}} = \mathbf{g}e^{\mathrm{i}\omega t + i\kappa \mathbf{n}^0 \cdot \mathbf{X}} = \mathbf{g}e^{\alpha(\mathbf{X},t)} \tag{5.11}$$

where, $\mathbf{g}$ is polarization of the wave, κ is wave number, ω is frequency and $\mathbf{n}^0$ is the normal direction of the wave front with respect to the initial configuration [90]. Then

$$\tilde{F}_{lk} = \frac{\partial \tilde{u}_l}{\partial X_k} = \mathrm{i}\kappa g_l n_k^0 e^{\alpha(\mathbf{X},t)} \tag{5.12}$$

and

$$\frac{\partial}{\partial X_j}\left(C_{ijkl}\tilde{F}_{lk}\right) = \mathrm{i}\kappa C_{ijkl} g_l n_k^0 \mathrm{i}\kappa n_j^0 e^{\alpha(\mathbf{X},t)} = -\kappa^2 C_{ijkl} n_k^0 n_j^0 g_l e^{\alpha(\mathbf{X},t)} \tag{5.13}$$

Since

$$\frac{\partial^2 \tilde{u}_i}{\partial t^2} = -\omega^2 g_i e^{\alpha(\mathbf{X},t)} \tag{5.14}$$

The perturbed equation Eq. (5.10) yields

$$-\rho_0 \omega^2 g_i + \kappa^2 C_{ijkl} n_k^0 n_j^0 g_l = 0 \quad \text{for} \quad i = 1 \quad \text{to} \quad N \tag{5.15}$$

or

$$\left(\frac{\omega^2}{\kappa^2}\delta_{il} - \frac{1}{\rho_0}A_{il}^{\ 0}\right) g_l = 0\,, \quad A_{il}^{\ 0} = C_{ijkl} n_j^0 n_k^0 \tag{5.16}$$

$\boldsymbol{A}^{\,0}\left(\mathbf{n}^0\right)$ is called the acoustic tensor. The above is a set of homogeneous linear algebraic equations. Nontrivial solutions exist only when the determinant vanishes. Thus, the characteristic equation for the continuum medium is

$$\det\left[\frac{\omega^2}{\kappa^2}\delta_{il} - \frac{1}{\rho_0}A_{il}^{0}\right] = 0 \tag{5.17}$$

If the matrix $\boldsymbol{A}^{0}$ is positive definite, then the roots ω must be real and the nanostructured material is stable. Note that instabilities can occur when $\boldsymbol{A}^{0}$ loses positive definiteness, which can occur due to strain-softening.

5.3 Applications

5.3.1 One-dimensional Stability Analysis

We first conduct one-dimensional stability analysis. The perturbation of displacement takes the form of a plane wave in the X-direction as:

$$\tilde{u} = ge^{\mathrm{i}\kappa x + \mathrm{i}\omega t} \tag{5.18}$$

The governing equations in one dimension are

$$\rho_0\ddot{u} = \frac{\partial P}{\partial X} + \rho_0 b \tag{5.19}$$

and

$$P = \frac{\partial w_H}{\partial F} \tag{5.20}$$

The equations for the perturbed solutions corresponding to Eq. (5.7) – Eq. (5.9) are

$$\rho_0\ddot{\tilde{u}} = \frac{\partial \tilde{P}}{\partial X} \tag{5.21}$$

$$\tilde{P} = \frac{\partial^2 w_H}{\partial F^2}\tilde{F} = C\tilde{F} \tag{5.22}$$

where $\tilde{u}$ is the perturbed displacement in the x-direction, $\tilde{P}$ is the perturbation of the nominal stress, F and $\tilde{F}$ are the deformation gradient and its perturbation respectively.

In this section we consider a one-dimensional molecule chain as shown in Fig. 3.1. We assume that the molecule chain contains N atoms and the mass for each atom is m_0. The bond length in equilibrium state and bond potential between any of the two nearest neighboring atoms are l_0 and $\varphi(l)$ respectively. Periodic boundary conditions are employed.

The unit cell of this molecule chain contains one atom and two half-bonds. The free energy density for this unit cell under temperature T can be calculated as

$$\begin{aligned} w_H &= \frac{1}{l_0}\left\{\varphi(l)+\kappa_B T \ln\left[\frac{\hbar\sqrt{\bar{D}}}{\kappa_B T}\right]\right\} \\ &= \frac{1}{l_0}\left\{\varphi(l)+\kappa_B T\left[\ln\left(\frac{\hbar}{\kappa_B T}\right)+\frac{1}{2}\ln(\varphi'')-\frac{1}{2}\ln(m_0)\right]\right\} \end{aligned} \tag{5.23}$$

where $\bar{D}$ is the determinant of the dynamical matrix which can be written as

$$\bar{D} = \frac{1}{m_0}\frac{\partial^2\varphi}{\partial x^2} = \frac{1}{m_0}\frac{\partial^2\varphi}{\partial l^2} = \frac{\varphi''}{m_0} \tag{5.24}$$

The nominal stress derived from the free energy density can be calculated as

$$\begin{aligned} P &= \frac{\partial w_H}{\partial F} = \frac{\partial w_H}{\partial l}\frac{\partial l}{\partial F} \\ &= \frac{1}{l_0}\left\{\varphi'(l)+\frac{\partial}{\partial l}\left[\frac{1}{2}\kappa_B T\ln(\varphi'')\right]\right\} l_0 \\ &= \varphi'(l)+\frac{1}{2}\kappa_B T\frac{\varphi'''(l)}{\varphi''(l)} \end{aligned} \tag{5.25}$$

And then, the temperature-related first tangential stiffness is

$$
\begin{aligned}
C &= \frac{\partial P}{\partial F} = \frac{\partial P}{\partial l}\frac{\partial l}{\partial F} \\
&= \frac{\partial}{\partial l}\left[\varphi'(l) + \frac{1}{2}\kappa_B T \frac{\varphi'''(l)}{\varphi''(l)}\right] l_0 \\
&= l_0 \left\{ \varphi''(l) + \frac{\kappa_B T}{2}\frac{\varphi^{(4)}(l)}{\varphi''(l)} - \frac{\kappa_B T}{2}\left[\frac{\varphi'''(l)}{\varphi''(l)}\right]^2 \right\}
\end{aligned}
\tag{5.26}
$$

The linearized equation in terms of the perturbed displacement can be written as

$$
\rho_0 \frac{\partial^2 \tilde{u}}{\partial t^2} = \frac{\partial}{\partial X}\left(C\frac{\partial \tilde{u}}{\partial X}\right) = C\frac{\partial^2 \tilde{u}}{\partial X^2} \tag{5.27}
$$

Substituting the Fourier representation of the perturbed solution, Eq. (5.18) into Eq. (5.27) yields that the stability is governed by

$$
\omega^2 = \frac{C\kappa^2}{\rho_0} \tag{5.28}
$$

It can be seen that the solution becomes unstable only when $C < 0$. The criterion for material stability of the molecule chain is

$$
\varphi''(F) + \frac{\kappa_B T}{2}\frac{\varphi^{(4)}(F)}{\varphi''(F)} - \frac{\kappa_B T}{2}\left[\frac{\varphi'''(F)}{\varphi''(F)}\right]^2 \geq 0 \tag{5.29}
$$

Fig. 5.1 shows the stable domain of the molecule chain based on the HC-stability criterion, Eq. (5.29). Lennard-Jones 6-12 potential was used in this example to describe the atomistic interaction with the parameter $\varepsilon = 8.25\times10^{-17}\,\mathrm{J}$. Various deformation gradients and temperatures up to 3000K are considered. It can be seen that the stable domain gets smaller with increasing temperature. It should be noted that the locally harmonic mode for atom vibration might be invalid at higher temperatures that are close to the material melting temperature. In addition, molecular dynamics is conducted at selected deformation gradients and temperatures to verify the continuum-approached

material stability analysis. In molecular dynamics, the molecule chain contains 200 atoms. Instability occurs when the length of one bond is larger than the cutoff distance of the Lennard-Jones potential function. In other words, the molecule chain is broken. In Figure 5.1, empty circles represent the stable molecule chains, while the solid circles represent the unstable molecule chains. As evidenced, the molecular dynamics results support the linearized stability analysis.

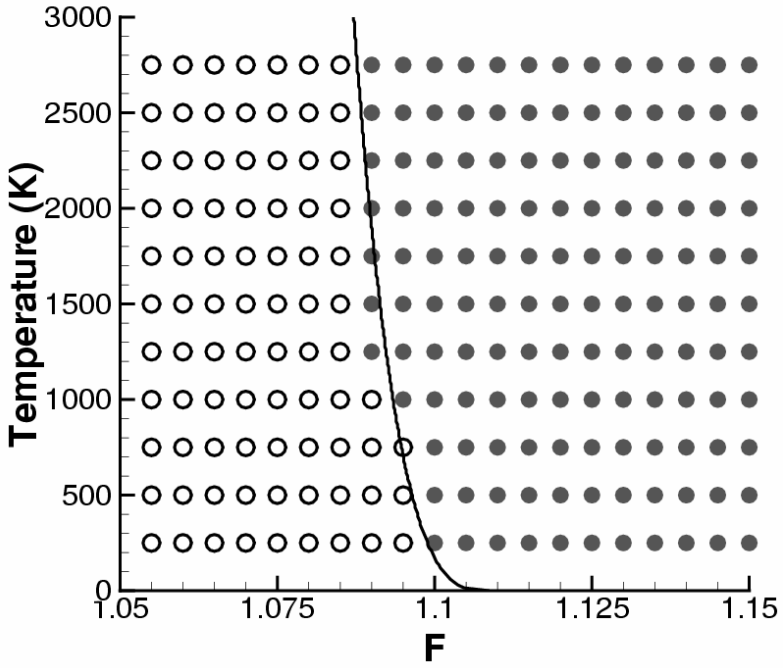

Figure 5.1: Stable domain of 1-D molecule chain

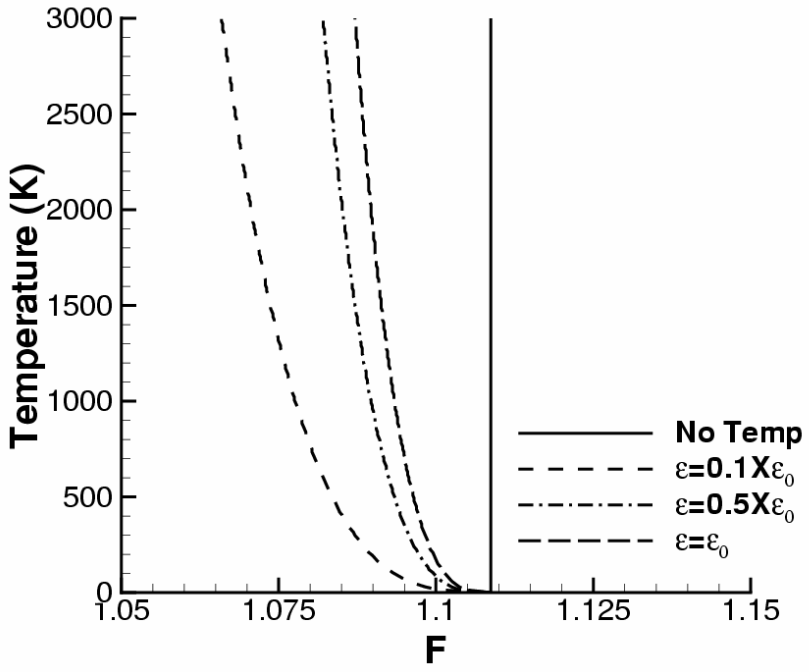

Figure 5.2: Temperature-dependent stability analysis for 1-D molecule chain

In Fig. 5.2, the lines represent the boundaries of the stable domain for different material parameters. One the left side of each line is the stable domain for each case. We can see if we do not consider the temperature effect, which means there is only the first term in Eq. (5.29), the boundary of stable domain is a temperature independent straight line. As the material parameter goes smaller, the stable domain is getting smaller, which makes sense since the softer material is easier to lose its stability at high temperature.

5.3.2 Two-dimensional Stability Analysis

Then we consider a two-dimensional problem to investigate material stability in higher dimensions. From Eq. (5.8) the perturbation of the nominal stress **P** can be

computed via the temperature-related first elasticity tensor $\mathbf{C}$. In higher dimension, it can be written as

$$\mathbf{C} = \frac{\partial^2 w_C}{\partial \mathbf{F}^{\mathrm{T}} \partial \mathbf{F}^{\mathrm{T}}} + \frac{\kappa_B T}{2\bar{D}} \frac{\partial^2 \bar{D}}{\partial \mathbf{F}^{\mathrm{T}} \partial \mathbf{F}^{\mathrm{T}}} - \frac{\kappa_B T}{2\bar{D}^2} \frac{\partial \bar{D}}{\partial \mathbf{F}^{\mathrm{T}}} \otimes \frac{\partial \bar{D}}{\partial \mathbf{F}^{\mathrm{T}}} \tag{5.30}$$

or

$$C_{ijkl} = \frac{\partial^2 w_C}{\partial F_{ji} \partial F_{lk}} + \frac{\kappa_B T}{2\bar{D}} \frac{\partial^2 \bar{D}}{\partial F_{ji} \partial F_{lk}} - \frac{\kappa_B T}{2\bar{D}^2} \frac{\partial \bar{D}}{\partial F_{ji}} \otimes \frac{\partial \bar{D}}{\partial F_{lk}} \tag{5.31}$$

in indicial form. The summation on the RHS is over all the bonds in a unit cell, and $\bar{D}$ is the determinant of the dynamical matrix. w_C is the strain energy density at 0K. If the strain energy density in a nanostructured material can be written as a summation of the bond potentials,

$$w_C = \sum_k \varphi(l_k) \tag{5.32}$$

then the first term on the RHS of Eq. (5.30) and Eq. (5.31) can be calculated as

$$\frac{\partial^2 w_C}{\partial \mathbf{F}^{\mathrm{T}} \partial \mathbf{F}^{\mathrm{T}}} = \sum_k \left[\varphi''(l_k) \frac{\partial l_k}{\partial \mathbf{F}^{\mathrm{T}}} \otimes \frac{\partial l_k}{\partial \mathbf{F}^{\mathrm{T}}} + \varphi'(l_k) \frac{\partial^2 l_k}{\partial \mathbf{F}^{\mathrm{T}} \partial \mathbf{F}^{\mathrm{T}}} \right] \tag{5.33}$$

or

$$\frac{\partial^2 w_C}{\partial F_{ji} \partial F_{lk}} = \sum_k \left[\varphi''(l_k) \frac{\partial l_k}{\partial F_{ji}} \otimes \frac{\partial l_k}{\partial F_{lk}} + \varphi'(l_k) \frac{\partial^2 l_k}{\partial F_{ji} \partial F_{lk}} \right] \tag{5.34}$$

in indicial form. We ignore the off-diagonal components in dynamical matrix since they are pretty small compare to the diagonal components. Therefore, in a two-dimensional lattice the determinant of a dynamical matrix is

$$\bar{D} = D_{11} D_{22} \tag{5.35}$$

and

$$\frac{\partial \bar{D}}{\partial \mathbf{F}^{\mathrm{T}}} = \frac{\partial D_{11}}{\partial \mathbf{F}^{\mathrm{T}}} D_{22} + D_{11} \frac{\partial D_{22}}{\partial \mathbf{F}^{\mathrm{T}}} \tag{5.36}$$

The first derivative of the diagonal components with respect to the deformation gradient, from Eq. (3.28), is

$$\begin{aligned} \frac{\partial D_{ii}}{\partial \mathbf{F}^{\mathrm{T}}} = \sum_k \Bigg[& \varphi'''(l_k) \left(\frac{r_{ki}}{l_k}\right)^2 \frac{\partial l_k}{\partial \mathbf{F}^{\mathrm{T}}} + 2\varphi''(l_k) \frac{r_{ki}}{l_k^2} \frac{\partial r_{ki}}{\partial \mathbf{F}^{\mathrm{T}}} - 3\varphi''(l_k) \frac{r_{ki}^2}{l_k^3} \frac{\partial l_k}{\partial \mathbf{F}^{\mathrm{T}}} \\ & + \varphi''(l_k) \frac{1}{l_k} \frac{\partial l_k}{\partial \mathbf{F}^{\mathrm{T}}} + 3\varphi'(l_k) \frac{r_{ki}^2}{l_k^4} \frac{\partial l_k}{\partial \mathbf{F}^{\mathrm{T}}} - \varphi'(l_k) \frac{1}{l_k^2} \frac{\partial l_k}{\partial \mathbf{F}^{\mathrm{T}}} - 2\varphi'(l_k) \frac{r_{ki}}{l_k^3} \frac{\partial r_{ki}}{\partial \mathbf{F}^{\mathrm{T}}} \Bigg] \end{aligned} \tag{5.37}$$

And

$$\frac{\partial^2 \bar{D}}{\partial \mathbf{F}^{\mathrm{T}} \partial \mathbf{F}^{\mathrm{T}}} = \frac{\partial^2 D_{11}}{\partial \mathbf{F}^{\mathrm{T}} \partial \mathbf{F}^{\mathrm{T}}} D_{22} + 2 \frac{\partial D_{11}}{\partial \mathbf{F}^{\mathrm{T}}} \otimes \frac{\partial D_{22}}{\partial \mathbf{F}^{\mathrm{T}}} + D_{11} \frac{\partial^2 D_{22}}{\partial \mathbf{F}^{\mathrm{T}} \partial \mathbf{F}^{\mathrm{T}}} \tag{5.38}$$

The second derivative of the diagonal components with respect to the deformation gradient is

$$\begin{aligned} \frac{\partial^2 D_{ii}}{\partial \mathbf{F}^{\mathrm{T}} \partial \mathbf{F}^{\mathrm{T}}} = \sum_k \Bigg\{ & \left[\varphi'''(l_k) \left(\frac{r_{ki}}{l_k}\right)^2 - \varphi''(l_k) \left(3\frac{r_{ki}^2}{l_k^3} - \frac{1}{l_k} \right) + \varphi'(l_k) \left(3\frac{r_{ki}^2}{l_k^4} - \frac{1}{l_k^2} \right) \right] \frac{\partial^2 l_k}{\partial \mathbf{F}^{\mathrm{T}} \partial \mathbf{F}^{\mathrm{T}}} \\ & + \left[\varphi^{(4)}(l_k) \left(\frac{r_{ki}}{l_k}\right)^2 - \varphi'''(l_k) \left(5\frac{r_{ki}^2}{l_k^3} - \frac{1}{l_k} \right) + \varphi''(l_k) \left(12\frac{r_{ki}^2}{l_k^4} - \frac{2}{l_k^2} \right) \right. \\ & \left. - \varphi'(l_k) \left(12\frac{r_{ki}^2}{l_k^5} - \frac{2}{l_k^3} \right) \right] \frac{\partial l_k}{\partial \mathbf{F}^{\mathrm{T}}} \otimes \frac{\partial l_k}{\partial \mathbf{F}^{\mathrm{T}}} + \left[2\varphi''(l_k) \frac{1}{l_k^2} - 2\varphi'(l_k) \frac{1}{l_k^3} \right] \frac{\partial r_{ki}}{\partial \mathbf{F}^{\mathrm{T}}} \otimes \frac{\partial r_{ki}}{\partial \mathbf{F}^{\mathrm{T}}} \\ & + \left[2\varphi'''(l_k) \frac{r_{ki}}{l_k^2} - 6\varphi''(l_k) \frac{r_{ki}}{l_k^3} + 6\varphi'(l_k) \frac{r_{ki}}{l_k^4} \right] \frac{\partial l_k}{\partial \mathbf{F}^{\mathrm{T}}} \otimes \frac{\partial r_{ki}}{\partial \mathbf{F}^{\mathrm{T}}} \\ & + \left[2\varphi'''(l_k) \frac{r_{ki}}{l_k^2} - 6\varphi''(l_k) \frac{r_{ki}}{l_k^3} + 6\varphi'(l_k) \frac{r_{ki}}{l_k^4} \right] \frac{\partial r_{ki}}{\partial \mathbf{F}^{\mathrm{T}}} \otimes \frac{\partial l_k}{\partial \mathbf{F}^{\mathrm{T}}} \Bigg\} \end{aligned} \tag{5.39}$$

Followed the discussion for temperature-dependent material stability, a simple sufficient condition for stability can be deduced when the acoustic tensor $\boldsymbol{A}^{0}$ is symmetric: the positive definiteness of the acoustic tensor for all $\mathbf{n}^0$ is sufficient for

stability. The acoustic tensor $\boldsymbol{A}^{0}$ is symmetric when $\mathbf{C}$ has major symmetry. This is guaranteed by Eq. (5.30).

The positive definiteness of $\boldsymbol{A}^{0}$ for all $\mathbf{n}^{0}$ can also be expressed as

$$C_{ijkl} n_j^0 n_k^0 h_i h_l > 0 \quad \forall \mathbf{n}^0 \neq 0, \mathbf{h} \neq 0 \tag{5.40}$$

or

$$\mathbf{n}^0 \otimes \mathbf{h} : \mathbf{C} : \mathbf{n}^0 \otimes \mathbf{h} > 0 \tag{5.41}$$

where

$$n_1^0 = \cos\alpha \quad n_2^0 = \sin\alpha$$

$$h_1 = \cos\beta \quad h_2 = \sin\beta$$

and α and β are arbitrary angles. This is called the strong ellipticity condition or the hyperbolicity conditions for the time dependent PDE. When the strong ellipticity holds, the PDE for equilibrium is elliptic, the roots ω will be real and the continuum is stable.

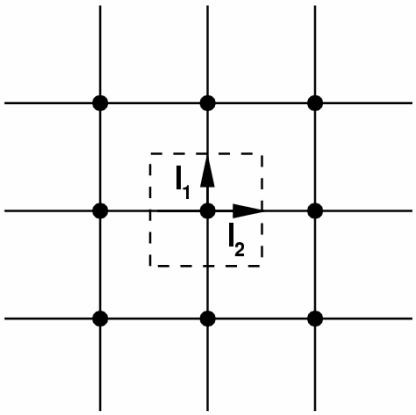

Figure 5.3: Quadrilateral molecular structure with its unit cell

In the numerical example, we only consider two-dimensional bi-axial tension problem for simplicity. The deformation gradient is in the form

$$\mathbf{F} = \begin{bmatrix} \lambda_1 & 0 \\ 0 & \lambda_2 \end{bmatrix} \tag{5.42}$$

where λ_1 and λ_2 are the stretching in the x and y direction, respectively.

We consider a quadrilateral lattice, which is shown in Fig. 5.3, with Lennard-Jones material whose $\varepsilon = 8.25\times10^{-18}\,\mathrm{J}$ and $l_0 = 1\mathrm{nm}$. In this lattice there are two independent bonds in the unit cell, $k = 2$, and

$$r_{11} = F_{11}l_0\,,\ r_{12} = F_{21}l_0\,,$$

$$r_{21} = F_{12}l_0\,,\ r_{22} = F_{22}l_0\,.$$

If there exists ω_I such that $\mathrm{Im}(\omega_I) < 0$ for any α , the nanostructured material will be unstable. The stable domain for the material considered above is shown in Fig. 5.4. The entire compressive domain $(0 < \lambda_i \le 1)$ is stable. However, for sufficiently large extensional deformations, the material is unstable. It also can be seen that the stable domain is smaller at a higher temperature.

To study temperature effects on nanostructured material instability, we employ various energy well depths, ε , in the Lennard-Jones potential function. Three values are considered: $\varepsilon_0 = 8.25\times10^{-18}\,\mathrm{J}$ for material 1, $0.1\times\varepsilon_0$ for material 2, and $0.01\times\varepsilon_0$ for material 3. Obviously, material 1 is ten times stiffer than material 2 that is ten times stiffer than material 3. At zero temperature, those three materials have the same material stability. However, at a room temperature of 300K, the stiffest material (material 1) has the largest stable domain, shown in Fig. 5.5.

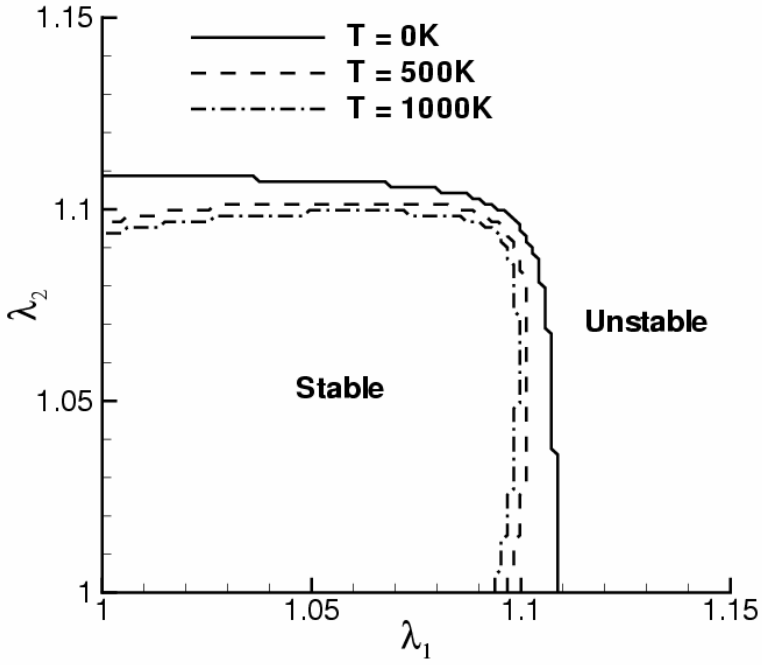

Figure 5.4: Stable domains at various temperatures

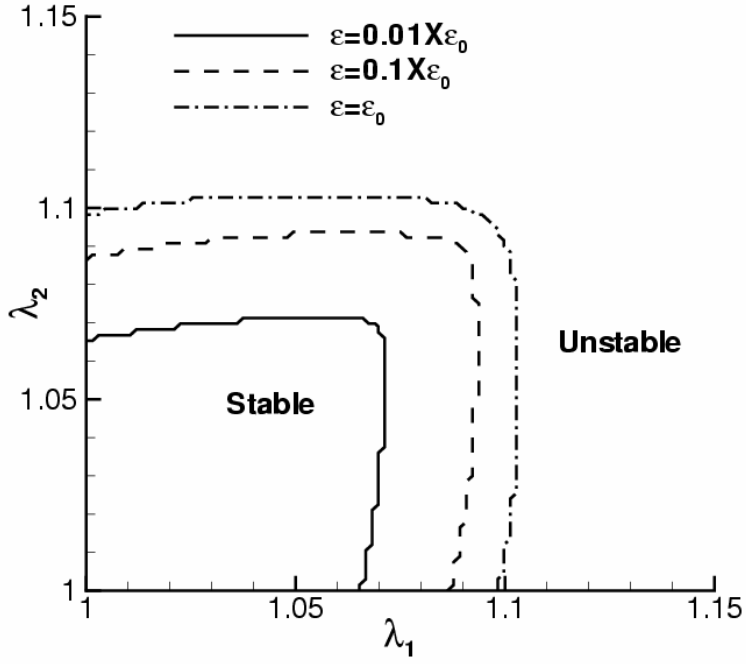

Figure 5.5: Stable domains of different materials at room temperature of 300K

5.3.3 Stability Analysis of the Graphene Sheet

As a more practical example, we consider temperature effects on the material stability of a graphene sheet. A graphene sheet has a honeycomb multi-lattice, and the unit cell is shown in Fig. 5.6. We have mentioned that the honeycomb multi-lattice is a Bravais multi-lattice, which has two types of basic nuclei shown as black and white dots in Fig. 5.6. Obviously, one basic nucleus and two simple Bravais lattice vectors cannot represent the entire lattice when the graphene sheet is subject to a homogeneous deformation. Therefore, the inner displacement, $\boldsymbol{\eta}$, as a shift vector must be introduced to define the relative displacement between the two types of basic nuclei. Consequently, the strain energy density is a function of inner displacements and deformation gradients.

Both the HC stability and the CB stability consider material stability when the crystal solid is subject to a continuum-level deformation gradient. The role of the inner displacement in analyzing material stability determines whether using the HC stability or the CB stability. If the inner displacement has insignificant effect on material stability, the HC stability should be employed. Indeed, the HC stability criterion indicates stability with respect to all internally equilibrated "uniform" perturbations at the macroscopic continuum scale. A "homogenized continuum" energy density is defined as a function only of the deformation gradient by eliminating the inner displacements using energy minimization. The CB stability provides an intermediate criterion by considering perturbations at both the atomistic and continuum scales. It indicates stability with respect to all "quasi-uniform" perturbations and includes HC stability as a special case. In the CB stability, both the uniform deformation gradient and the inner displacements are allowed to vary independently. In our research, we mainly consider the HC stability.

According to the HC stability, the crystal's equilibrium configuration is considered stable if the resulting elastic moduli are positive definite with respect to all deformation gradients. The HC stability criterion is identical to the strong ellipticity condition and hyperbolicity condition for the time-dependent PDE.

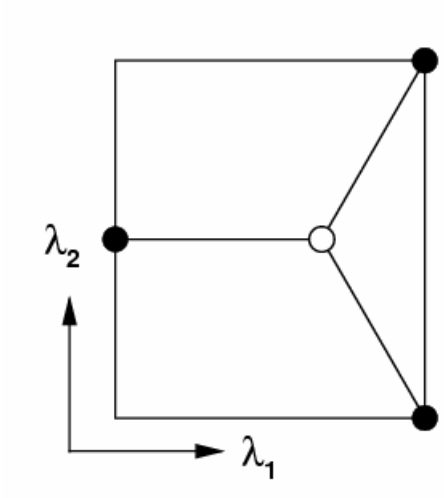

Figure 5.6: Unit cell of graphene sheet

We employ the modified Morse potential function [56] with the same parameters we used in the previous chapter to describe the interatomic interaction. Based on the TCB rule, the nominal stress is derived as

$$\begin{aligned}\mathbf{P} &= \frac{\mathrm{d}w_H}{\mathrm{d}\mathbf{F}^{\mathrm{T}}} = \frac{\partial w_H}{\partial \mathbf{F}^{\mathrm{T}}} + \frac{\partial w_H}{\partial \boldsymbol{\eta}}\frac{\partial \boldsymbol{\eta}}{\partial \mathbf{F}^{\mathrm{T}}} \\ &= \frac{\partial w_C}{\partial \mathbf{F}^{\mathrm{T}}} + \frac{\kappa_B T}{2A_0\bar{D}}\frac{\partial \bar{D}}{\partial \mathbf{F}^{\mathrm{T}}} + \left(\frac{\partial w_C}{\partial \boldsymbol{\eta}} + \frac{\kappa_B T}{2A_0\bar{D}}\frac{\partial \bar{D}}{\partial \boldsymbol{\eta}}\right)\frac{\partial \boldsymbol{\eta}}{\partial \mathbf{F}^{\mathrm{T}}}\end{aligned} \tag{5.43}$$

where A_0 is the area of the unit cell in reference configuration. We neglect the temperature effects on inner displacements since they are in the internal equilibrium. Similar to the work by Tadmor et al. [55], the inner displacement is calculated via the

minimization of the strain energy density with respect to $\boldsymbol{\eta}$ for a given deformation of the lattice, i.e.,

$$\boldsymbol{\eta}(\mathbf{F}) = \arg\left(\min_{\boldsymbol{\eta}} w_C(\mathbf{F}, \boldsymbol{\eta}) \right) \Rightarrow \left. \frac{\partial w_C(\mathbf{F}, \boldsymbol{\eta})}{\partial \boldsymbol{\eta}} \right|_{\mathbf{F}} = 0 \tag{5.44}$$

Then the nominal stress is

$$\mathbf{P} = \frac{\partial w_C}{\partial \mathbf{F}^{\mathrm{T}}} + \frac{\kappa_B T}{2A_0 \bar{D}} \frac{\partial \bar{D}}{\partial \mathbf{F}^{\mathrm{T}}} + \frac{\kappa_B T}{2A_0 \bar{D}} \frac{\partial \bar{D}}{\partial \boldsymbol{\eta}} \frac{\partial \boldsymbol{\eta}}{\partial \mathbf{F}^{\mathrm{T}}} \tag{5.45}$$

Since

$$\frac{\partial^2 w_C}{\partial \boldsymbol{\eta} \partial \mathbf{F}^{\mathrm{T}}} + \frac{\partial^2 w_C}{\partial \boldsymbol{\eta} \partial \boldsymbol{\eta}} \frac{\partial \boldsymbol{\eta}}{\partial \mathbf{F}^{\mathrm{T}}} = 0 \tag{5.46}$$

the stress then further reduced to

$$\mathbf{P} = \frac{\partial w_C}{\partial \mathbf{F}^{\mathrm{T}}} + \frac{\kappa_B T}{2A_0 \bar{D}} \frac{\partial \bar{D}}{\partial \mathbf{F}^{\mathrm{T}}} - \frac{\kappa_B T}{2A_0 \bar{D}} \frac{\partial \bar{D}}{\partial \boldsymbol{\eta}} \left(\frac{\partial^2 w_C}{\partial \boldsymbol{\eta} \partial \boldsymbol{\eta}} \right)^{-1} \frac{\partial^2 w_C}{\partial \boldsymbol{\eta} \partial \mathbf{F}^{\mathrm{T}}} \tag{5.47}$$

And the first tangential stiffness tensor is

$$\begin{aligned}
\mathbf{C} &= \frac{\mathrm{d}\mathbf{P}}{\mathrm{d}\mathbf{F}^{\mathrm{T}}} = \frac{\partial^2 w_H}{\partial \mathbf{F}^{\mathrm{T}} \partial \mathbf{F}^{\mathrm{T}}} + \frac{\partial^2 w_H}{\partial \mathbf{F}^{\mathrm{T}} \partial \boldsymbol{\eta}} \frac{\partial \boldsymbol{\eta}}{\partial \mathbf{F}^{\mathrm{T}}} \\
&= \frac{\partial^2 w_H}{\partial \mathbf{F}^{\mathrm{T}} \partial \mathbf{F}^{\mathrm{T}}} - \frac{\partial^2 w_H}{\partial \mathbf{F}^{\mathrm{T}} \partial \boldsymbol{\eta}} \left(\frac{\partial^2 w_C}{\partial \boldsymbol{\eta} \partial \boldsymbol{\eta}} \right)^{-1} \frac{\partial^2 w_C}{\partial \boldsymbol{\eta} \partial \mathbf{F}^{\mathrm{T}}} \\
&= \frac{\partial^2 w_C}{\partial \mathbf{F}^{\mathrm{T}} \partial \mathbf{F}^{\mathrm{T}}} + \frac{\kappa_B T}{2A_0 \bar{D}} \frac{\partial^2 \bar{D}}{\partial \mathbf{F}^{\mathrm{T}} \partial \mathbf{F}^{\mathrm{T}}} - \frac{\kappa_B T}{2A_0 \bar{D}^2} \frac{\partial \bar{D}}{\partial \mathbf{F}^{\mathrm{T}}} \otimes \frac{\partial \bar{D}}{\partial \mathbf{F}^{\mathrm{T}}} \\
&\quad - \left(\frac{\partial^2 w_C}{\partial \mathbf{F}^{\mathrm{T}} \partial \boldsymbol{\eta}} + \frac{\kappa_B T}{2A_0 \bar{D}} \frac{\partial^2 \bar{D}}{\partial \mathbf{F}^{\mathrm{T}} \partial \boldsymbol{\eta}} - \frac{\kappa_B T}{2A_0 \bar{D}^2} \frac{\partial \bar{D}}{\partial \mathbf{F}^{\mathrm{T}}} \otimes \frac{\partial \bar{D}}{\partial \boldsymbol{\eta}} \right) \left(\frac{\partial^2 w_C}{\partial \boldsymbol{\eta} \partial \boldsymbol{\eta}} \right)^{-1} \frac{\partial^2 w_C}{\partial \boldsymbol{\eta} \partial \mathbf{F}^{\mathrm{T}}}
\end{aligned} \tag{5.48}$$

This indicator can be used to determine whether the material is stable or unstable under certain deformation and temperature. But we should notice that here the strain energy density w_C and dynamical matrix $\mathbf{D}$ are not only the function of bond stretching potential but also the angle bending potential. The derivatives of the strain energy density

and the determinant of the dynamical matrix with respect to the inner displacement can be derived similarly to the derivates with respect to the deformation gradient, which are shown in the previous chapter.

During our analyses, we find that if the graphene sheet is subject to deformation on the direction of λ_1, shown in Fig. 5.6, the inner displacement plays a significant role in the stability of the graphene sheet. In this case, the CB criterion [66, 67] has to be applied. In our research, we only conduct stability analysis when the graphene sheet is subject to elongation on the direction of λ_2, i.e., $\lambda_1 = 1$, because the effect of the inner displacement can be neglected. It should be noted that the λ_2 direction coincides to the axial direction of an armchair carbon nanotube. Since size effects of large armchair carbon nanotubes can be negligible [70], stability analysis performed here can assist in the prediction of failure strains of armchair nanotubes, as shown in Fig. 5.7. It can be seen that at the room temperature of 300 K, the failure strain is 13.5%. Taking the average secant Young's modulus [70] of 800 GPa for carbon nanotubes, the failure stress of armchair tubes at room temperature is 108 GPa, which is in good agreement with molecular dynamics simulation, 110 GPa [71].

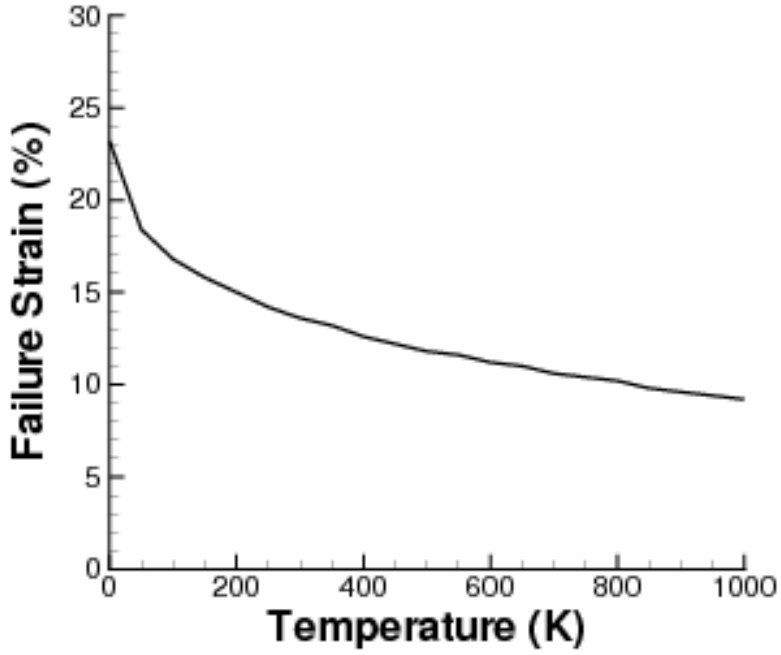

Figure 5.7: Failure strain of the graphene sheet along λ_2 direction for different temperatures

5.4 Summary and Conclusions

The general concept of material stability and several different stability criteria of crystalline solids have been introduced and compared. A standard linearized stability analysis process has been conducted for nanostructured materials using temperature-dependent homogenization technique. It has been showed that the temperature-dependent intrinsic stability of a crystalline solid could be reflected by TCB rule. Stability analyses of a 1D molecule chain and 2D lattices verified that the stability states from TCB rule are the same as the ones from molecular dynamics simulation at given temperature. We also

found that stiffer materials can sustain larger deformations than softer materials at the same temperature.

CHAPTER 6

THERMO-MECHANICAL COUPLING

6.1 Introduction

In numerical modeling and simulation, the temperature-related homogenization technique can help to evaluate stress at a local material point if the temperature profile is prescribed. However, material failure is always related to bond breaking at the nanoscale, in which the released energy results in temperature increase in the surrounding material during formation and propagation of cracks. Therefore, a thermo-mechanical model must be developed via coupling the energy equation with the momentum equations in the nanoscale continuum approximation. In this chapter, we couple the thermal diffusion equation in the nanoscale meshfree particle method [72, 73]. The temperature profile is updated via solving discrete equations of thermal flow. Since locally thermal dynamic equilibrium is assumed, the TCB rule is still valid for calculating stresses for solving equations of motion. If crack nucleates and propagates, the released energy due to bond breaking at the nanoscale will be used to calculate the temperature increment in the continuum approximation.

6.2 Thermo-mechanical Coupling

To develop a thermo-mechanical coupling model in nanoscale continuum simulations, the energy equation should be considered as well as the temperature-related homogenization techniques. When assuming Fourier's law for heat conduction, the energy equation is

$$\rho c\dot{T} = \sigma_{ij} v_{i,j} + k\nabla^2 T + S \tag{6.1}$$

where ρ is the density, c is the specific heat, T is the temperature, σ is the stress, v is the velocity, and k is the conductivity. If no internal heat source, S, exists and all deformations are reversible, the energy equation is rewritten as the macroscopic diffusion model for temperature profile.

In our research, we mainly focus on nanoscale continuum simulation via the nanoscale meshfree particle method [72, 73] to demonstrate the application of the proposed thermo-mechanical coupling model. In a two-dimensional problem subject to the Lagrangian description, the governing equations include the thermal diffusion equation [74] and the momentum conservation equation.

$$\rho_0 c_v \dot{T} = k\left(\frac{\partial^2 T}{\partial X_1^2} + \frac{\partial^2 T}{\partial X_2^2}\right) \tag{6.2}$$

$$\rho_0 \ddot{u}_i = \frac{\partial P_{ji}}{\partial X_j} + \rho_0 b_i \tag{6.3}$$

where ρ_0 is the initial density, c_v is the specific heat capacity for constant volume, k is the thermal conductivity, $\mathbf{X}$ is the material (Lagrangian) coordinates, $\mathbf{u}$ is the displacement, $\mathbf{b}$ is the body force per unit mass, and the superposed dots denote material time derivatives. And $\mathbf{P}$ is the nominal stress tensor which can be calculated by TCB rule,

$$\mathbf{P}\left(\mathbf{F},T\right) = \frac{\partial w_H\left(\mathbf{F},T\right)}{\partial \mathbf{F}^{\mathrm{T}}} \tag{6.4}$$

where w_H is the free energy density, and $\mathbf{F}$ is the deformation gradient. The weak forms in the reference configurations, Ω_0, are written as follows via the Galerkin method:

$$\int_{\Omega_0} \delta T \rho_0 \dot{T} d\Omega_0 = -\frac{k}{c_v}\int_{\Omega_0}\left(\frac{\partial\left(\delta T\right)}{\partial X_1}\frac{\partial T}{\partial X_1} + \frac{\partial\left(\delta T\right)}{\partial X_2}\frac{\partial T}{\partial X_2}\right) d\Omega_0 \tag{6.5}$$

$$\int_{\Omega_0} \delta u_i \rho_0 \ddot{u}_i d\Omega_0 = \int_{\Omega_0} \delta u_i \rho_0 b_i d\Omega_0 - \int_{\Omega_0} \frac{\partial (\delta u_i)}{\partial X_j} P_{ij} d\Omega_0 + \int_{\Gamma_0} \delta u_i \bar{t}_i d\Gamma_0 \tag{6.6}$$

where δT and $\delta \mathbf{u}$ are the test functions, and $\bar{\mathbf{t}}$ is the prescribed boundary traction along the boundary, Γ_0. It should be noted that the boundary term in Eq. (6.6) vanished due to the essential boundary condition requirement.

We employ the nanoscale meshfree particle method in this thesis to conduct nanoscale continuum simulations. In meshfree particle methods [40], the fields of temperature and displacements can be approximated as

$$T^h(\mathbf{X},t) = \sum_I \omega_I(\mathbf{X}) T_I(t) \tag{6.7}$$

$$\mathbf{u}^h(\mathbf{X},t) = \sum_I \omega_I(\mathbf{X}) \mathbf{u}_I(t) \tag{6.8}$$

where $\omega_I(\mathbf{X})$ are called Lagrangian kernels since they are functions of the material (Lagrangian) coordinates. The Lagrangian kernel functions can be obtained from the weight function, i.e.,

$$\omega_I(\mathbf{X}) = \omega(\mathbf{X} - \mathbf{X}_I) = \frac{W(\mathbf{X} - \mathbf{X}_I)}{\sum_K W(\mathbf{X} - \mathbf{X}_K)} \tag{6.9}$$

in which a quartic spline weight function is used:

$$W(R) = \begin{cases} 1 - 6\left(\frac{R}{R_0}\right)^2 + 8\left(\frac{R}{R_0}\right)^3 - 3\left(\frac{R}{R_0}\right)^4 & R \le R_0 \\ 0 & R > R_0 \end{cases} \tag{6.10}$$

where $R = \|\mathbf{X} - \mathbf{X}_I\|$ and R_0 is the support radius of the influence domain.

Substituting Eqs. (6.7) and (6.8) into the weak forms of Eqs. (6.5) and (6.6), the following discrete equations of thermal flow and motion can be obtained (Appendix E):

$$m_I \dot{T}_I = K_{IJ} T_J \tag{6.11}$$

$$m_I \ddot{u}_{iI} = f_{iI}^{ext} - f_{iI}^{int} \tag{6.12}$$

where $m_I = \rho_0 V_I^0$ and V_I^0 is the volume associated with particle I, K_{IJ} is the conductivity tensor as

$$K_{IJ} = -\frac{k}{c_v} \int_{\Omega_0} \left[\frac{\partial \omega_I(\mathbf{X})}{\partial X_1} \frac{\partial \omega_J(\mathbf{X})}{\partial X_1} + \frac{\partial \omega_I(\mathbf{X})}{\partial X_2} \frac{\partial \omega_J(\mathbf{X})}{\partial X_2} \right] d\Omega_0 \tag{6.13}$$

and f_{iI}^{ext} and f_{iI}^{int} are the external and internal nodal forces, respectively, given by

$$f_{iI}^{ext} = \int_{\Omega_0} \rho_0 \omega_I b_i d\Omega_0 + \int_{\Gamma_0^t} \omega_I \bar{t}_i d\Gamma_0 \tag{6.14}$$

$$f_{iI}^{int} = \int_{\Omega_0} \frac{\partial \omega_I(\mathbf{X})}{\partial X_j} P_{ji} d\Omega_0 \tag{6.15}$$

In the above integrals of Eqs. (6.13-6.15), we utilize the stress point integration scheme because the meshfree particle method with Lagrangian kernels and stress points is a stable numerical method [35, 40]. It should be noted that temperatures might vary at different particles within thermal flow. However, a locally thermodynamic equilibrium is assumed so that the TCB rule is still valid to calculate stresses.

The flow chart of our simulation is as follows:

1) Initialize the problem, including particle generation, boundary/initial condition definition, and material property identification.
2) Solve the equations of thermal flow, Eq. (6.11), and update particle temperatures.
3) Calculate stresses at the positions of particles via the TCB rule, i.e., Eq. (6.4).
4) Solve the equations of motion, Eq. (6.12), and update particle displacements.
5) Go to step (2) if the target time is not reached.

6) Output.

6.3 Nanoscale Crack Propagation

We restudy the problem of crack propagation in a nanoplate with triangular lattices in chapter 4, as shown in Fig. 4.17. But the temperature field is not prescribed in this case. We give only an initial temperature, which is the room temperature of 300K. Then, the temperature profile will be determined via solving Eq. (6.11) during the simulation. The simulated nanoplate consists of 513,922 atoms with the following dimensions: the length of 1600nm and the width of 280nm. Each atom has the mass of 60amu. An edge crack is initiated in the middle of the plate by taking out a number of bonds, and the initial crack length is 20nm. The nanoplate is subject to fracture mode I via prescribed displacements with the strain rate of 1×10^{-8} per fs. In the meshfree particle model, there are 27,200 particles. The crack is modeled defining a line segment internal to the domain. The domains of influence for particles near the crack are truncated whenever they intersect the crack surface so that a particle on one side of the crack will not affect particles on the opposite side of the crack. This technique is called the visibility criterion by Krysl and Belytschko [11].

For simplification, the crack is restricted to propagate along the weak interface by assuming that only weakened bonds can be broken. A Lennard-Jones potential with $\varepsilon = 2.47\text{aJ}$, $l_0 = 1\text{nm}$, and $l_{cutoff} = 2\text{nm}$, is employed for weakened bonds. In the nanoplate except the weak interface, we use a harmonic potential function, $\varphi_h(l) = \frac{1}{2}k(l-l_0)^2$, to describe interatomic interactions between nearest neighbouring atoms. The spring constant in this harmonic potential function is $k = 594.0\text{nN/nm}$. Using

the TCB rule, the nominal stress, $\mathbf{P}$, at a particle, where the deformation gradient is $\mathbf{F}$ and the temperature is T, is calculated as follows based on a unit cell model,

$$\mathbf{P} = \frac{\partial w_C}{\partial \mathbf{F}^{\mathrm{T}}} + \frac{1}{A_0}\left(\frac{\kappa_B T}{2\bar{D}}\frac{\partial \bar{D}}{\partial \mathbf{F}^{\mathrm{T}}}\right) = \frac{\partial w_C}{\partial \mathbf{F}^{\mathrm{T}}} + \frac{\kappa_B T}{\sqrt{3}\bar{D}l_0^2}\frac{\partial \bar{D}}{\partial \mathbf{F}^{\mathrm{T}}} \tag{6.16}$$

It should be noted that both potential density, w_C, and the determinant of the dynamical matrix, $\bar{D}$, could be calculated via the unit cell model.

The thermal coefficients in equations of thermal flow, i.e., Eq. (6.11), are determined via molecular dynamics simulations on a piece of nanoplate (Appendix F). The specific heat capacity, c_v, represents how the system internal energy responds to an isometric change in temperature. We conduct two isometric molecular dynamics simulations with periodic boundary conditions on the testing nanoplate at various temperatures. In each simulation, the internal energy is computed as the time-averaged potential energy. Consequently, the specific heat capacity can be computed as the change of internal energy per unit temperature. The thermal conductivity k is the intensive property of a material that indicates its ability to conduct heat. It is defined as the quantity of heat, Q, transmitted in time t through a thickness L, in a direction normal to a surface of area A, due to a temperature difference ΔT, under steady state conditions and when the heat transfer is dependent only on the temperature gradient. In our simulation, we set a high temperature on one side of the testing nanoplate and a low temperature on the opposite side via the Hoover thermostat [19]. The periodic boundary condition is applied on the other two sides. The heat will transfer from the side with high temperature to the side with low temperature due to the temperature gradient. The total internal energy in the center part of the specimen is measured as a function of time, so that we can

calculate the thermal conductivity. For the simulated nanoplate, the following thermal coefficients are obtained: $c_v = 0.141\mathrm{J}\cdot\mathrm{kg}^{-1}\cdot\mathrm{K}^{-1}$ and $k = 0.76\mathrm{w}\cdot\mathrm{m}^{-1}\cdot\mathrm{K}^{-1}$.

The crack propagation criterion used in our study is similar to the cohesive zone model [58]. Two crack tips are monitored in the cohesive zone model: one is physical tip, a "real" crack tip in physics, and the other is mathematical tip, a fictitious tip ahead of the physical one. The mathematical tip is used to determine the domain of influence in meshfree particle methods via the visibility criterion. Between the mathematical tip and the physical tip in the continuum model, there is a so-called cohesive zone, where the cohesive traction is applied on the two facets of the cohesive zone. The cohesive tractions, $\boldsymbol{\tau}$, are taken as external forces in meshfree particle simulation and are derived via the TCB rule as

$$\boldsymbol{\tau} = \frac{\partial \hat{w}_H\left(\boldsymbol{\Delta}, T\right)}{\partial \boldsymbol{\Delta}} = \varphi'\left(\boldsymbol{\Delta}\right) + \frac{1}{2}\kappa_B T \frac{\varphi'''\left(\boldsymbol{\Delta}\right)}{\varphi''\left(\boldsymbol{\Delta}\right)} \tag{6.17}$$

where φ is the Lennard-Jones potential describing the weak interface, $\boldsymbol{\Delta}$ is the crack opening displacement vector, and $\hat{w}_H\left(\boldsymbol{\Delta}, T\right)$ is the free energy per unit length along the cohesive zone. In meshfree particle methods, the cohesive tractions can be projected into consistent nodal forces [58] without introducing additional degrees of freedom.

At the nanoscale, crack initiation and propagation involve bond breakage. The released potential due to bond breaking turns out to be the kinetic energy. We know that the kinetic energy at the nanoscale relates to the temperature, which is a macroscopic parameter. Consequently, the temperature increases due to the released energy. Since a bond is treated as broken when its deformed bond length exceeds the cutoff distance, the released energy is calculated as the difference between the potential when the bond

length equals the cutoff distance l_{cutoff} and that when the bond length equals the equilibrium length l_0. In our simulation, the distance that the physical crack tip propagates determines the number of breaking bonds along the weak interface. Consequently, the temperature increment is thereafter calculated as follows:

$$\Delta T = \frac{1}{\kappa_B} \frac{\Delta \varphi_{total}}{N} \tag{6.18}$$

where N is the number of atoms associated with the broken bonds and $\Delta \varphi_{total}$ is the total released energy. In nanoscale meshfree particle simulation, the increasing temperature is distributed on the particles around the physical crack tip based on the meshfree particle approximation. The temperatures on those particles will be treated as the discretized essential boundary conditions while solving the equations of thermal flow.

We simulate the crack propagation in the nanoplate subject to fracture mode I. The initial temperature is set as the room temperature of 300K. The evolution of crack propagation speed is shown in Fig. 6.1. We can see that the crack starts to propagate at 0.42ns. Once the crack propagates, some bonds along the weak interface are broken. The released energy results in a temperature increase in the surrounding domain around the crack tip. Furthermore, a temperature increase results in the reduction of cohesive traction in the cohesive zone along the weak interface. Consequently, the crack propagation speed increases gradually. Fig. 6.2 illustrates the temperature contour in the nanoplate at the time of 0.9ns. The temperature concentration occurs around the crack tip, and temperature propagates from the crack tip to the remaining domain of the nanoplate.

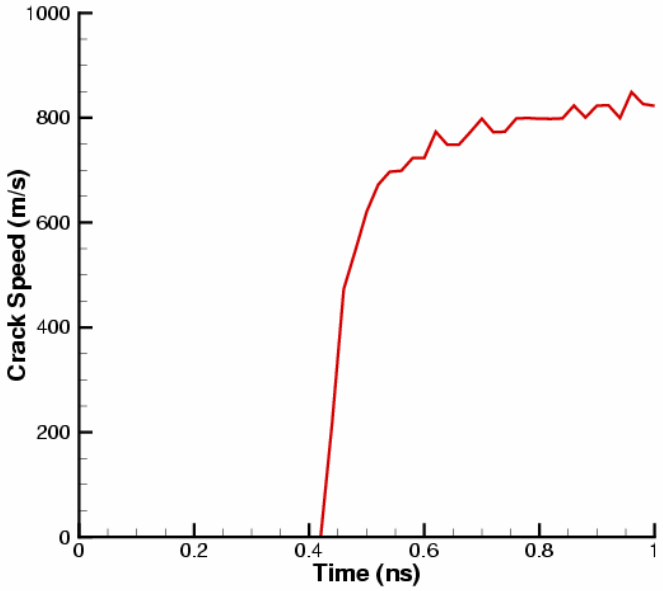

Figure 6.1: Crack speed in a nanoplate with initial temperature of 300K

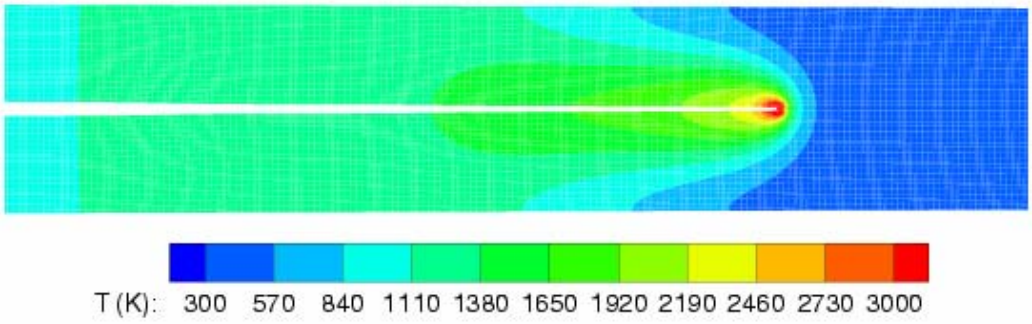

Figure 6.2: Temperature profile of crack propagation at 0.9ns

6.4 Summary and Conclusions

A thermo-mechanical model has been developed via coupling the energy equation with the momentum equations in nanoscale continuum approximations. The temperature-related constitutive relation is represented by TCB rule and the system temperature profile is updated via solving discrete equations of thermal flow. The nanoscale crack propagation is reanalyzed by the thermal-mechanical coupling method with the consideration of the temperature increasing around the crack tip due to the released potential.

CHAPTER 7

NANOTUBE-BASED OSCILLATOR

7.1 Introduction

Since being discovered by Ijimma in 1990 [76], carbon nanotubes hold promise in designing novel nanoscale materials and devices due to carbon nanotubes' unique mechanical and electronic properties [77, 78]. Carbon nanotubes have a high elastic modulus (~ 1TPa) [76], high strength (~100GPa), and low density so they can be used as ideal fibers in nanocomposites [79]. They can also be designed as scanning probe tips, field emission sources or used as other nanoelectronics components, such as molecular wires and diodes. As well, Bachtold and his co-workers [80] demonstrated logic circuits with field-effect transistors based on individual carbon nanotubes. Kinaret *et al*. [81] investigated the operational characteristics of a nanorelay in which a conducting carbon nanotube was placed on a terrace in a silicon substrate. Other carbon nanotube-based devices and machines include nanotweezers [82], nanogears [83], a nanocantilever device [84] and a nanotube motor [85].

A multi-walled carbon nanotube (MWNT) consists of a number of co-axial single-walled nanotubes (SWNTs). Cumings and Zettl [86] realized the ultra-low friction between nanotube walls in nanoscale linear bearings and constant-force nanosprings when demonstrating the controlled and reversible telescopic extension of MWNTs. Consequently, MWNTs have been used to design novel nanoscale devices based on the relative motion of nanotube walls. Lozovik *et al*. [87] proposed to use double-walled nanotubes as nut and bolt pairs, and they found that the relative motion of nanotube walls was controlled by the potential relief of interlayer interaction energy. A nanoswitch [88]

was designed with the assumption that the corrugation of interlayer energy has no significant effects on relative motion between nanotube walls. Nanotube-based oscillators have been of interest to scientists and engineers since Zheng *et al*. [89, 90] designed MWNTs as gigahertz oscillators in 2002. A simple nanotube-based oscillator consists of an inner tube (core) and an outer tube (shell). When the outer tube is fixed, the inner tube can oscillate inside of the outer tube once it is given an initial velocity or an initial extrusion length. The oscillatory frequency may be up to 87GHz based on molecular dynamics simulations [91, 92]. Legoas and his co-workers [92] also pointed out that stable oscillators are only possible when the interlayer distances between the outer and inner tubes are of ~0.34nm, which equals the interlayer distance of regular MWNTs. Unlike other nanotube-based machines, energy dissipation plays a key role and needs to be considered when designing a stable nano-oscillator. Xiao *et al*. [8] studied mechanisms of oscillators at finite temperatures via molecular dynamics simulations. They found that oscillators would stop due to the interlayer friction. Tangney *et al*. [93] also studied mechanical energy dissipation in carbon nanotube-based oscillators and found that the interlayer friction strongly depends on the relative velocity of the tubes. In addition, the morphology combination of the tubes was found to have a significant effect on the interlayer friction [94, 95]. Since nanotube-based oscillators are expected to have potential applications, it is crucial to design stable nano-oscillators.

Although molecular dynamics (MD) is a powerful tool in the domain of computational nanotechnology, as we discussed before, it exhibits severe limitations with respect to both length (restricted to $1.0\mu m^3$ volume) and time (restricted to a time step of 1.0fs) scales. MWNTs employed in experimental investigation have always been

composed of more than millions of atoms. Consequently, MD is not suitable to simulate large models for the purpose of analyzing manufacturing feasibility of nanotube-based mechanical systems. Currently, the development of efficient multiscale methods that are capable of addressing large length and time scales has been the subject of intensive research in computational nanotechnology for designing and analyzing novel nanoscale materials and devices. In this chapter, a continuum approach (a hierarchical multiscale method) will be developed to model and simulate nanotube-based oscillators because utilized nanotubes are not subject to large deformation during the oscillation,

7.2 Modeling of Nanotube-based Oscillator

7.2.1 Single-walled Nanotubes

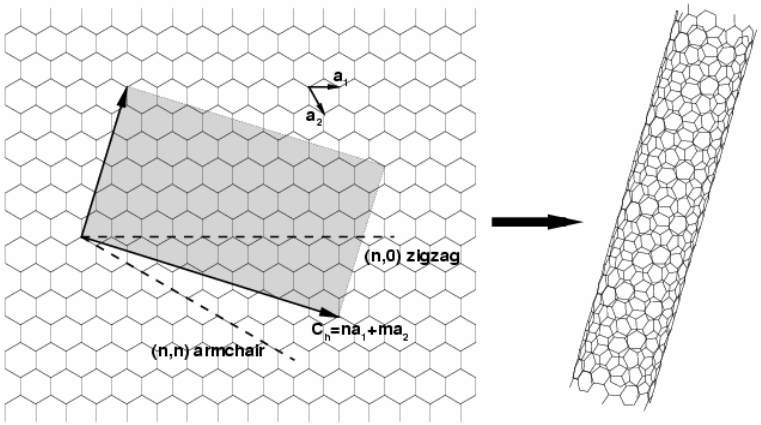

Figure 7.1: Nanotube structure

Most SWNTs have a diameter of close to several nanometers, with a tube length that can be many thousands of times longer. The structure of a SWNT (without cap) can be conceptualized by wrapping a one-atom-thick layer of graphite called graphene into a

seamless cylinder as shown in Fig. 7.1. The nanotube structure is uniquely determined by the chiral vector $\mathbf{C}_h$ which spans the circumference of the cylinder when the graphene layer is rolled up into a tube. The chiral vector can be written in the form as $\mathbf{C}_h = n\mathbf{a}_1 + m\mathbf{a}_2$, where $\mathbf{a}_1$ and $\mathbf{a}_2$ are the lattice vectors of the graphene. The pair of integers n and m, written as (n, m), characterizes the nanotube structure [78, 96]. If $m = 0$, the nanotubes are called "zigzag". If $m = n$, the nanotubes are called "armchair". Otherwise, they are called "chiral".

7.2.2 Continuum Model of Single-walled Nanotube

Since the carbon nanotube can be viewed as an appropriate roll-up of a planar graphene sheet, it is convenient to define the undeformed or reference system as the planar crystalline sheet in the continuum model of carbon nanotubes. The continuum object replacing the crystalline monolayer is a curvature surface without thickness. Therefore, the nuclei are assumed to lie on the surface, and the lattice vectors are chords of the surface.

As discussed in previous chapters, the Cauchy-Born hypothesis consists of assuming that the lattice vectors deform as line elements within a homogeneous deformation, $\mathbf{a} = \mathbf{F}\mathbf{A}$, where $\mathbf{a}$ and $\mathbf{A}$ are deformed and undeformed lattice vectors respectively. $\mathbf{F}$ is the deformation gradient which maps “infinitesimal” tangential material vectors of the undeformed body into “infinitesimal” tangential material vectors of the deformed body. However, the lattice vectors $\mathbf{a}$ and $\mathbf{A}$, each of which connects two atomic positions, are physical entities with finite length. Consequently, Cauchy-Born rule holds exactly, at least locally, only when the “infinitesimal” material vector is equivalent to the lattice vector, which means the deformation is homogeneous.

Arroyo and Belytschko [27] introduced a so-called “exponential Cauchy-Born rule” (ECB rule) to overcome the difficulties of conventional Cauchy-Born rule in approximating curved membranes. The exponential mapping, which maps the lattice vector precisely from the reference to the current configurations, is approximated locally via the ECB rule based on the stretch and curvature of the membrane.

In studying mechanisms of nanotube-based co-axial oscillators, we are mainly interested in the longitudinal motion of the carbon nanotube. We assume that the nanotube is deformed uniformly in the radial direction so that the out-of-plane motion can be neglected. Consequently, the Cauchy-Born rule is still appropriate as a homogenization technique in the continuum model of carbon nanotubes. In this case, the lattice vectors are approximated in the tangent plane at the material point.

Since only the developable surface with zero Gaussian curvature can be mapped to a planar body, the cap of a nanotube, which is a semi sphere, can not be modeled via our continuum approach. However, the need to represent this kind of surface can be covered easily by splitting it into pieces that can be represented as approximately developable patches, and by gluing them together by continuity boundary conditions, which are easily accommodated by the Lagrange multiplier technique [97].

7.2.3 Meshfree Particle Approximation

Since we ignore the out-of-plane motion of the nanotube, the atoms are only allowed to move on the surface of the nanotube. Consequently, each atom has only two degrees of freedom. It is natural to use the Cartesian components on the planar graphene in $\mathbb{R}^2$ to express the atom coordinates in $\mathbb{R}^3$. If we denote $\mathbf{x}_t$ and $\mathbf{x}_g$ as the Cartesian

components of the nanotube and graphene respectively, and R as the radius of the nanotube, the mapping can be written as

$$\begin{aligned} &\varphi : \mathbb{R}^2 \to \mathbb{R}^3 \\ &\quad \mathbf{x}_{\mathrm{g}} \mapsto \mathbf{x}_{\mathrm{t}} = \varphi\left(\mathbf{x}_{\mathrm{g}}\right) \end{aligned} \tag{7.1}$$

Or,

$$\begin{aligned} x_{\mathrm{t1}} &= R\cos\left(\frac{x_{\mathrm{g1}}}{R}\right) \\ x_{\mathrm{t2}} &= R\sin\left(\frac{x_{\mathrm{g1}}}{R}\right) \\ x_{\mathrm{t3}} &= x_{\mathrm{g2}} \end{aligned} \tag{7.2}$$

In the meshfree particle method, we define $\mathbf{x}_{\mathrm{g}} \in \mathbb{R}^2$ as the current configuration and the undeformed planar graphene $\mathbf{X} \in \mathbb{R}^2$ as the reference configuration. The deformation gradient is then defined by

$$\mathbf{F} = \frac{\partial \mathbf{x}_{\mathrm{g}}}{\partial \mathbf{X}} \tag{7.3}$$

which is a 2×2 matrix. Using the Cauchy-Born rule, the nominal stress in $\mathbb{R}^2$ can be computed as

$$\mathbf{P}\left(\mathbf{F}\right) = \frac{\partial w_C\left(\mathbf{F}\right)}{\partial \mathbf{F}^{\mathrm{T}}} \tag{7.4}$$

where w_C is the strain energy density. Therefore the internal force in $\mathbb{R}^2$ is then

$$f_{\mathrm{g}iI}^{int} = \int_{\Omega_0} \frac{\partial \omega_I(\mathbf{X})}{\partial X_j} P_{ji}\, d\Omega_0 \tag{7.5}$$

where $\omega_I(\mathbf{X})$ is the meshfree kernel function. Then, we map the internal force onto the nanotube in $\mathbb{R}^3$, where

$$f_{iI}^{int} = \varphi\left(f_{giI}^{int} \right) \tag{7.6}$$

The equations of motion in $\square^3$ then become

$$m_I \ddot{u}_{iI} = f_{iI}^{ext} - f_{iI}^{int} \tag{7.7}$$

where m_I and f_{iI}^{ext} are the mass and the external force of particle I, respectively.

7.2.4 Non-bonded Interlayer Interaction

In the nanotube-based oscillator, the external force applied on the inner nanotube is primarily due to the van der Waals [98] interlayer interaction. The van der Waals forces are induced due to non-bonded interatomic interactions. Although a SWNT or single layer of a MWNT can be modeled using the continuum approximation via the nanoscale meshfree particle method we developed before, the continuum approach to van der Waals interaction remains an issue. In the meshfree particle method-based continuum model, the key issue becomes how to map the van der Waals interaction between two groups of atoms to the interaction between two particles.

The general form of the non-bonded potential of the atomistic system can be written as

$$E_{nb} = \sum_i \sum_{j>i,\, j\notin B_i} V_{nb}\left(r_{ij}\right) = \frac{1}{2}\sum_i \sum_{j\notin B_i} V_{nb}\left(r_{ij}\right) \tag{7.8}$$

where V_{nb} is the non-bonded potential, r_{ij} is the distance between atom i and j, and B_i is the set of atoms non-bonded interacting with atom i. In our study, the main non-bonded interactions in the nanotube-based oscillator are between the atoms in the outer tube and the atoms in the inner tube. We neglect non-bonded interactions between the

atoms in the same tube. Therefore, the non-bonded energy in the nanotube-based oscillator system is

$$E_{nb} = \sum_{i \in A_O} \sum_{j \in A_I} V_{nb}\left(r_{ij}\right) \tag{7.9}$$

where A_O is the set of atoms in the outer tube and A_I is the set of atoms in the inner tube. The Lennard-Jones 6-12 potential has been adopted here to describe the van der Waals interaction,

$$V_{nb}\left(r\right) = A\left[\frac{1}{2}\frac{y_0^6}{r^{12}} - \frac{1}{r^6}\right] \tag{7.10}$$

where $A = 2.43 \times 10^{-24}\,\mathrm{J \cdot nm^6}$ and $y_0 = 0.3834\mathrm{nm}$ [8, 99]. The interlayer equilibrium distance in a MWNT is $0.34\mathrm{nm}$, which results in the minimum van der Waals energy. This distance matches the thickness of a graphene sheet, and it also satisfies the criterion proposed by Legoas *et al*. [92] for stable nanotube-based oscillators.

To calculate the non-bonded energy in the continuum level, we choose two representative cells of area S_0 each containing n nuclei ($n = 2$ for graphene). The continuum-level van der Waals energy density is

$$\varphi_{nb}\left(d\right) = \left(\frac{n}{S_0}\right)^2 V_{nb}\left(d\right) \tag{7.11}$$

where d is the distance between the centers of those two considered cells. Then, the total continuum-level non-bonded energy is calculated as

$$\Phi_{nb} = \int_{\Omega_O} \int_{\Omega_I} \varphi_{nb}\left(\left\|\mathbf{x}_O - \mathbf{x}_I\right\|\right) \mathrm{d}\Omega_O \mathrm{d}\Omega_I \tag{7.12}$$

where Ω_O and Ω_I are the deformed configuration of outer and inner tube respectively.

Eq. (7.12) can be integrated using the nodal or stress point integration schemes via the meshfree particle method. As a difference from the bonded interatomic interaction, the non-bonded interatomic interaction is determined by the van der Waals cut-off distance which limits the area associated to each particle in the continuum model.

7.2.5 Reduced Model of Nanotube-based Oscillator

Basically, the motion of the nanotube-based oscillator is composed of rigid body translation and deformation of the inner tube. However, since there is only longitude deformation induced on the inner tube (no bending and twisting) and the van der Waals interaction is significantly weaker than the bonded interatomic interaction, the rigid body translation of the inner tube is the dominant motion of the nanotube-based oscillator. Therefore, it is an alternative to reduce the computation model via only considering the rigid body motion of the inner tube and neglecting its deformation. Then the equation of motion is

$$M\ddot{u} = F^{ext} \tag{7.13}$$

where M is the total mass of the inner tube, u is the center-of-mass displacement in the outer-tube-center coordinate system (separation distance), and F^{ext} is the total external force applied on the inner tube due to the van der Waals interaction.

Even in this reduced rigid model of the nanotube-based oscillator, we still need to discretize the CNT into particles since the van der Waals interaction is approximated as interaction between particles. As well, the accuracy of the model depends on the number of particles that is used in the computer simulation. In this chapter, this reduced model is also called the rigid meshfree particle (MP) model while the original MP model is called the deformable MP model.

7.2.6 Verification

We study the oscillation mechanism of a (10, 10)/(5, 5) nanotube-based oscillator which is illustrated in Fig. 7.2 to verify the proposed meshfree particle model via comparing with molecular dynamics simulations. We first assume that the system is isolated so that there is no heat exchange between the oscillator and its surrounding. The outer tube is 3.7nm long, and it is an open-ended (10, 10) armchair tube containing 620 atoms. The inner tube is 2.5nm long, and it is a capped (5, 5) armchair tube containing 260 atoms. In the meshfree particle model, the outer tube surface is discretized with 320 particles following a 15×20 regular background mesh. For the inner tube, a 10×10 background mesh is utilized to discretize the tube cylinder and a 3×10 mesh for the caps. Consequently, the continuum model of the inner tube has totally 152 particles. The distance between two tubes in the radial direction is 0.34nm so that the system satisfies the stability criterion proposed by Legoas *et al*. [92]. In our simulations, the outer tube is fixed and the inner tube is free and deformable in the system. The initial extrusion of the inner tube is half of the inner tube length. When the inner tube is released without any initial velocity, the interlayer force, due to the van der Waals energy between the tubes, will drive the inner tube to move towards the center of the outer tube. The inner tube will be accelerated until the interlayer potential reaches the minimum. The center-of-mass velocity of the inner tube will start to decrease when the interlayer potential increases. Once the center-of-mass velocity of the inner tube becomes zero, the separation reaches the maximum. Then the interlayer force tends to drive the inner tube backwards to the center of the outer tube.

It is assumed that the atoms on the inner tube only move along the cylinder surface without out-of-plane motion. We also assume that the bond lengths between atoms could be approximated by the arc length on the cylinder surface between the positions of the atoms. Therefore the motion and deformation of the inner tube could be modeled by the meshfree particle method using the traditional Cauchy-Born rule. It should be noted that the caps of the inner tube are modeled as rigid surfaces since the surface of the sphere is undevelopable. All the mass and interlayer forces on the caps are uniformly distributed to the particles on the tube cylinder, and the motion of the caps is approximated by the center-of-mass motion of the tube cylinder.

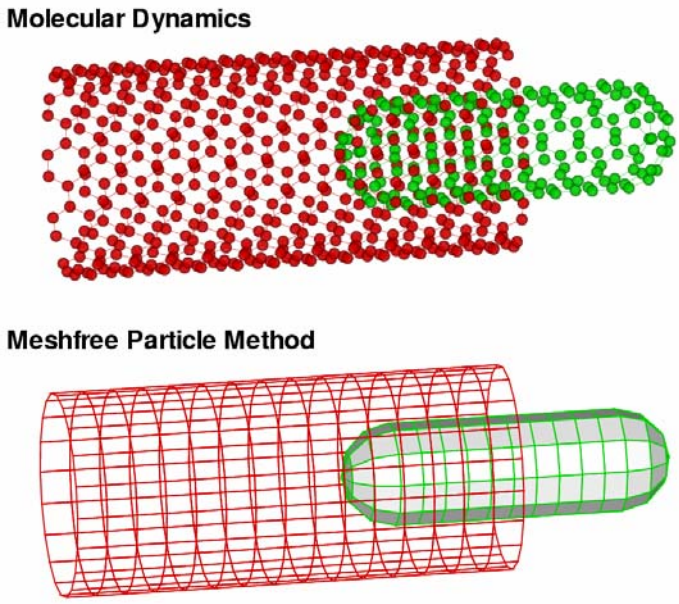

Figure 7.2: MD and MP models of a (10, 10)/(5, 5) nanotube-based oscillator

Fig. 7.3 shows the separation distance evolution of the system obtained from the meshfree particle method and compared with the molecular dynamics result. It can be

seen that the inner tube travels back and forth stably in the outer tube tunnel. Since there is no friction and other energy dissipation, the oscillator maintains constant amplitude, and the oscillatory frequency is around 55GHz which agrees to what Xiao et al. [8] obtained via molecular dynamics simulations. The relative velocities, which are the particle velocities with respect to the local coordinate system at mass center of the inner tube, at different times, are shown in Fig. 7.4. We can see that several shock waves induce in the inner tube during its oscillation. Those shock waves propagate back and forth between the ends of the inner tube and interact with each other. It should be noted that the relative velocities are very small comparing with the velocity of the center-of-mass of the inner tube. As well, the shock wave speeds are very high due to the high stiffness of the nanotube. Consequently, the inner tube behaves like a rigid body. Fig. 7.5 gives the comparison between the deformable and rigid MP models. It is seen that rigid model also gives us a good approximation.

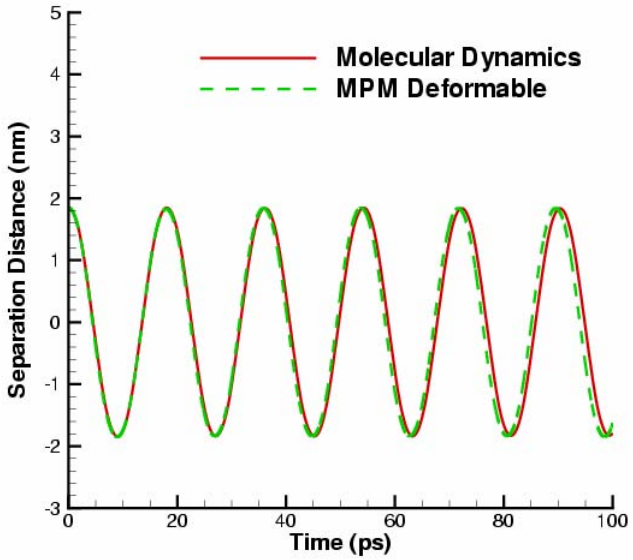

Figure 7.3: Comparison of separation distance evolutions between MD and the deformable MP model

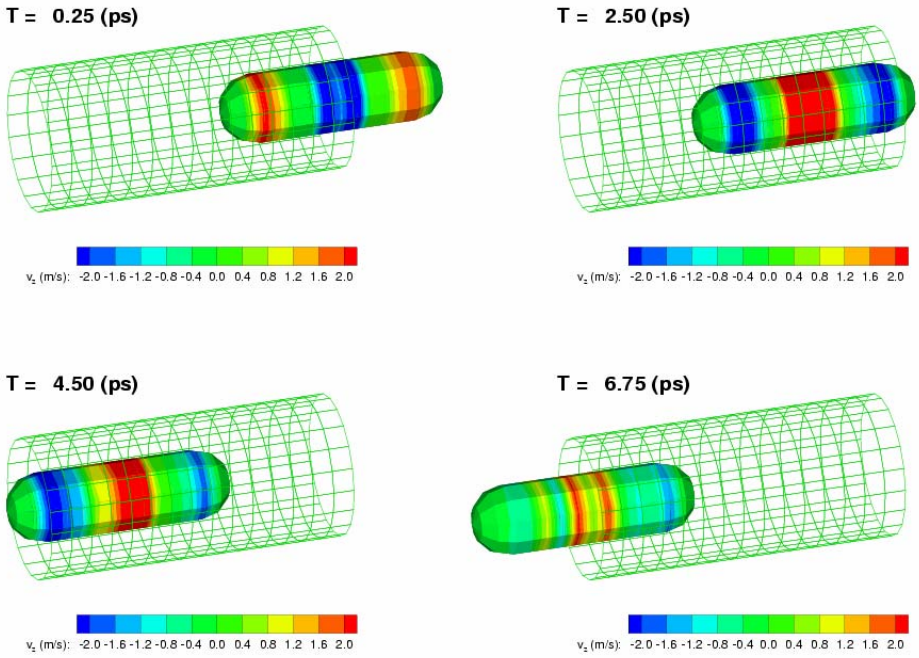

Figure 7.4: Relative velocity contours at different times

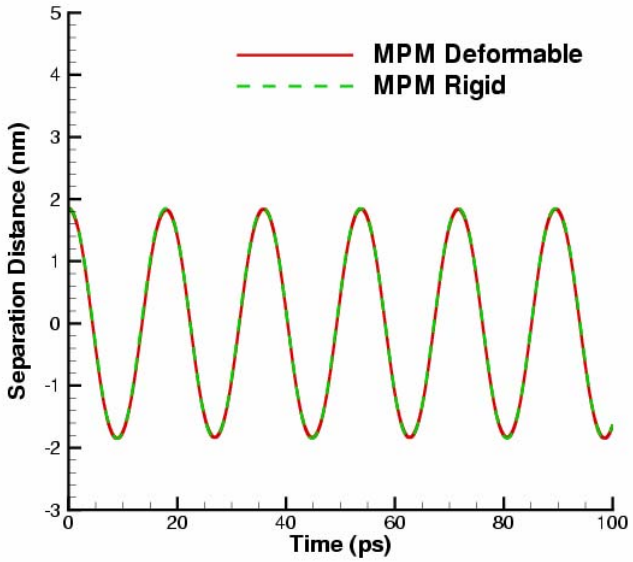

Figure 7.5: Comparison of separation distance evolutions between the deformable and rigid MP models

Next we further consider the interlayer friction and compare it with the MD simulation done by Xiao *et al*. [8]. In this example, the outer tube is a 3.6-nm-long open-ended (10, 10) armchair tube containing 600 atoms while the inner tube is a 2.2-nm-long capped (5, 5) armchair tube containing 180 atoms. In the MP model, there are 380 particles for the outer tube and 152 particles for the inner tube. The initial configuration of the MP model and the corresponding MD model are shown in Fig. 7.6.

The effective interlayer friction in the MD system at certain time can be calculated based on the following equation [95]:

$$F_{\text{eff}} = \frac{1}{4\xi_{\max} f}\frac{dE_{\text{pot}}}{dt} \tag{7.14}$$

where $\xi_{\max}$ is the oscillator amplitude of the nanotube-based oscillator, f is the oscillator frequency, and $\frac{dE_{\text{pot}}}{dt}$ is the potential energy dissipation rate. From the MD simulation, the effective interlayer friction is calculated to be 0.025pN per atom. We applied this interlayer friction as an external force in the continuum model. Fig. 7.7 shows the separation distance as a function of time and compared it with the result from MD simulation. We can see they are in good agreement.

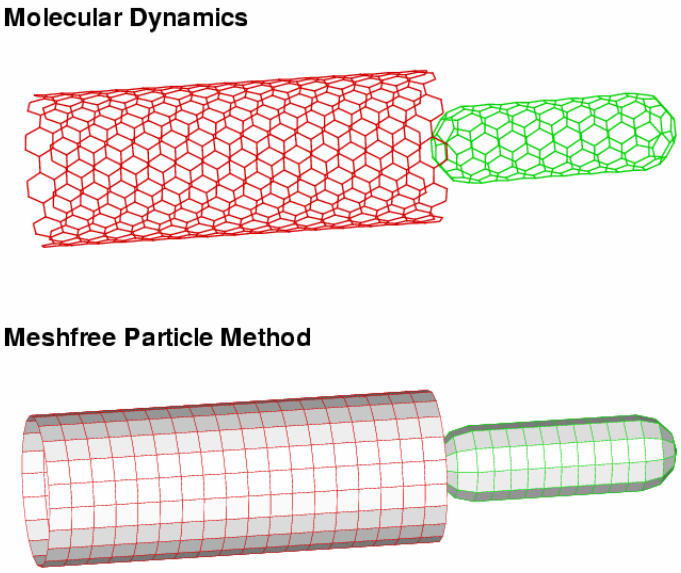

Figure 7.6: Initial configurations of a (10, 10)/(5, 5) nanotube-based oscillator

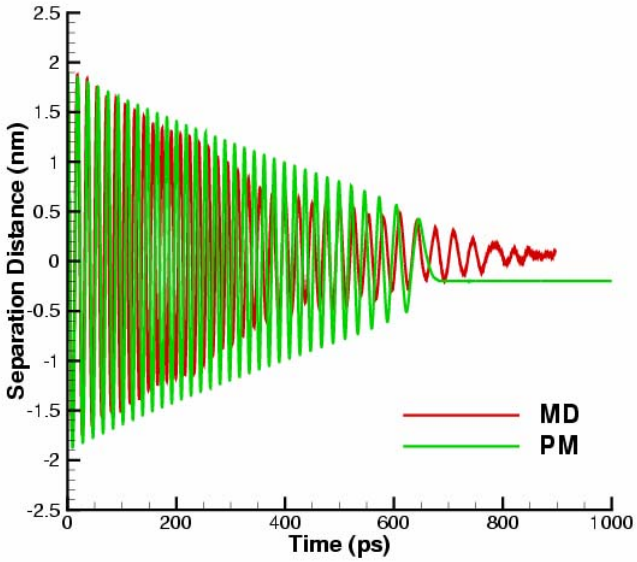

Figure 7.7: Comparison of separation distance between MD and MP simulations

7.2.7 Frequencies of Nanotube-based Oscillator

We employ (10, 10) carbon nanotubes with various lengths as the outer tube to study its length effects on the oscillation mechanism of (10, 10)/(5, 5) nanotube-based oscillators. In the following simulations, we maintain the length of the inner tube to be 2.2nm and the initial extrusion to be half of the inner tube length, 1.1nm. Due to the interlayer van der Waals force, the inner tube is accelerated at the beginning release. The accelerating distance could be estimated as $L_{\text{accl}} = L_{\text{extru}} = L_{\text{inner}} / 2 = 1.1\text{nm}$, through which the center-of-mass velocity of the inner tube increases from zero to a constant, $V_{\max}$. For simplification, we assume the mean interlayer force applied on the inner tube remain constant when the inner tube travels through the accelerating distance so that the elapsed time can be approximately by $t_{\text{accl}} = 2L_{\text{accl}} / V_{\max}$. It is reasonable especially when the inner

tube is long enough since the nonlinear force only occurs when the inner tube end is close to the outer tube end. The acceleration can be calculated from the mean interlayer force and the mass of the inner tube. Here, they are $F_{\text{vdw}} = 0.6\text{nN}$ and $m_0 = 3.4\times10^{-24}\,\text{kg}$. So, the maximum center-of-mass velocity is $V_{\max} = \sqrt{2aL_{\text{accl}}} \approx 623\text{m/s}$. Therefore, the oscillatory frequency can be estimated once the length of the outer tube is given through the following formula

$$f = \frac{1}{2\left(2t_{\text{accl}} + \dfrac{L_{\text{outer}} - 2L_{\text{accl}}}{V_{\max}}\right)} = \frac{V_{\max}}{2\left(L_{\text{outer}} + L_{\text{inner}}\right)} \tag{7.15}$$

Fig. 7.8 illustrates the effect of the length of the outer tube on the nano-oscillator frequency. The oscillatory frequency can be as high as 72GHz when length of the outer tube equals that of the inner tube, which was also predicted by Xiao *et al*. [8]. It also shows the frequencies from MP and MD simulations. They agree with the estimation very well.

Next we investigate the length effects on the oscillation mechanism from the inner tube. We employ (5, 5) carbon nanotube with various length as the inner tube of the (10, 10)/(5, 5) nanotube-based oscillators and maintain the length of the outer tube to be 25nm. The initial extrusion is still the half of the inner tube length. The mean interlayer force applied on the inner tube is still 0.6nN, but the mass of the inner tube and the accelerating distance vary with the length of the inner tube. However, since $L_{\text{accl}} \propto L_{\text{inner}}$ and $a \propto 1/L_{\text{inner}}$, the maximum center-of-mass velocity is still a constant around 623m/s. Therefore, the oscillatory frequency also can be predicted by Eq. (7.15).

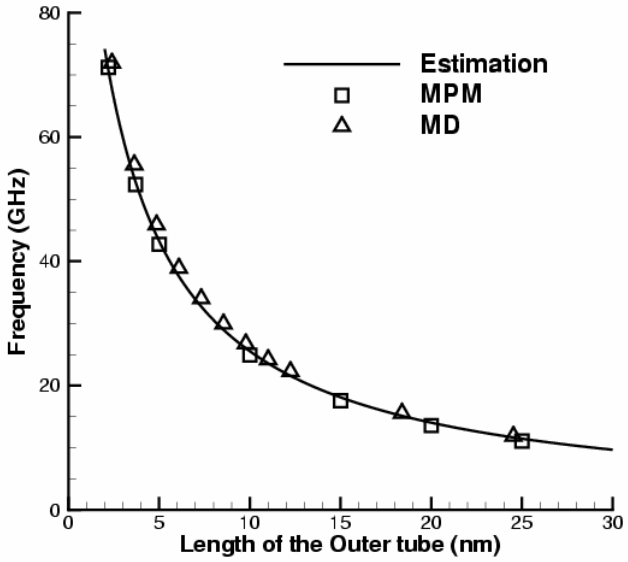

Figure 7.8: Frequencies of the nanotube-based oscillators with different outer tube lengths

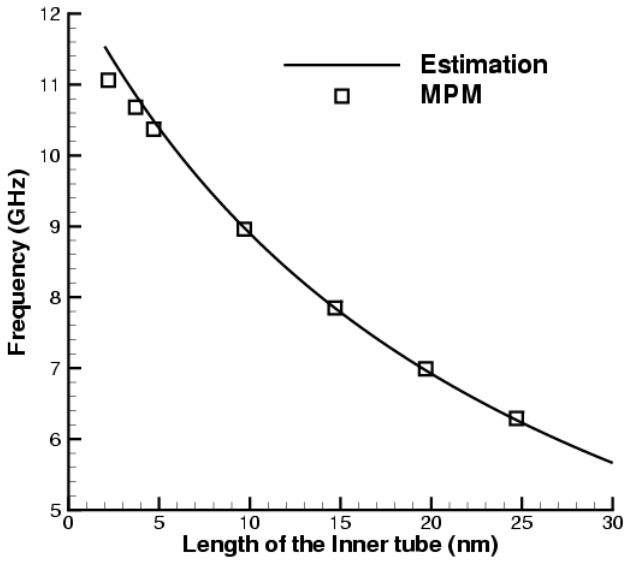

Figure 7.9: Frequencies of the nanotube-based oscillators with different inner tube lengths

Fig. 7.9 shows the comparison of the frequencies of different inner tube length from both Eq. (7.15) and MP simulations. The results agree with each other especially when we have a large inner tube length. That's because the non-constant interlayer force is negligible for a long inner tube. It should be noted that Eq. (7.15) worked for various cases as long as the initial extrusion was half of the inner tube length and the interlayer distance between outer and inner tube was around 0.34nm. However, it is easy to modify Eq. (7.15) by the same methodology for different extrusion lengths.

7.3 NEMS Design for CNT-based Nano Devices

7.3.1 Motivation

Due to their extraordinary mechanical, thermal and electrical properties, carbon nanotubes (CNTs) have attracted tremendous interest from fundamental science and technological perspectives. Nanotube-based electronics is one of the main potential uses of carbon nanotubes. The flexibility of nanoscale design and availability of both semiconducting and metallic nanotubes enable a wide variety of device configurations [78, 96, 100, 101]. These devices include metallic wires, field-effect transistors, electromechanical sensors and displays [96]. Another exciting application of the CNT is the development of the CNT-based high-density data storage devices [96]. This new type of memory can have up to 100-times the storage density of existing random access memories (RAMs) by taking the advantage of the unique electromechanical properties of CNTs.

With the interest to develop the nanotube-based memory cell, we have analyzed the mechanism of the nanotube-based oscillator in the previous sections. An example of a

(5, 5)/(10, 10) nanotube-based oscillator illustrates the evolution of the separation distance while the inner tube oscillates inside the outer tube. The calculated frequency is 55GHz and is referred to as the natural oscillatory frequency of this particular nano-oscillator. We also showed that the natural oscillatory frequency depends on the structure and the length of nanotubes. However, when an oscillator is subject to a finite temperature as discussed in [8, 94], mechanical energy dissipation will be observed and the oscillation will cease. Such energy dissipation was found to be strongly dependent on the morphology combination of the tubes. MD simulations led to the conclusion that a carbon nanotube itself could not be used as a steady nano-oscillator at finite temperatures. Therefore, to make the steady nanotube-based oscillator capable of functioning at specific temperatures, special treatment needs to be considered in the nanoelectromechanical systems (NEMS) design to overcome the energy dissipation.

7.3.2 NEMS Design for CNT-based Memory Cell

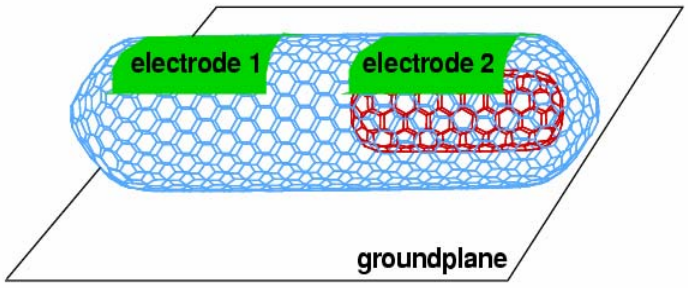

Figure 7.10: A NEMS design for memory cells

Fig. 7.10 illustrates a simple example of the proposed NEMS design. The outer tube is a capped (17, 0) zigzag tube while the inner tube is a capped (5, 5) armchair tube.

It has been known that carbon nanotubes with different chiralities exhibit different electrical properties. It is known that if (m-n)/3 is an integer, the carbon nanotube is metallic, otherwise the tube is semiconducting. In the proposed design, the outer tube is semiconducting while the inner tube can be either metallic or semiconducting. In the example depicted in Fig. 7.10, the (17, 0) nanotube is semiconducting and the (5, 5) nanotube is metallic. The outer tube is positioned on the top of a conducting ground plane. Atomic materials for the conducting electrodes 1 and 2 are deposited on the top of the outer nanotube. In this configuration the inner tube sits in a double-bottom electromagnetic potential well. The depth of the potential well under electrode 1 is proportional to the voltage applied to electrode 1; similarly, the depth of the potential well under electrode 2 is proportional to the voltage applied to electrode 2. The induced quasi-static electromagnetic forces exerted on the inner tube will overcome interlayer friction if the applied voltage is sufficiently large. This large applied voltage is referred to as the WRITE voltage. When a WRITE voltage is applied to the electrode, the inner tube may move due to the induced electromagnetic forces [102, 103]. It is because the electromagnetic force due to the applied WRITE voltage is sufficiently strong to overcome the interlayer friction acting upon the inner nanotube. Consequently, lateral motion of the inner tube will be induced as a result. Here, a capped outer tube is employed because the inner tube can easily escape from an open outer tube due to the induced electromagnetic forces. The capacitance of the NEMS gate can be read by a distinct READ process. A constant-current pulse is applied to one of the electrodes. If the inner CNT is present under that electrode, a relatively large capacitance will be observed, and the time required to charge the electrode will be longer. If the inner tube is

not present under that electrode, a relatively small capacitance will be observed, as will a concomitant fast charging time for the electrode. As a result, the logic state of the NEMS gate can be determined, as schematically shown in Fig. 7.11. It should be noted that all READ voltages are sufficiently small so that the motion of the inner tube will not be influenced. Whether the inner tube is underneath electrode 1 or electrode 2 will result in two different physical states determined by the READ voltage. These two different physical states can be interpreted as Boolean logic states. Therefore, the system can be used as a static random access memory (SRAM) cell.

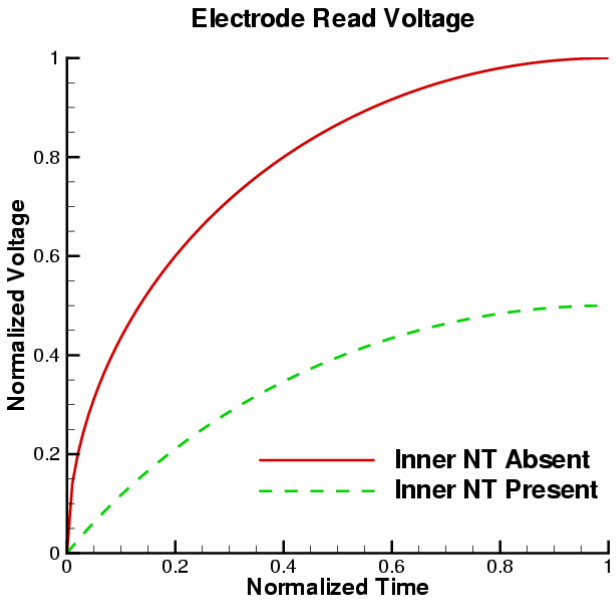

Figure 7.11: Schematic read voltage

7.3.3 Electromechanical Properties of CNT-based Memory Cell

Since the outer carbon nanotube is chosen as semiconducting, its electric property is very similar to that of the insulator. Including two electrodes and the conducting

ground plane, the whole device can be viewed as a two-conductor capacitor with the dielectric spaces between them. The capacitance of the system varies with the presence or absence of the inner carbon nanotube. In other words, the electric energy stored in the system varies with different positions of the inner tube when a constant voltage is applied on the electrode. Consequently, the inner tube will be driven by the induced electromechanical force due to the gradient of the electric energy.

Poisson's equation is the general way to find the electric potential for a given charge distribution [104],

$$\nabla^2\Phi = -\frac{\rho}{\varepsilon_0} \tag{7.16}$$

where Φ is the potential (in volts), ρ is the charge density (in coulombs per cubic meter) and $\varepsilon_0 = 8.854\times10^{-12}\,\text{F/m}$ is the permittivity of free space (in farads per meter). In a region of space where there is no unpaired charge density, we have

$$\rho = 0 \tag{7.17}$$

and the equation for the potential becomes Laplace's equation:

$$\nabla^2\Phi = 0 \tag{7.18}$$

The solution of the Laplace and Poisson equations can be obtained by the numerical methods such as finite differences, finite elements, Fourier transformations, or method of moments [105]. And the electric field at a point is equal to the negative gradient of the electric potential there. In symbols,

$$\mathbf{E} = -\nabla\Phi \tag{7.19}$$

Capacitance is a measure of the amount of electric charge stored (or separated) for a given electric potential. In a capacitor, there are two conducting electrodes which are

insulated from one another. The charge on the electrodes is $+Q$ and $-Q$, and $\Delta\Phi$ represents the potential difference between the electrodes.

$$C = \frac{Q}{\Delta\Phi} \tag{7.20}$$

We can determine Q by a surface integral over the positive conductors, and we find $\Delta\Phi$ from the difference of the potential between the electrodes.

$$C = \frac{\oint_S \mathbf{E} \cdot \varepsilon_0 \mathrm{d}\mathbf{S}}{V_1 - V_0} \tag{7.21}$$

where V_1 and V_0 are the potentials for two electrodes respectively. In our design, the capacitor is made of an electrode of potential V with the ground plane which has the zero potential, so $V_1 = V$, $V_0 = 0$, and the capacitance is further expressed as

$$C = \frac{\oint_S \mathbf{E} \cdot \varepsilon_0 \mathrm{d}\mathbf{S}}{V} \tag{7.22}$$

The energy stored in a capacitor is

$$W = \frac{1}{2} C V^2 \tag{7.23}$$

If the length of the electrode along the longitude direction of the nanotube is sufficiently large compared with the diameter of the outer nanotube, we can assume that the electric field is uniformly distributed along the longitude direction and the fringing regions at the both ends of the electrode are negligible. Therefore, Eq. (7.18) can be simplified as a two-dimensional case. In this chapter, we can consider the following two cases: the capacitor with or without the presence of the inner tube, respectively. For each case, the electric field and the capacitance can be easily calculated by taking the advantage of the two-dimensional model. If the inner tube is partially under the electrode, the system is

effectively the combination of two capacitors in parallel. We denote C_0' and C_1' as the capacitances of unit length capacitor without and with inner tube respectively, and yield the total capacitance of the system,

$$C = \begin{cases} C_1' l_0 & \text{with inner tube} \\ C_0' l + C_1' \left(l_0 - l \right) & \text{with part of inner tube} \\ C_0' l_0 & \text{without inner tube} \end{cases} \tag{7.24}$$

where l_0 is the length of the electrode and l is the length of the inner tube underneath the electrode, which varies with the positions of the inner nanotube, $l = f\left(z\right)$. And the electromstatic force applied on the inner tube can be calculated as

$$F\left(z\right) = \frac{\partial W}{\partial z} = \frac{1}{2} V^2 \frac{\partial C}{\partial z} \tag{7.25}$$

However, if the diameter of the outer nanotube is large and the length of the electrode is short, the fringing regions cannot be neglected. In this case, three-dimensional calculation would be appropriate for this case.

7.3.4 Capacitance Calculation

7.3.4.1 Two-dimensional Capacitance Calculation

The capacitance is the intrinsic property of an electric device. It is a function of the physical dimensions of the system of conductors and the permittivity of the dielectric. Due to the Gauss's law, the calculation of the capacitance should be independent of the potential and the total charge because the ratio of the pontential to the toal charge is constant. Therefore, we can arbitrarily choose the potential on the electrode. Here we assume the electrode has a constant potential of 10V .

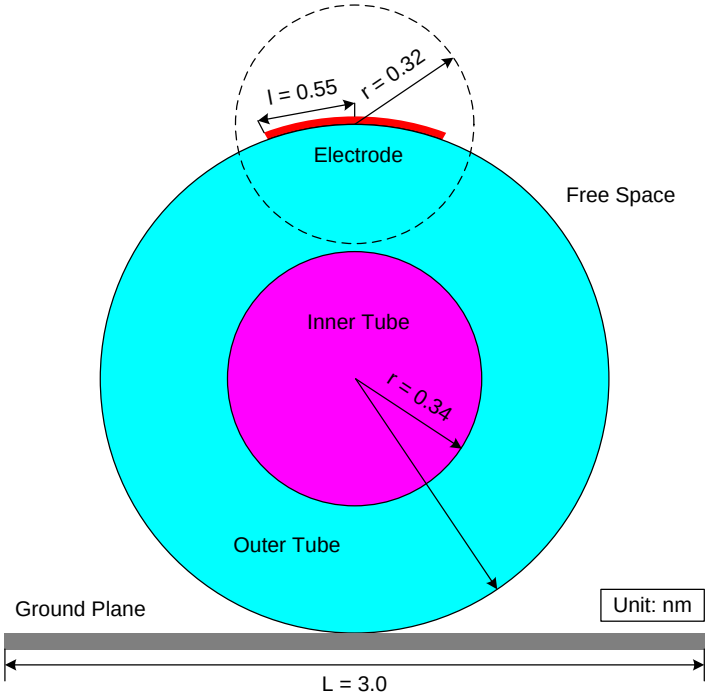

Figure 7.12: Cross-sectional view of the nanotube-based memory cell

Fig. 7.12 schematically shows the cross section of the nanotube-based memory cell. In the considered NEMS, the inner (5, 5) tube has a radius of 0.34nm, and the outer (17,0) has a radius of 0.68nm. It is known that the thickness of graphene is 0.34nm. Therefore, the (5, 5) inner tube is viewed as a solid rod with the radius of 0.34nm, while the (17, 0) outer tube is viewed as a hollow cylinder with the inner radius of 0.34nm and the outer radius of 0.68nm. The outer tube sits on the ground plane and is attached 1.1nm long electrode on the center top. The region between the electrode and the ground plane composes two kinds of dielectrics as indicated in Fig. 7.12. The pink region is free space if the inner tube is absent or CNT if the inner tube is present in the system. The dielectric constant (relative permittivity) of CNT is chosen to be 5.0, which is also used in Crujicic's work [106].

By Gauss's law, the charge induced on a conductor is equal to the flux ending there. The charge calculated from Eq. (7.22) should be independent of the integral path as long as the electrode is included in the region. To perform the line integral (surface integral in 3-D case), we employ a circle (sphere in 3-D case) with the radius 0.32nm at the center top of the outer tube, which is also called "Gaussian surface".

Fig. 7.13, Fig. 7.14, and Fig. 7.15 show the two-dimensional electric potential, electric field, and electric field on the integral path respectively when the inner tube is absent. The calculated capacitance is $1.03\times10^{-19}\text{F}$. Similarly, Fig. 7.16, Fig. 7.17, and Fig. 7.18 show the s electric potential, electric field, and electric field respectively when the inner tube is present. The calculated capacitance is $1.11\times10^{-19}\text{F}$, which is larger than the one when the inner tube is absent.

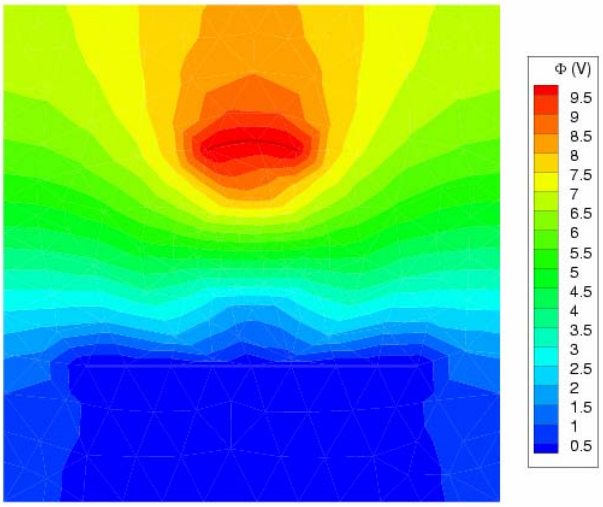

Figure 7.13: 2-D electric potential when the inner tube is absent

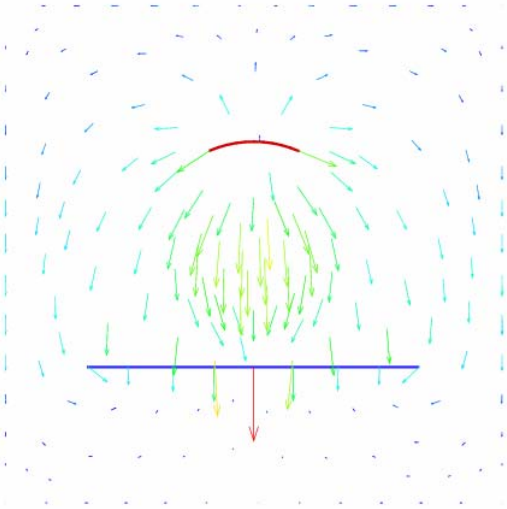

Figure 7.14: 2-D electric field when the inner tube is absent

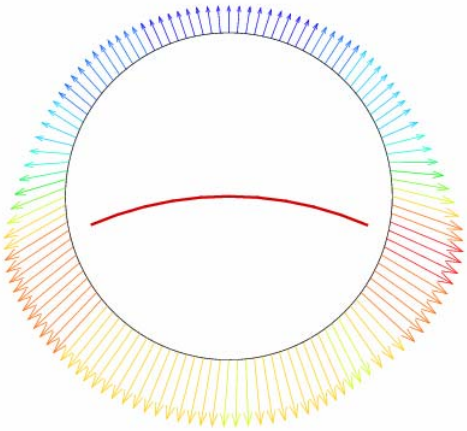

Figure 7.15: 2-D electric field on the integral path when the inner tube is absent

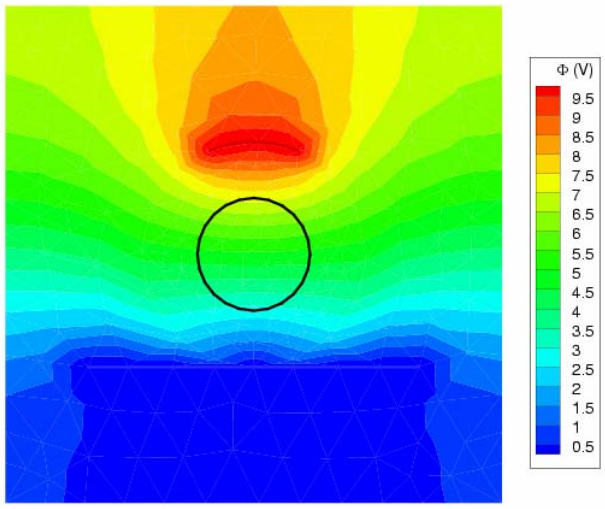

Figure 7.16: 2-D electric potential when the inner tube is present

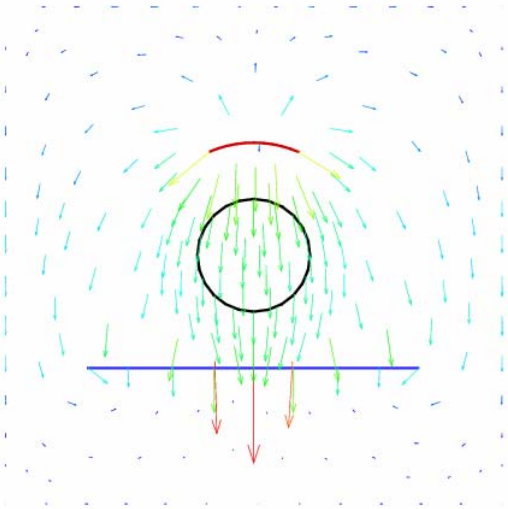

Figure 7.17: 2-D electric field when the inner tube is present

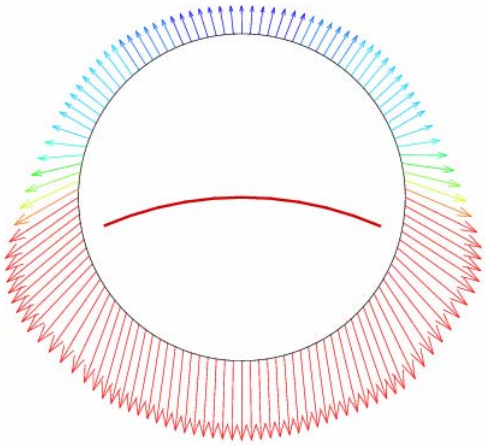

Figure 7.18: 2-D electric field on the integral path when the inner tube is present

7.3.4.2 Three-dimensional Capacitance Calculation

We also calculate the capacitance of the nanotube-based memory cell for different inner tube position by a three-dimensional model. The 7.5-nm-long (17, 0) outer tube has a radius of 0.68nm and sits on the ground plane with the dimensions of $7.5\text{nm} \times 3.0\text{nm}$. The (5, 5) inner tube is 1.6nm long and has a radius of 0.34nm. The electrode attached on the center top of the outer tube is 0.3nm long in the longitude direction and 1.1nm wide along the lateral direction. The CNTs in the model are solid rod and hollow cylinder with a 0.34nm thickness. The dielectric constant of CNT is also 5.0.

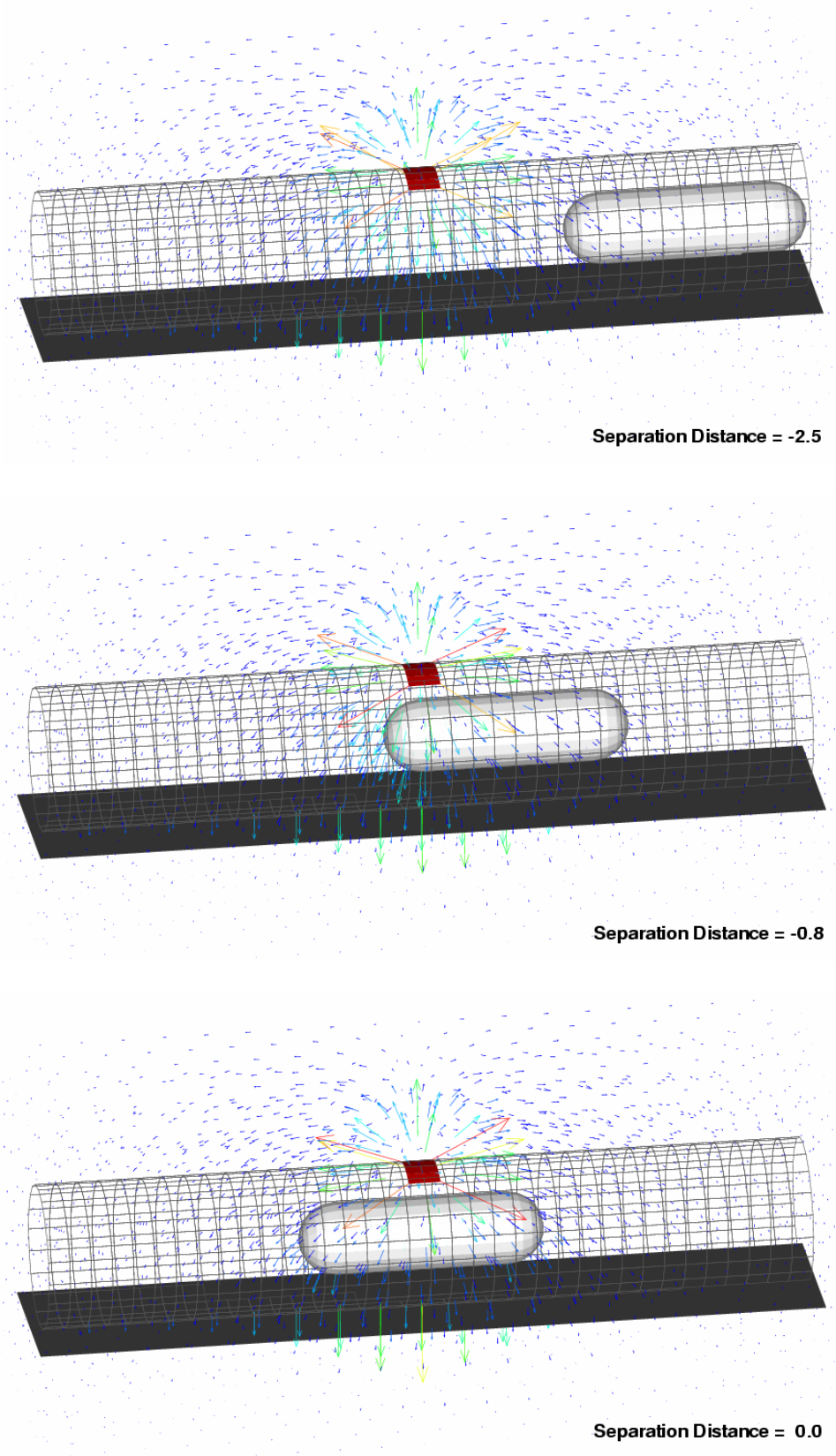

Figure 7.19: 3-D electric field for different inner tube positions

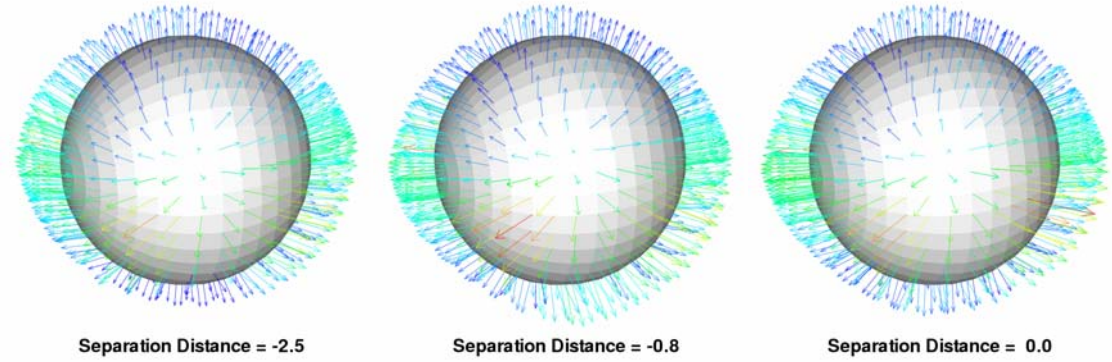

Figure 7.20: 3-D electric field on the integral surface for different inner tube positions

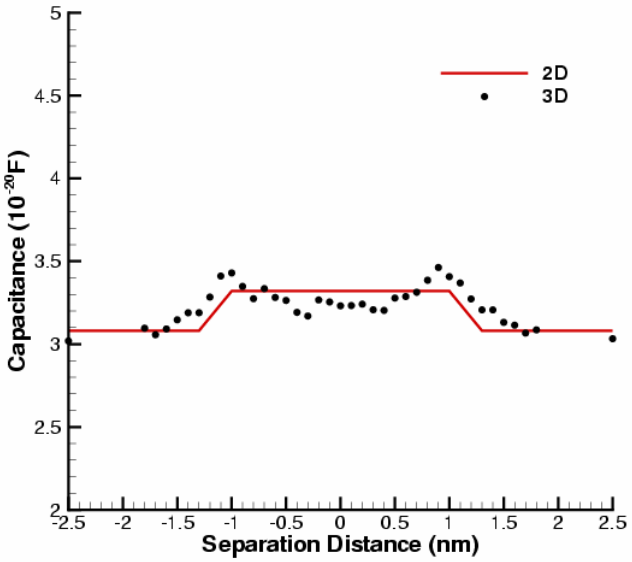

Figure 7.21: Comparison of capacitance from 2-D and 3-D calculations

Fig. 7.19 shows the three-dimensional electric fields when the separation distance is –2.5nm , –0.8nm and 0.0nm . The integral is conducted on the surface of a sphere located in the middle of the electrode. Fig. 7.20 gives the three-dimensional electric field on the integral surface for different inner tube positions. And the comparison of the

capacitance calculated from two-dimensional and three-dimensional model is presented in Fig. 7.21, in which we can conclude that the two-dimensional model is a good approximation.

7.3.5 CNT-based Memory Cell

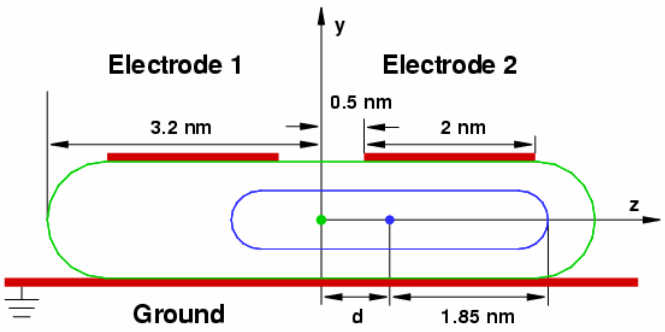

Figure 7.22: Geometry of the nanotube-based memory cell

An example of the proposed nanotube-base memory cell is indicated in Fig. 7.22. The length of (17, 0) outer CNT has the length of 6.4nm , while the (5, 5) inner CNT has the length of 3.7nm . There are 884 particles in the MP model. We attach two 2.0nm long electrodes symmetrically on the top of the outer CNT. Initially, the inner tube is at the center of the outer tube. The voltage applied on the electrodes can not too large otherwise the CNT could start unraveling carbon chains from the exposed edge. Lee *et al*. claimed that the breakdown voltage of the CNT is round 2.0V/Å [107]. Therefore, the CNTs in our design could afford a potential of several hundreds volts to maintain its electrochemical stability. Here we apply 16V constant voltage on the two electrodes alternatively for the time interval of 1ns . The total electromagnetic force applied on the

inner tube is around 1.0nN which is calculated via Eq. (7.10) and the capacitance came from the two-dimensional model.

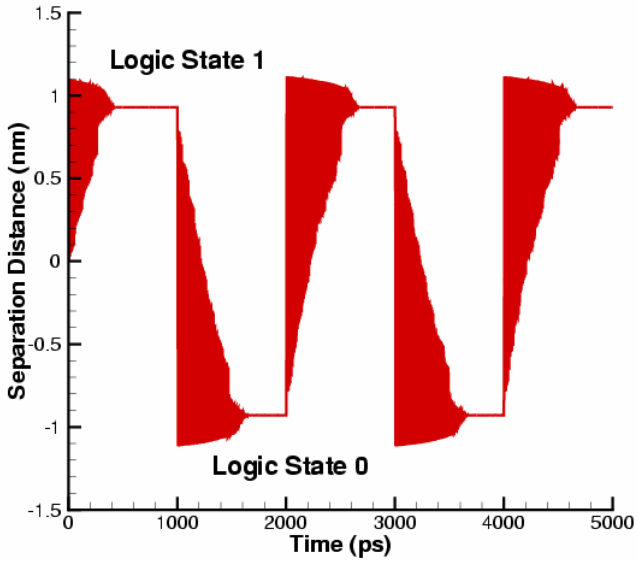

Figure 7.23: Separation distance of the short nanotube-based memory cell in SRAM configuration

Fig. 7.23 shows the separation distance of the nanotube-based memory cell when constant voltage is applied on the electrodes alternatively. After we apply the voltage on electrode 2, the inner tube is stimulated to move due to the induced electromagnetic force. Under electrode 2, the amplitude of the oscillation is getting smaller and smaller due to the interlayer friction and the electromagnetic force. Finally, the inner tube ceases under electrode 2 after about 500ps. When the voltage is shifted to electrode 1, the inner tube moves again and ceases under electrode 1. Such a motion of the inner tube repeats as long as the shifting voltage is applied on the electrodes. When the inner tube is under

electrode 1 or electrode 2, its position can be detected by the READ process and the logic states 0 and 1 are produced. Fig. 7.24 shows the position of the inner tube at different logic state. The red color on the electrode indicates the applied voltage. The frequency of the memory cell depends on the frequency of the voltage shifting, which means the device works as a SRAM. In this case, the frequency of this SRAM is 500MHz. Since it takes 500ps for the inner tube to cease under an electrode, the recommended maximum frequency is 1GHz.

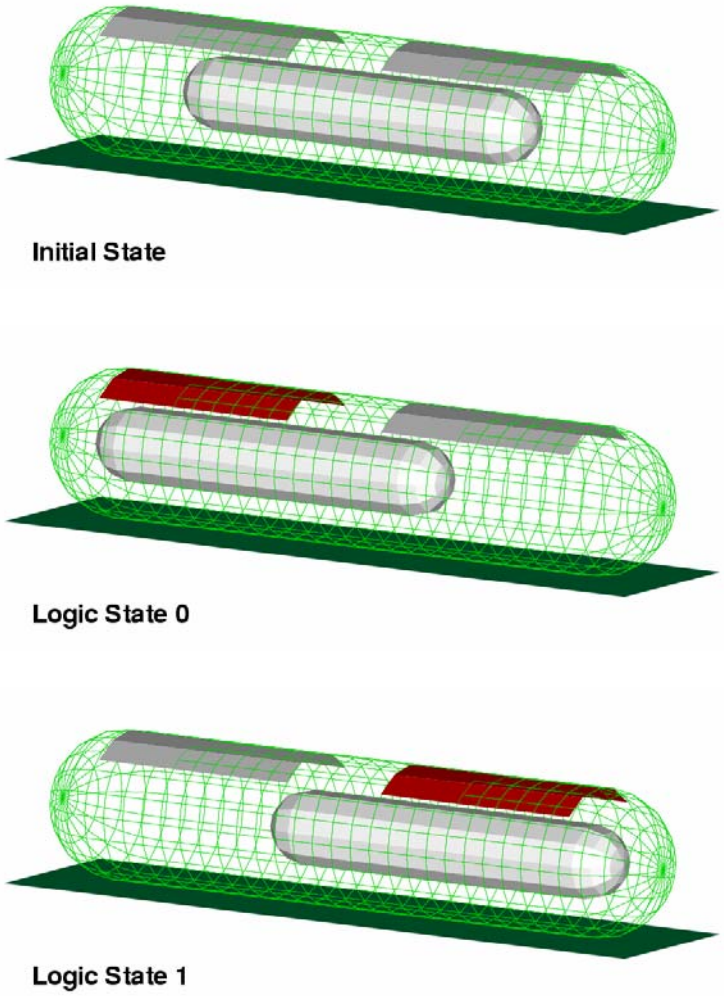

Figure 7.24: Positions of the inner tube at different logic states in SRAM configuration

Next, we consider the same SRAM device with longer CNTs. We maintain the diameter of the CNTs but change the lengths of the outer and inner tube to 32nm and 18nm respectively. The electrodes are elongated to 10nm so that the inner tube can be stimulated at any position. The voltages applied on the electrodes are still 16V but the electromagnetic forces are increased due to the change of electrode lengths. There are 2834 particles in the MP model. Fig. 7.25 shows the separation distance of the nanotube-based memory cell when constant voltage is applied on the electrodes alternatively. It can be seen that we can also obtain different logic states with the frequency around 500MHz. Obviously the maximum frequency of a nanotube-based memory cell depends on lengths of the inner tube, the out tube, and the electrodes.

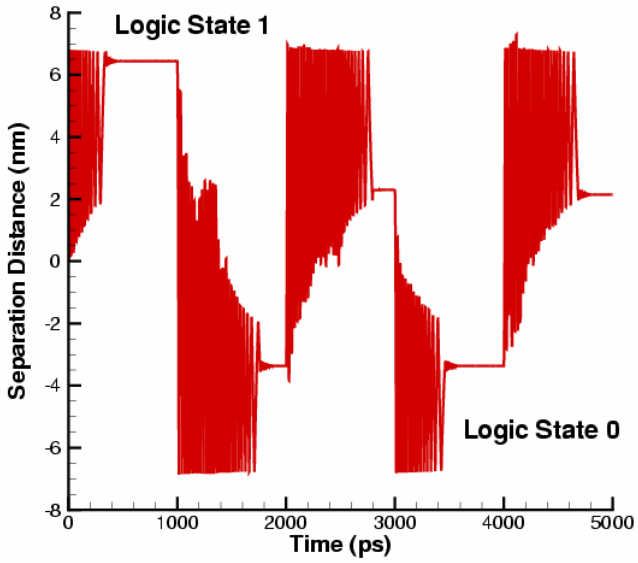

Figure 7.25: Separation distance of the long nanotube-based memory cell in SRAM configuration

It is obvious that the frequency of the proposed NEMS cannot exceed the natural frequency of its embedded nanotube-based oscillator. Since the nanotube-based oscillator is an underdamped system, the proposed design can be extended for application as a dynamic random access memory (DRAM) cell. In this configuration, the oscillator will continue to oscillate at its natural frequency. A WRITE voltage pulse is applied every several oscillation periods to stimulate oscillation of the oscillator. The period of the WRITE voltage pulse should not be larger than natural period of the oscillator so that the induced voltage acts to enhance oscillation from time to time. Consequently, a steady oscillation can be generated.

Fig. 7.26 shows the separation distance of the nanotube-based memory cell in the DRAM configuration. In this case the DRAM still composes of a 32-nm-long (17, 0) outer tube and a 18-nm-long (5, 5) inner tube. Here, we use an open-ended outer tube instead of the capped one. Two 10-nm-long electrodes are attached on the top of the outer tube. Initially, the inner tube is at the position where the separation distance is -4nm and with the velocity of 400m/s. With such an initial condition, the natural oscillating frequency of the oscillator is 6.75GHz. We apply a voltage of 48V at the electrode 2 and last it for 2ps. The inner tube is accelerated but the oscillatory amplitude decreases due to the interlayer friction. After the oscillator oscillates four cycles, we give the same voltage pulse on the electrode 2 to increase the oscillatory amplitude. Then, the inner tube keeps oscillating. Figure 7.26 shows that stable oscillation can be reached for DRAM cells.

Fig. 7.27 gives the periodic voltages applied on the electrode 2, and Fig. 7.28 shows the positions of the inner tube at different logic states in DRAM configuration. It

should be noted that we applied the periodic voltage pulses on the electrode 2 in this case. However, voltage pulses on the electrode 1 or on both electrodes 1 and 2 alternatively can also maintain the oscillation of oscillators.

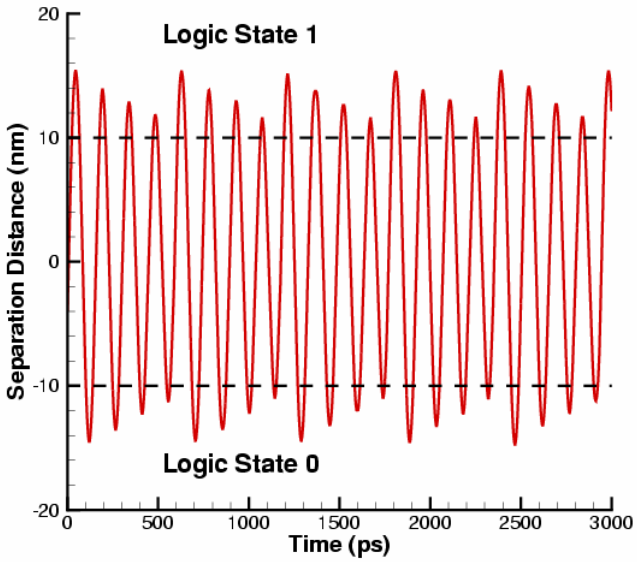

Figure 7.26: Separation distance of the long nanotube-based memory cell in DRAM configuration

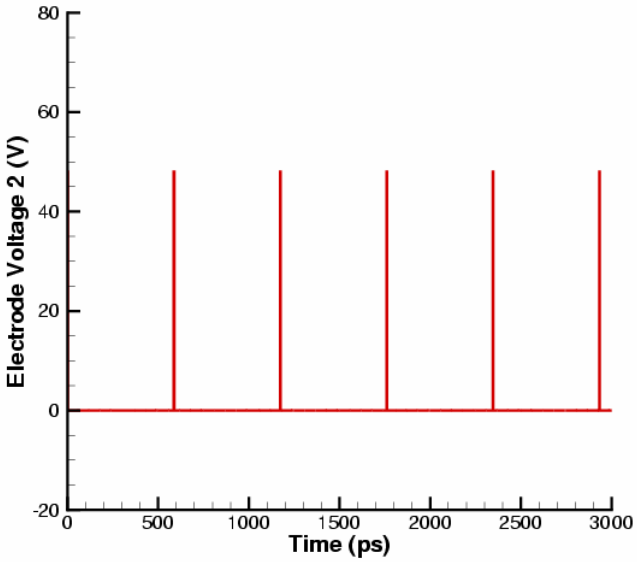

Figure 7.27: Voltage on electrode 2 of the long nanotube-based memory cell in DRAM configuration

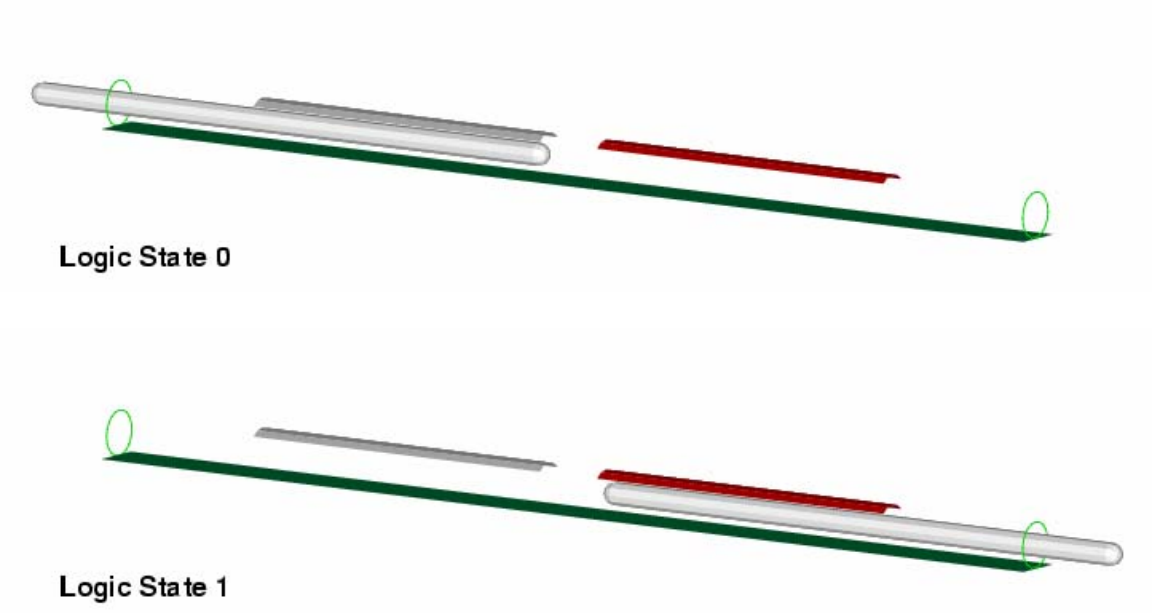

Figure 7.28: Positions of the inner tube at different logic states in DRAM configuration

7.4 Summary and Conclusions

The mechanism of the nanotube-based oscillator has been studied by the nanoscale meshfree particle method. Since the rigid body motion dominates the oscillation of oscillators, the nanoscale meshfree particle model is simplified to calculate interlayer interaction between the outer tube and inner tube. A NEMS design, containing nanotube-based oscillators has been proposed as a memory cell. The electric properties of the nanotube-based memory cell have been analyzed. Numerical analyses demonstrated that the superposed electric field overcomes the interlayer friction in the embedded nanotube-based oscillator so that the steady oscillatory mechanism can be obtained and the representation of the Boolean logic states is possible.

CHAPTER 8

SUMMARY AND FUTURE WORK

8.1 Summary

It has been known that temperature has significant effects on material behaviors at the nanoscale. Although multiscale methods can overcome the limitations of length/time scale that molecular dynamics has, they have difficulties in investigating temperature-dependent physical phenomena because most homogenization techniques have an assumption of zero temperature. A new homogenization technique, the temperature-related Cauchy-Born (TCB) rule, was developed in this thesis with the consideration of the free energy instead of the potential energy. The TCB rule assumes that atoms have locally harmonic motion in addition to homogeneous assumption. When employing the TCB rule in the nanoscale continuum approximation, the first Piola-Kirchhoff stress can be explicitly computed as the first derivative of the Helmholtz free energy density to the deformation gradient. Since the Helmholtz free energy is temperature-dependent, multiscale methods consisting of the TCB rule embedded continuum model can be used to elucidate temperature-related physical phenomena at the nanoscale. Stress analyses of canonical ensembles verify the continuum approximation with the TCB rule by comparing the calculated Cauchy stresses with the outcomes of molecular dynamics simulations. Temperature-related material instability was also studied in this thesis. The von Neumann stability analysis showed that the temperature-dependent intrinsic stability of a crystalline solid could be reflected by TCB rule. Stability analyses of a 1D molecule chain and 2D lattices verified that the stability states from TCB rule are the same as the ones from molecular dynamics simulation at given temperature. We also found that

stiffer materials can sustain larger deformations than softer materials at the same temperature.

A nanoscale meshfree particle method with the implementation of a temperature-dependent homogenization technique was also developed in this thesis. The intrinsic properties of the material associated with each particle could be sought from the atomic level via the TCB rule. Therefore, numerical simulations in nanotechnology can be beneficial from the advantages of the meshfree particle methods. This progress makes it possible to treat extremely large deformation problems and the problems involving discontinuities, such as fractures, at nanoscale. In addition, we developed a thermo-mechanical coupling model through implementing the thermal diffusion equation into nanoscale continuum approximation. Crack propagation at a nanoplate was studied as an example. Since the nanoscale phenomenon of bond breaking is involved when crack propagates, temperature increasing around the crack tip due to the released potential is considered in our thermo-mechanical coupling model.

With the interest to study the electromechanical behavior of nanoscale devices, a design of nanotube-based memory cells is proposed and analyzed via nanoscale meshfree particle method. In this design, the superposed electric field overcomes the interlayer friction in the embedded nanotube-based oscillator so that the steady oscillatory mechanism can be obtained. Under different voltage schemes applied on the attached electrodes, our numerical simulations indicated that the motions of the inner nanotube represent different Boolean logic states.

8.2 Future Work

In the design of the nanotube-based memory cell, the setup scheme indicates that both the inner tube and the outer tube consist of single-walled carbon nanotubes (SWNT). However, during fabrication, carbon nanotubes assemble as either multi-walled nanotubes (MWNTs) or bundles consisting of individual SWNTs that are rather difficult to separate. Given there is no doubt that the proposed memory cell design can be easily extended for practical use, an extended design is assumed, in which an MWNT will be employed as the shell. At the very least, the most outer tube must be capped. The core can consist of either an MWNT or an SWNT bundle. When an open MWNT is used as the core, it is suspected that interlayer slippage may be observed when the core oscillates within the shell. Similar slippage may occur between SWNTs if a SWNT bundle is used as the core. These potential instances of slippage will result in an unstable oscillation mechanism and in turn preclude the use of the proposed NEMS design as a memory cell. The potential for occurrence of the above possible phenomena will be investigated using numerical simulation. In our future research, experiment will also be employed to ascertain and verify slippage phenomena as predicted from numerical methods. If slippage is confirmed, only capped MWNT or the SWNT (capped or open) will be used as the oscillator.

Bounds on the WRITE voltage are critical and must be determined in the practical design. If the applied voltage is too small, an electrostatic force sufficient to overcome the static friction between the inner and outer tubes will not be obtained. In contrast, a WRITE voltage that is too large may cause the inner tube to impact and possibly damage the outer tube due to the large forces and high energy placed on the inner tube. Lee *et al*

claimed that the breakdown voltage of the CNT is round 2.0V/Å [107]. If the electric field is larger than this value, the CNT could start unraveling carbon chains from the exposed edge. A voltage range sufficient to permit a reliable WRITE will be determined.

It has been shown that certain conditions [95] may result in interlayer friction of various values between the outer tube and the inner tube, including: 1) chiralities of the outer tube and the inner tube; 2) topology and vacancy defects in carbon nanotubes; 3) temperature. Some conditions can have a significant effect on interlayer friction and, in turn, influence the predicted interval of the WRITE voltage. Several NEMS designs of various outer tube and inner tube configurations will be investigated in the future. The effects of the temperature in the mechanisms of the proposed memory cell design will also be investigated.

APPENDIX A

MOLECULAR MECHANICS/DYNAMICS

Molecular mechanics/dynamics are one of the standard numerical methods used to study nanoscale systems. Molecular mechanics uses mathematical techniques to yield an equilibrium position of the system. Classical molecular dynamics methods solve Newton's equations of motion numerically for a set of atoms or molecules, which interact via a given potential energy.

A.1 Molecular Dynamics

Molecular dynamics (MD) is a computer simulation technique in which the time evolution of a set of interacting atoms is followed by integrating their equations of motion. We consider a set of atoms labeled by integers $I, I \in [1, n]$ with coordinates $\mathbf{x}_I(t)$. The mass of the nucleus is denoted by m_I. The displacement is defined by

$$\mathbf{u}_I(t) = \mathbf{x}_I(t) - \mathbf{x}_I(0) \tag{A.1}$$

The governing equations are Newton's second law:

$$m_I \ddot{\mathbf{u}}_I = \mathbf{f}_I \tag{A.2}$$

where

$$\mathbf{f}_I = \mathbf{f}_I^{ext} - \mathbf{f}_I^{int} \tag{A.3}$$

where $\mathbf{f}_I$ is the net force acting upon the atom I. $\mathbf{f}_I^{int}$ are forces arising from the same body; $\mathbf{f}_I^{ext}$ are any external forces, such as Van der Waals forces.

The internal forces are obtained from the first derivative of potential energy W with respect to the displacement:

$$\mathbf{f}_I^{int} = \frac{\partial W}{\partial \mathbf{u}_I} = \frac{\partial W}{\partial \mathbf{x}_I} \tag{A.4}$$

The second-order Verlet scheme is used for time integration algorithm (it is identical to the central difference method):

$$\begin{aligned}
\mathbf{u}_I\left(t+\Delta t\right) &= \mathbf{u}_I\left(t\right) + \mathbf{v}_I\left(t\right)\Delta t + \frac{1}{2}\mathbf{a}_I\left(t\right)\Delta t^2 \\
\mathbf{v}_I\left(t+\Delta t/2\right) &= \mathbf{v}_I\left(t\right) + \frac{1}{2}\mathbf{a}_I\left(t\right)\Delta t \\
\mathbf{a}_I\left(t+\Delta t\right) &= \frac{1}{m_I}\mathbf{f}_I\left(t+\Delta t\right) \\
\mathbf{v}_I\left(t+\Delta t\right) &= \mathbf{v}_I\left(t+\Delta t/2\right) + \frac{1}{2}\mathbf{a}_I\left(t+\Delta t\right)\Delta t
\end{aligned} \tag{A.5}$$

A.2 Molecular Mechanics

Molecular mechanics neglects the motion of atoms, so strictly speaking, it only applies to 0K. However, considerable insight to molecular behavior can be gained by molecular mechanics. The governing equations, Eq. (A.2), are then become

$$\mathbf{f}_I = 0 \tag{A.6}$$

where $\mathbf{f}_I$ is the force applied on the atom I.

The nonlinear conjugate gradient method [108] is used with the secant method here to solve these equations. It finds the configuration $\overset{0}{\mathbf{x}}$ that minimizes the total potential energy of the system, which means at this configuration Eq. (A.6) holds.

APPENDIX B

BERENDSEN THERMOSTAT

Temperature is a thermodynamic quantity. For a system containing N particles, the temperature can be related to the average kinetic energy $\langle K \rangle$ of the system through the principle of equipartition of energy, which states that every degree of freedom has an average energy of $\kappa_B T/2$ associated with it [109, 110]. That is

$$\langle K \rangle = \left\langle \sum_i^N \frac{1}{2} m_i v_i^2 \right\rangle = \frac{N_\mathrm{f} \kappa_B T}{2} \tag{B.1}$$

where N_f is the number of degrees of freedom per atom, κ_B is the Boltzmann constant, and T is the thermodynamic temperature.

The Berendsen thermostat [54] can be thought of as a system that is coupled to a thermal bath held at the desired temperature. The coupling is simulated by random "collisions" of system particles with thermal bath particles. After each collision, the velocity of a randomly chosen system particle is modified by a factor λ corresponding to the desired temperature. This λ is given by

$$\lambda = \left[1 + \frac{\Delta t}{\tau_T} \left(\frac{T_0}{T} - 1 \right) \right]^{1/2} \tag{B.2}$$

where Δt is the time step and τ_T is the time constant of the coupling. In this way, the velocities of the particles are adjusted such that the instant temperature T approaches the desired temperature T_0.

APPENDIX C

NONLINEAR CONJUGATE GRADIENT METHOD

The nonlinear conjugate gradient (CG) [108, 111] method finds the stationary point of the system, i.e. the configuration for which the first derivatives of potential function with respect to any coordinate vanish

$$\left.\frac{\partial W(\mathbf{x})}{\partial \mathbf{x}}\right|_{\mathbf{x}}^{0} = 0 \tag{C.1}$$

This configuration $\overset{0}{\mathbf{x}}$ is the solution to $\mathbf{f}_I = 0$ in molecular mechanics.

Given a potential function W, a starting value $\mathbf{x}$, a maximum number of CG iterations $i_{\max}$, a CG error tolerance $\varepsilon < 1$, the minimum point will be found by iteration.

In each iteration, a general line search is used to find the proper α that minimizes $W(\mathbf{x}+\alpha\mathbf{d})$, where $\mathbf{d} = -W'(\mathbf{x})$ is the searching direction, so that

$$\frac{\partial W(\mathbf{x}+\alpha\mathbf{d})}{\partial \alpha} = 0 \tag{C.2}$$

Two iterative methods for this zero-finding are the Newton method and the Secant method. Both methods require that W be twice continuously differentiable. The Newton method also requires that it is possible to calculate the second derivative of $W(\mathbf{x}+\alpha\mathbf{d})$ with respect to α.

The Newton method relies on the Taylor series approximation

$$\frac{\mathrm{d}}{\mathrm{d}\alpha} W(\mathbf{x}+\alpha\mathbf{d}) \approx \left[W'(\mathbf{x})\right]^{\mathrm{T}} \mathbf{d} + \alpha \mathbf{d}^{\mathrm{T}} W''(\mathbf{x}) \mathbf{d} \tag{C.3}$$

The function $W(\mathbf{x}+\alpha\mathbf{d})$ is approximately minimized by setting Eq. (C.3) to zero, giving

$$\alpha = -\frac{W'^{\mathrm{T}}\mathbf{d}}{\mathbf{d}^{\mathrm{T}}W''\mathbf{d}} \tag{C.4}$$

The repeated steps of Eq. (C.4) must be taken until $W'^{\mathrm{T}}\mathbf{d}$ is zero so that the values of $W'^{\mathrm{T}}\mathbf{d}$ and $\mathbf{d}^{\mathrm{T}}W''\mathbf{d}$ must be evaluated at each step. These evaluations may be expensive. Therefore, the Secant method is used here because it avoids calculating the second derivatives of function W. To perform an exact line search without computing W'', the Secant method approximates the second derivatives of $W(\mathbf{x}+\alpha\mathbf{d})$ by evaluating the first derivative at the distinct points $\alpha = 0$ and $\alpha = \sigma$, where σ is an arbitrary small nonzero number:

$$\frac{\mathrm{d}^2}{\mathrm{d}\alpha^2}W(\mathbf{x}+\alpha\mathbf{d}) = \frac{\left[W'(\mathbf{x}+\sigma\mathbf{d})\right]^{\mathrm{T}}\mathbf{d} - \left[W'(\mathbf{x})\right]^{\mathrm{T}}\mathbf{d}}{\sigma} \tag{C.5}$$

The above becomes a better approximation to the second derivative as α and σ approaches zero. Substituting Eq. (C.5) into the Taylor expansion of the first derivative of $W(\mathbf{x}+\alpha\mathbf{d})$, the following equation is given:

$$\frac{\mathrm{d}}{\mathrm{d}\alpha}W(\mathbf{x}+\alpha\mathbf{d}) \approx \left[W'(\mathbf{x})\right]^{\mathrm{T}} + \frac{\alpha}{\sigma}\left\{\left[W'(\mathbf{x}+\sigma\mathbf{d})\right]^{\mathrm{T}}\mathbf{d} - \left[W'(\mathbf{x})\right]^{\mathrm{T}}\mathbf{d}\right\} \tag{C.6}$$

Minimize $W(\mathbf{x}+\alpha\mathbf{d})$ by setting its derivatives to zero:

$$\alpha = -\sigma\frac{\left[W'(\mathbf{x})\right]^{\mathrm{T}}\mathbf{d}}{\left[W'(\mathbf{x}+\sigma\mathbf{d})\right]^{\mathrm{T}}\mathbf{d} - \left[W'(\mathbf{x})\right]^{\mathrm{T}}\mathbf{d}} \tag{C.7}$$

An arbitrary σ is chosen on the first Secant method iteration; on subsequent iterations $\mathbf{x}+\sigma\mathbf{d}$ is chosen to be the value of $\mathbf{x}$ from the previous Secant method iteration and the negative calculated value of α is to be the value of σ for the next interation.

APPENDIX D

ATOMIC LEVEL CAUCHY STRESS

The atomic-level Cauchy stresses [112, 113], $\boldsymbol{\sigma}^A$, of the simulated molecular system with the volume of V_0 can be calculated via

$$\boldsymbol{\sigma}^A = \frac{1}{V_0}\sum_i \left(\frac{1}{2}\sum_{j(\neq i)} \mathbf{r}_{ij} \otimes \mathbf{f}_{ij} \right) \tag{D.1}$$

where $\mathbf{r}_{ij}\left(=\mathbf{r}_j - \mathbf{r}_i\right)$ represents interatomic distance between atoms j and i, and $\otimes$ denotes the tensor product of two vectors. The sign convention adopted here for interatomic forces, $\mathbf{f}_{ij}$, is positive for attraction and negative for repulsion. Accordingly, a positive stress indicates tension and a negative stress indicates compression. The interatomic force from bond-stretching potential is

$$\mathbf{f}_{ij} = \frac{\partial \varphi_s(r_{ij})}{\partial r_{ij}} \frac{\mathbf{r}_{ij}}{r_{ij}} = \varphi_s'(r_{ij}) \frac{\mathbf{r}_{ij}}{r_{ij}} \tag{D.2}$$

For angle-bending potential, the angle θ_{jik} between two vectors $\mathbf{r}_{ij}$ and $\mathbf{r}_{ik}$ can be calculated as

$$\theta_{jik} = \arccos\left(\frac{\mathbf{r}_{ij} \cdot \mathbf{r}_{ik}}{r_{ij} r_{ik}} \right) \tag{D.3}$$

So, the interatomic force from the angle-bending potential [114] is

$$\mathbf{f}_{ij} = -\frac{1}{\sqrt{1-\cos^2\theta_{jik}}} \varphi_a'(\theta_{jik}) \left(\frac{\mathbf{r}_{ik}}{r_{ij} r_{ik}} - \frac{\mathbf{r}_{ij} \cdot \mathbf{r}_{ik}}{r_{ij}^2 r_{ik}} \frac{\mathbf{r}_{ij}}{r_{ij}} \right) \tag{D.4}$$

We should note here that the Monte Carlo method could result in the same state of stresses as molecular dynamic simulations for canonical ensembles.

The continuum-level Cauchy stress, $\boldsymbol{\sigma}^C$, is computed [33] as

$$\boldsymbol{\sigma}^C = J^{-1}\mathbf{F}\cdot\mathbf{P} \tag{D.5}$$

where $\mathbf{P}$ is the nominal stress, $J = \det(\mathbf{F})$ is the determinant of deformation gradient $\mathbf{F}$.

APPENDIX E

MESHFREE METHOD FOR THE DIFFUSION EUQATION

In a two-dimensional problem subject to the Lagrangian description, the thermal diffusion equation is

$$\rho_0 c_v \dot{T} = k\left(\frac{\partial^2 T}{\partial X_1^2} + \frac{\partial^2 T}{\partial X_2^2}\right) \tag{E.1}$$

In order to use the Galerkin's method, we need to develop an appropriate weak form first. Assuming Ω_0 refers to volume of an arbitrary element in the reference configuration, moving all terms in the differential equation to the left-hand side, multiplying by the test function δT and integrating over the volume, the Galerkin weighted residual for the problem is

$$\int_{\Omega_0}\left[\rho_0\dot{T} - \frac{k}{c_v}\left(\frac{\partial^2 T}{\partial X_1^2} + \frac{\partial^2 T}{\partial X_2^2}\right)\right]\delta T d\Omega_0 = 0 \tag{E.2}$$

Using integration by parts,

$$\begin{aligned}
\int_{\Omega_0} -\frac{k}{c_v}\frac{\partial^2 T}{\partial X_1^2}\delta T d\Omega_0 &= -\frac{k}{c_v}\frac{\partial T}{\partial X_1}\delta T\Big|_{\partial\Omega_0} + \frac{k}{c_v}\int_{\Omega_0}\frac{\partial T}{\partial X_1}\frac{\partial(\delta T)}{\partial X_1}d\Omega_0 \\
\int_{\Omega_0} -\frac{k}{c_v}\frac{\partial^2 T}{\partial X_2^2}\delta T d\Omega_0 &= -\frac{k}{c_v}\frac{\partial T}{\partial X_2}\delta T\Big|_{\partial\Omega_0} + \frac{k}{c_v}\int_{\Omega_0}\frac{\partial T}{\partial X_2}\frac{\partial(\delta T)}{\partial X_2}d\Omega_0
\end{aligned} \tag{E.3}$$

where the boundary terms in the right hand sides vanish due to the essential boundary condition requirement. Rearrange all the terms and the weak form is written as

$$\int_{\Omega_0}\delta T\rho_0\dot{T}d\Omega_0 = -\frac{k}{c_v}\int_{\Omega_0}\left(\frac{\partial(\delta T)}{\partial X_1}\frac{\partial T}{\partial X_1} + \frac{\partial(\delta T)}{\partial X_2}\frac{\partial T}{\partial X_2}\right)d\Omega_0 \tag{E.4}$$

In meshfree particle methods [40], the fields of temperature can be approximated as

$$T^h(\mathbf{X},t)=\sum_I \omega_I(\mathbf{X})T_I(t) \tag{E.5}$$

Substituting Eq. (E.5) into weak form Eq. (E.4), the left hand side is

$$\begin{aligned}\rho_0\int_{\Omega_0}\dot{T}\delta T d\Omega_0 &= \rho_0\int_{\Omega_0}\sum_J \omega_J(\mathbf{X})\dot{T}_J\delta T d\Omega_0 \\ &= \rho_0\sum_I\sum_J \omega_J(\mathbf{X}_I)\dot{T}_J\delta T V_I\end{aligned} \tag{E.6}$$

where V_I is the volume of particle I. In order to simplify the equation, we diagonalize the mass matrix and take the advantage of the property of kernel function, $\sum_j \omega_j(\mathbf{X}_I)=1$,

$$\begin{aligned}\rho_0\sum_I\sum_J \omega_J(\mathbf{X}_I)\dot{T}_J\delta T_I V_I &\approx \rho_0\sum_I\sum_J \omega_J(\mathbf{X}_I)\dot{T}_I\delta T_I V_I \\ &= \rho_0\sum_I \dot{T}_I V_I\delta T_I \\ &= \sum_I m_I\dot{T}_I\delta T_I\end{aligned} \tag{E.7}$$

where $m_I=\rho_0 V_I$ is the mass of particle I. The right hand side is

$$\begin{aligned}&-\frac{k}{c_v}\int_{\Omega_0}\left(\frac{\partial(\delta T)}{\partial X_1}\frac{\partial T}{\partial X_1}+\frac{\partial(\delta T)}{\partial X_2}\frac{\partial T}{\partial X_2}\right)d\Omega_0 \\ &=-\frac{k}{c_v}\sum_I\left(\sum_J\frac{\partial\omega_J(\mathbf{X}_I)}{\partial X_1}T_J\sum_K\frac{\partial\omega_K(\mathbf{X}_I)}{\partial X_1}\delta T_K+\sum_J\frac{\partial\omega_J(\mathbf{X}_I)}{\partial X_2}T_J\sum_K\frac{\partial\omega_K(\mathbf{X}_I)}{\partial X_2}\delta T_K\right)V_I \\ &=-\frac{k}{c_v}\sum_K\sum_J\left(\sum_I\left[\frac{\partial\omega_J(\mathbf{X}_I)}{\partial X_1}\frac{\partial\omega_K(\mathbf{X}_I)}{\partial X_1}+\frac{\partial\omega_J(\mathbf{X}_I)}{\partial X_2}\frac{\partial\omega_K(\mathbf{X}_I)}{\partial X_2}\right]V_I\right)T_J(\delta T_K) \\ &=-\frac{k}{c_v}\sum_I\sum_J\left(\int_{\Omega_0}\left[\frac{\partial\omega_I(\mathbf{X})}{\partial X_1}\frac{\partial\omega_J(\mathbf{X})}{\partial X_1}+\frac{\partial\omega_I(\mathbf{X})}{\partial X_2}\frac{\partial\omega_J(\mathbf{X})}{\partial X_2}\right]d\Omega_0\right)T_J(\delta T_I)\end{aligned} \tag{E.8}$$

Since the integral domain is arbitrary, finally we got

$$m_I\dot{T}_I=K_{IJ}T_J \tag{E.9}$$

where

$$K_{IJ}=-\frac{k}{c_v}\int_{\Omega_0}\left[\frac{\partial\omega_I(\mathbf{X})}{\partial X_1}\frac{\partial\omega_J(\mathbf{X})}{\partial X_1}+\frac{\partial\omega_I(\mathbf{X})}{\partial X_2}\frac{\partial\omega_J(\mathbf{X})}{\partial X_2}\right]d\Omega_0 \tag{E.10}$$

APPENDIX F

CALCULATION OF THE THERMAL PARAMETERS

F.1 Thermal Conductivity

Thermal conductivity k is the intensive property of a material that indicates its ability to conduct heat. It is defined as the quantity of heat, Q, transmitted in time t through a thickness L, in a direction normal to a surface of area A, due to a temperature difference ΔT, under steady state conditions and when the heat transfer is dependent only on the temperature gradient.

For the hexagonal-triangular lattice in which the bond length is 1.0nm and the atom mass is $1.0\times10^{-22}\,\mathrm{kg}$, the thermal conductivity is calculated when the atomic interaction is described by the harmonic potential $k = 594\,\mathrm{N/m}$.

Fig. F.1 shows the specimen we used in this numerical experiment. The nanoplate with the hexagonal-triangular lattice has the dimension as $80\mathrm{nm}\times26\mathrm{nm}$. At the initial state, the left boundary and right boundary have the temperature of 100K and 1000K respectively and remain those numbers in the whole process. The heat will transfer from left to right due to the given temperature gradient. The total energy in the center part of the plate is measured as a function of time, so that we can calculate the thermal conductivity using below formula

$$\begin{aligned} k &= \frac{Q}{t}\times\frac{L}{A\times\Delta T} \\ &= \frac{(8.22-5.48)\times10^{-18}\,\mathrm{J}}{10\times10^{-12}\,\mathrm{s}}\times\frac{65\times10^{-9}\,\mathrm{m}}{(26\times10^{-9}\,\mathrm{m}\times10^{-9}\,\mathrm{m})\times900\mathrm{K}} \\ &= 0.76\,\mathrm{w/m\cdot K} \end{aligned} \tag{F.1}$$

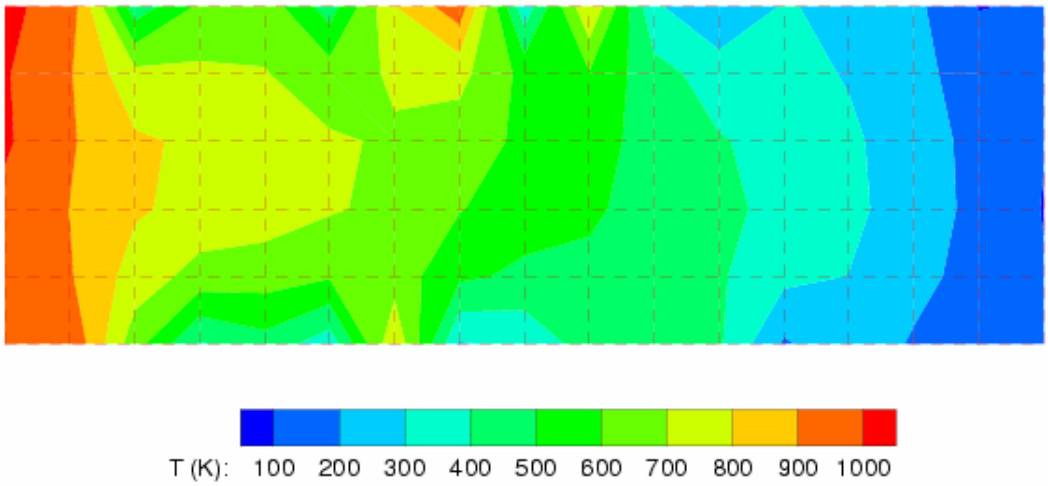

Figure F.1: Temperature profile of the hexagonal-triangular lattice

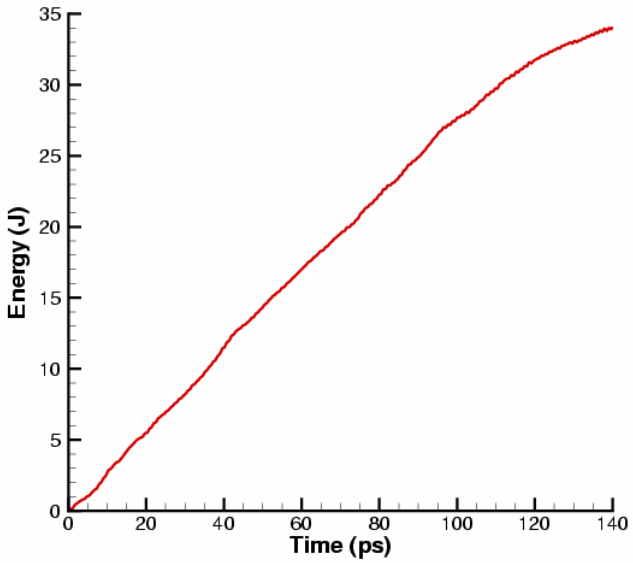

Figure F.2: Total energy evolution of the hexagonal-triangular lattice

F.2 Specific Heat Capacity

Specific heat capacity c is the measure of the heat energy required to raise the temperature of a specific quantity of a substance by certain amount. There are two distinctly different experimental conditions under which specific heat capacity is measured and these are denoted with a subscripted suffix modifying the symbols c. The specific heat of substances could be measured under constant pressure (Symbols: c_p) or constant volume (Symbols: c_v). Here we conduct the numerical experiment to calculate c_v.

The same nanoplate as last experiment is used here. Fig. F.3 and Fig. F.4 gave the temperature and total energy of two different thermal state with the temperature $T = 300.0\text{K}$ and $T = 500.0\text{K}$ respectively. In this case we maintain the volume of the material and the specific heat capacity is calculated as

$$\begin{aligned} c_v &= \frac{1}{m}\left(\frac{\delta Q}{dT}\right)_v \\ &= \frac{1}{1116\times 1.0\times 10^{-22}\,\text{kg}}\left(\frac{(12.75-9.61)\times 10^{-18}\,\text{J}}{200\text{K}}\right) \\ &= 0.141\,\text{J/kg}\cdot\text{K} \end{aligned} \tag{F.2}$$

Combine those parameters above,

$$\Rightarrow \frac{k}{c_v} = \frac{0.76}{0.141} = 5.40\,\text{kg/m}\cdot\text{s} \tag{F.3}$$

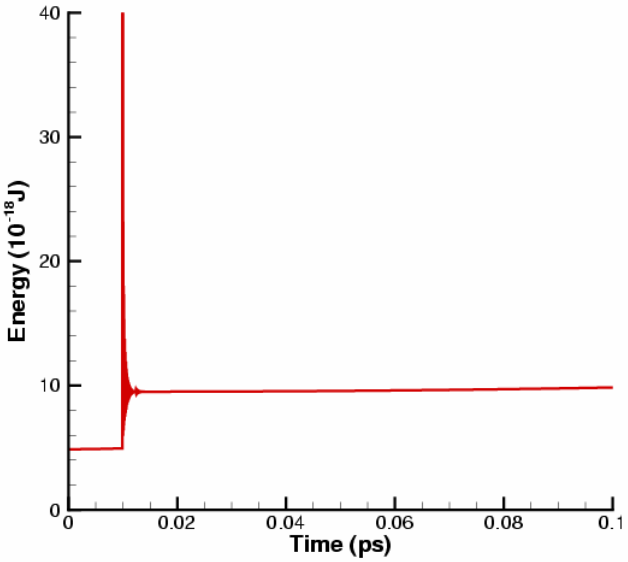

Figure F.3: Total energy of the hexagonal-triangular lattice at T = 300K

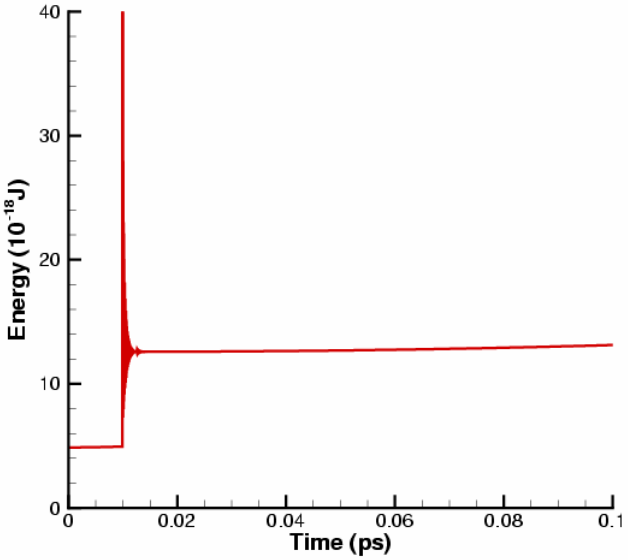

Figure F.4: Total energy of the hexagonal-triangular lattice at T = 500K

REFFERENCES

[1] Luis M. Liz-Marzan and Prashant V. Kamat, *Nanoscale Materials*, Kluwer Academic Publishers, 2003

[2] Carl C. Koch, *Nanostructured Materials*, Noyes Publications, 2002

[3] William A. Goddard, III, Donald W. Brenner, Sergey Edward Lyshevski and Gerald J. Iafrate, *Handbook of Nanoscience, Enginering, and Technology*, CRC Press, 2003

[4] Rountree C. L., Kalia R. K., Lidorikis E., Nakano A., Van B. L. and Vashishta P., Atomistic aspects of crack propagation in brittle materials: Multimillion atom molecular dynamics simulation, *Annual Review of Material Research*, **32**: 377-400, 2002

[5] Abraham F. F., Walkup R., Gao H., Duchaineau M., Rubia T. D. and Seager M., Simulating materials failure by using up to one billion atoms and the world's fastest computer: Brittle fracture, *Proceedings of the National Academy of Sciences, USA*, **99**: 5777-5782, 2002

[6] Tadmor E. B., Ortiz M. and Phillips R., Quasicontinuum analysis of defects in solids. *Philosophical Magazine A,* **73**: 1529-1563, 1996

[7] Tadmor E. B., Phillips R. and Ortiz M., Hierarchical modeling in the mechanics of materials. *International Journal of Solids and Strutures*, **37**: 379-389, 2000

[8] Xiao S. P., Andersen D. R., Han R. and Hou W. Y., Studies of carbon nanotube-based oscillators using molecular dynamics, *Journal of Computational and Theoretical Nanoscience*, **3**: 142-147, 2006

[9] Belytschko T., Krysl P. and Krongauz Y., A three-dimensional explicit element-free Galerkin method. *International Journal for Numerical Methods in Fluids*, **24**(12): 1253-1270, 1997

[10] Chen J. S., Roque C. and Pan C.H., Analysis of metal forming process based on meshless method. *Journal of Materials Processing Technology*, **80**(1): 642-646, 1998

[11] Krysl P and Belytschko T. The Element Free Galerkin method for dynamic propagation of arbitrary 3-D cracks. *International Journal for Numerical Methods in Engineering*, **44**(6): 767-800, 1999

[12] Liu W. K., Hao S, Belytschko T., Li S. F. and Chang C. T., Multiple scale meshfree methods for damage fracture and localization. *Computational Materials Science*, **16**(1-4): 197-205, 1999

[13] Abraham F., Broughton J., Bernstein N. and Kaxiras E., Spanning the continuum to quantum length scales in a dynamic simulation of brittle fracture. *Europhysics Letters*, **44**: 783-787, 1998

[14] Broughton J., Abraham F., Bernstein N. and Kaxiras E., Concurrent coupling of length scales: Methodology and application. *Physical Review B*, **60**: 2391-2403, 1999

[15] Rudd R. E. and Broughton J., Coarse-grained molecular dynamics and the atomic limit of finite elements. *Physical Review B,* **58**: R5893-R5896, 1998

[16] Rudd R. E., Concurrent multiscale simulation and coarse-grained molecular dynamics. *Abstracts of Papers of the American Chemical Society,* **221:** 208, 2001

[17] Wagner G. J. and Liu W. K., Coupling of atomic and continuum simulations using a bridging scale decomposition, *Journal of Computational Physics,* **190**: 249-274, 2003

[18] Park H. S., Karpov E. G., Liu W. K. and Klein P. A., The bridging scale for two-dimensional atomistic/continuum coupling, *Philosophical Magazine*, **85**(1): 79-113, 2005

[19] Belytschko T. and Xiao S. P., Coupling methods for continuum model with molecular model, *International Journal for Multiscale Computational Engineering,* **1**: 115-126, 2003

[20] Xiao S. P. and Belytschko T, A bridging domain method for coupling continua with molecular dynamics. *Computational Method in Applied Mechanics and Engineering,* **193**: 1645-1669, 2004

[21] Smith G. S., Tadmor E. B., Bernstein N. and Kaxiras E., Multiscale simulations of silicon nanoindentation. *ACTA Mater.,* **49**: 4089-4101, 2001

[22] Diestler D. J., Coarse-grained descriptions of multiple scale processes in solid systems. *Physical Review B,* **66**: 184104, 2002

[23] Wu Z. B., Diestler D. J., Feng R. and Zeng X. C, Coarse-graining description of solid systems at nonzero temperature. *Journal of Chemical Physics,* **119**: 8013-8023, 2003

[24] Rodney D. and Phillips R., Structure and strength of dislocation junctions: an atomic level analysis. *Physical Review Letters*, **82**: 1704-1707, 1999

[25] Mortensen J. J., Schiøtz J. and Jacobsen K.W, The quasicontinuum method revisited. *Challenges in Molecular Simulations,* ed. D. Mac Kernan, SIMU Newsletter **4**: 119, 2002

[26] Arroyo M. and Belytschko T, An atomistic-based finite deformation membrane for single layer crystalline films. *Journal of the Mechanics and Physics of Solids,* **50**: 1941-1977, 2002

[27] Arroyo M. and Belytschko T, A finite deformation membrane based on inter-atomic potentials for the transverse mechanics of nanotubes. *Mechanics of Materials*, **35**:193-215, 2003

[28] Shenoy V., Shenoy V. and Phillips R., Finite temperature quasicontinuum methods, *Materials Research Society Symposium Proceeding*, **538**: 465-471, 1999

[29] Chen S. Q., E W. N. and Shu C. W., The heterogeneous multiscale method based on the discontinuous Galerkin method for hyperbolic and parabolic problems, *Multiscale modeling and simulation*, **3**(4): 871-894, 2005

[30] Belytschko T., Lu Y.Y. and Gu L., Element-free Galerkin methods, *International Journal for Numerical Methods in Engineering*, **37**: 229-256, 1994

[31] Liu W. K., Chen Y., Jun S., Chen J. S., Belytschko T., Pan C., Uras R. A. and Chang C. T., Overview and applications of the reproducing kernel particle methods, *Archives of Computational Methods in Engineering: State of the art reviews*, **3**: 3-80, 1996

[32] Randles P. and Libersky L., Smoothed particle hydrodynamics: Some recent improvements and applications, *Computer Methods in Applied Mechanics and Engineering*, **139**: 375-408, 1996

[33] Belytschko T., Liu W. K. and Moran B., *Nonlinear Finite Elements for Continua and Structures*, Wiley, New York, 2000

[34] Marsden J. E. and Hughes T. J. R., *Mathematical Foundations of Elasticity*, Prentice-Hall, 1983

[35] Belytschko T. and Xiao S. P., Stability analysis of particle methods with corrected derivatives, *Computers and Mathematics with Applications*, **43**: 329-350, 2002

[36] Belytschko T., Krongauz Y., Dolbow J. and Gerlach C., On the completeness of meshfree particle methods, *International Journal for Numerical Methods in Engineering ,* **43**: 785-819, 1998

[37] Beissel S. and Belytschko T., Nodal integration of the element-free Galerkin method, *Computer Methods in Applied Mechanics and Engineering*, **139**: 49-74, 1996

[38] Dyka C. T., Randles P. W. and Ingel R. P., Stress points for tension instability in SPH, *International Journal for Numerical Methods in Engineering*, **40**: 2325-2341, 1997

[39] Xiao S. P. and Belytschko T., Material stability analysis of particle methods. *Advances in Computational Mathematics*, **23**: 171-190, 2005

[40] Rabczuk T., Belytschko T. and Xiao S. P., Stable particle methods based on Lagrangian kernels. *Computer Methods in Applied Mechanics and Engineering*, **193**: 1035-1063, 2004

[41] Milstein F., *Mechanics of Solids*, Edited by Hopkins HG and Sewell MJ, Pergamon, Oxford, 1982

[42] Ericksen J., The Cauchy and Born hypotheses for crystals, In *Phase transformations and material instabilities in solids*, Edited by Gurtin ME, Academic Press, 61-77, 1984

[43] Najafabadi R. and Srolovitz D. J., Order-disorder transitions at and segregation to (001) NI-PT surfaces, *Surface Science*, **286**: 104-115, 1993

[44] Garbulsky G. D. and Ceder G., Effect of lattice vibrations on the ordering tendencies in substitutional binary alloys, *Physical Review B*, **49**: 6327-6330, 1994

[45] Diestler D. J., Wu Z. B. and Zeng X. C., An extension of the quasicontinuum treatment of multiscale solid systems to nonzero temperature. *Journal of Chemical Physics,* **121**(19): 9279-9282, 2004

[46] Dupuy L. M., Tadmor E. B., Miller E. M. and Phillips R., Finite-temperature quasicontinuum: Molecular dynamics without all the atoms. *Physical Review Letters*, **95**: 060202, 2005

[47] Atkins P. and Paula J., *Physical Chemistry*, 7th edition, Oxford University Press, 2001

[48] Chandler D., *Introduction to Modern Statistical Mechanics*, Oxford, 1987

[49] Foiles, S. M., Evaluation of harmonic methods for calculating the free energy of defects in solids, *Physical Review B*, **49:** 14930-14938, 1994

[50] LeSar R., Najafabadi R. and Srolovitz D. J., Finite-temperature defect properties from free-energy minimization, *Physical Review Letters*, **63**: 624-627, 1989

[51] Najafabadi R., and Srolovitz D. J., Evaluation of the accuracy of the free-energy-minimization method, *Physical Review B*, **52**: 9229-9241, 1995

[52] Rickman J. M. and LeSar R., Free-Energy calculation in material research, *Annual Review of Material Research*, **32**: 195-217, 2002

[53] Jiang H., Huang Y. and Hwang K. C., A finite-temperature continuum theory based on interatomic potentials, *Journal of Engineering Materials and Technology*, **127**(4): 408-416, 2005

[54] Berendsen H. J. C., Postma J. P. M., Gunsteren W. F. van, DiNola A. and Haak J. R., Molecular dynamics with coupling to an external bath, *Journal of Chemical Physics*, **81**(8): 3684-3690, 1984

[55] Tadmor E.B., Smith G., Bernstein N. and Kaxiras E., Mixed finite element and atomistic formulation for complex crystals, *Physical Review B*: **59**(1): 235-245, 1999

[56] Belytschko T., Xiao S. P., Schatz G. C. and Ruoff R., Atomistic simulations for nanotube fracture, *Physics Review B*, **65**: 235430, 2002

[57] Organ D. J., Fleming M. and Belytschko T., Continuous meshless approximations for nonconvex bodies by diffraction and transparency, *Computational Mechanics,* **18**: 225-235, 1996

[58] Klein P. A., Foulk J. W., Chen E. P., Wimmer S. A. and Gao H. J., Physics-based modeling of brittle fracture: cohesive formulations and the application of meshfree methods, *Theoretical and Applied Fracture Mechanics*, **37**: 99-166, 2001

[59] Gao H., A theory of local limiting speed in dynamic fracture. *Journal of the Mechanics and Physics of Solids,* **44**: 1453-1474, 1996

[60] Hadamard J., *Lecons sur la Propagation des Ondes et les Equations de l'Hydrodynamique*, Hermann, Paris, chapter 6, 1903

[61] Hill R., Acceleration waves in solids, *Journal of the Mechanics and Physics of Solids*, **10**: 1-16, 1962

[62] Ogden R. W., *Nonlinear Elastic Deformations*, Ellis Horwood, Chichester, 1997

[63] Sands D. E., *Introduction to Crystallography*, Dover, New York, 1993

[64] Nye J. F., *Physical Properties of Crystals*, Oxford University Press, Oxford, 1985

[65] Miller Jr. W., *Symmetry Groups and Their Applications*, first edition, Pure and Applied Mathematics, Academic Press, New York, vol. 50, 1972

[66] Elliott R. S., Shaw J. A. and Triantafyllidis N., Stability of crystalline solids - I: Continuum and atomic lattice considerations, *Journal of the Mechanics and Physics of Solids*, **54**(1): 161-192, 2006

[67] Elliott R. S., Shaw J. A. and Triantafyllidis, N., Stability of crystalline solids - II: Application to temperature-induced martensitic phase transformations in a bi-atomic crystal , *Journal of the Mechanics and Physics of Solids*, **54**(1): 193-232, 2006

[68] Rice J. R., In *Theoretical and Applied Mechanics*, Koher WT, North-Holland: Amsterdam, **207**, 1977

[69] Rudnicki J. W. and Rice J. R., Conditions for the localization of deformation in pressure-sensitive dilatant materials, *Journal of the Mechanics and Physics of Solids*, **23**: 371, 1975

[70] Xiao S. P. and Hou W. Y., Studies of size effects on carbon nanotubes' mechanical properties by using different potential functions, *Fullerenes, Nanotubes and Carbon Nanostructures*, **14**: 9-16, 2006

[71] Xiao S. P. and Hou W. Y., Fracture of vacancy-defected carbon nanotubes and their embedded composites, *Physical Review B*, **73**: 115406, 2006

[72] Xiao S. P. and Yang W. X., A temperature-related homogenization technique and its implementation in the meshfree particle method for nanoscale simulations, *International Journal for Numerical Methods in Engineering*, **69**: 2099-2125, 2007

[73] Xiao S. P. and Yang W. X., A nanoscale meshfree particle method with the implementation of quasicontinuum method, *International Journal of Computational Methods*, **2**: 293-313, 2005

[74] Kreith F. and Bohn M. S., *Principles of Heat Transfer*, sixth edition, Brooks/Cole, 2001

[75] Hoover W. G., Canonical dynamics - Equilibrium phase-space distributions, *Physical Review A*, **31**: 1695-1697, 1985

[76] Iijima S., Helical microtubules of graphitic carbon, *Nature*, **354**(6348): 56-58, 1991

[77] Popov V. N., Carbon nanotubes: properties and application, *Materials Science & Engineering R-reports*, **43**(3): 61-102, 2004

[78] Bernholc J., Brenner D., Nardelli M. B., *et al*., Mechanical and electrical properties of nanotubes, *Annual Review of Materials Research*, **32**: 347-375, 2002

[79] Dalton A. B., Collins S., *et al*., Continuous carbon nanotube composite fibers: properties, potential applications, and problems, *Journal of Materials Chemistry*, **14:** 1, 2004

[80] Bachtold A., Hadley P., Nakanishi T., and Dekker C., Logic circuits with carbon nanotube transistors, *Science*, **294**: 1317-1320, 2001

[81] Kinaret J. M., Nord T., and Viefers S., A carbon-nanotube-based nanorelay, *Applied Physics Letters*, **82**(8): 1287-1289, 2003

[82] Kim, P. and Lieber C. M., Nanotube nanotweezers, *Science*, **286**(5447): 2148-2150, 1999

[83] Srivastava D., A phenomenological model of the rotation dynamics of carbon nanotube gears with laser electric fields, *Nanotechnology*, **8**: 186-192, 1997

[84] Ke C. and Espinosa H. D., Feedback controlled nanocantilever device, *Applied Physics Letters*, **85**: 681, 2004

[85] Kang J. W. and Hwang H. J., Nanoscale carbon nanotube motor schematics and simulations for micro-electro-mechanical machines, *Nanotechnology*, **15**:1633-1638, 2004

[86] Cumings J. and Zettl A, Low-friction nanoscale linear bearing realized from multiwall carbon nanotubes, *Science*, 289(5479): 602-604, 2000

[87] Lozovik Y. E., Minogin A. V. and Popov A. M., Nanomachines based on carbon nanotubes, *Physics Letters A*, **313**(1-2): 112-121, 2003

[88] Forro L., Nanotechnology: beyond Gedanken experiments, *Science*, **289**(5479): 560-561, 2000

[89] Zheng Q. S. and Jiang Q., Multiwalled carbon nanotubes as gigahertz oscillators, *Physical Review Letters*, **88**: 045503, 2002

[90] Zheng Q. S., Liu J. Z. and Jiang Q., Excess van der Waals interaction energy of a multiwalled carbon nanotube with an extruded core and the induced core oscillation, *Physical Review B*, **65**: 245409, 2002

[91] Legoas1 S. B., Coluci1 V. R., *et al*., Molecular-dynamics simulations of carbon nanotubes as gigahertz oscillators, *Physical Review Letters*, **90**: 055504, 2003

[92] Legoas1 S. B., Coluci1 V. R., *et al*., Gigahertz nanomechanical oscillators based on carbon nanotubes, *Nanotechnology*, **15**: S184, 2004

[93] Tangney P., Louie S. G. and Cohen M. L., Dynamic sliding friction between concentric carbon nanotubes, *Physical Review Letters*, **93**: 065503, 2004

[94] Rivera J. L., McCabe C. and Cummings P. T., The oscillatory damped behaviour of incommensurate double-walled carbon nanotubes, *Nanotechnology*, **16**: 186, 2005

[95] Guo W. L., Guo Y. F., Gao H. J., Zheng Q. S. and Zhong W. Y., Energy dissipation in gigahertz oscillators from multiwalled carbon nanotubes, *Physical Review Letters*, **91**: 125501, 2003

[96] Anantram M. P. and Leonard F., Physics of carbon nanotube electronic devices, *Reports on Progress in Physics*, **69**: 507-561, 2006

[97] Krysl P. and Belytschko T., Analysis of thin shells by the element-free Galerkin method, *International Journal of Solids and Structures*, **33**: 3057-3080, 1996

[98] Arroyo M. *Ph.D. thesis*, Northwestern University, 2003

[99] Xiao S. P., Han R. and Hou W. Y., Spin in carbon nanotube-based oscillators, *International Journal of Nanoscience*, **5**(1): 47-55, 2006

[100] Liu W. K., Karpov E. G. and Park H. S, *Nano Mechanics and Materials: Theory, Multiscale Methods and Applications*, John Wiley & Sons, Ltd, 2006

[101] Lyshevski S. E. *Nano- and Micro- Electromechanical Systems: Fundamentals of Nano- and Microengineering*, second edition, CRC Press, 2005

[102] Gluck P., Force on the dielectric in a parallel plate capacitor, *The Physics Teacher*, 41: 521-523, 2003

[103] Dietz E. R., Force on a dielectric slab: Fringing field approach, *American Journal of Physics*, 72(12): 1499-1500, 2004

[104] Hayt, W. H. Jr. and Buck J. A., *Engineering Electromagnetics*, sixth edition, McGraw-Hill, 2001

[105] Ramo S., Whinnery J. R. and Duzer T. V., *Fields and Waves in Communication Electronics*, third edition, John Wiley & Sons, Inc, 1994

[106] Grujicic M., Cao G. and Roy W. N., A computational analysis of the carbon-nanotube-based resonant-circuit sensors, *Applied Surface Science*, **229**: 316-323, 2004

[107] Lee Y. H., Kim S. G. and Tomanek D., Field-induced unraveling of carbon nanotubes, *Chemical Physics Letters*, **265**: 667-672, 1997

[108] Gilbert J. C. and Nocedal J., Global convergence properties of conjugate gradient methods, *SIAM Journal on Optimization*, **2**, 1992

[109] Dehoff R. T., *Thermodynamics in Materials Science*, McGraw-Hill, New York, 1993

[110] Hu Y. and Sinnott S. B., Constant temperature molecular dynamics simulations of energetic particle–solid collisions: comparison of temperature control methods, *Journal of Computational Physics*, **200**: 251-266, 2004

[111] Shewchuk J., An introduction to the conjugate gradient method without the agonizing pain, *Technical report, School of Computer Science, Carnegie Mellon University,* CMU-CS-94-125, 1994

[112] Zhang S., H. Johnson T., Wagner G. J., Liu W. K. and Hsia K. J., Stress generation mechanisms in carbon thin films grown by ion-beam deposition, *Acta Materialia*, **51**: 5211-5222, 2003

[113] Zhou M., A new look at the atomic level virial stress: on continuum-molecular system equivalence, *Royal Society of London Proceedings Series A*, **459**(2037): 2347-2392, 2003

[114] Gao J. and Weiner J. H., Intrinsic atomic-level stresses in polymer melts and networks, *Journal of Chemical Physics*, **90**(11): 6749-6760, 1989